NOAA OAR Special Report

PMEL Tsunami Forecast Series: Vol. 8
A Tsunami Forecast Model for Nantucket, Massachusetts

Michael C. Spillane

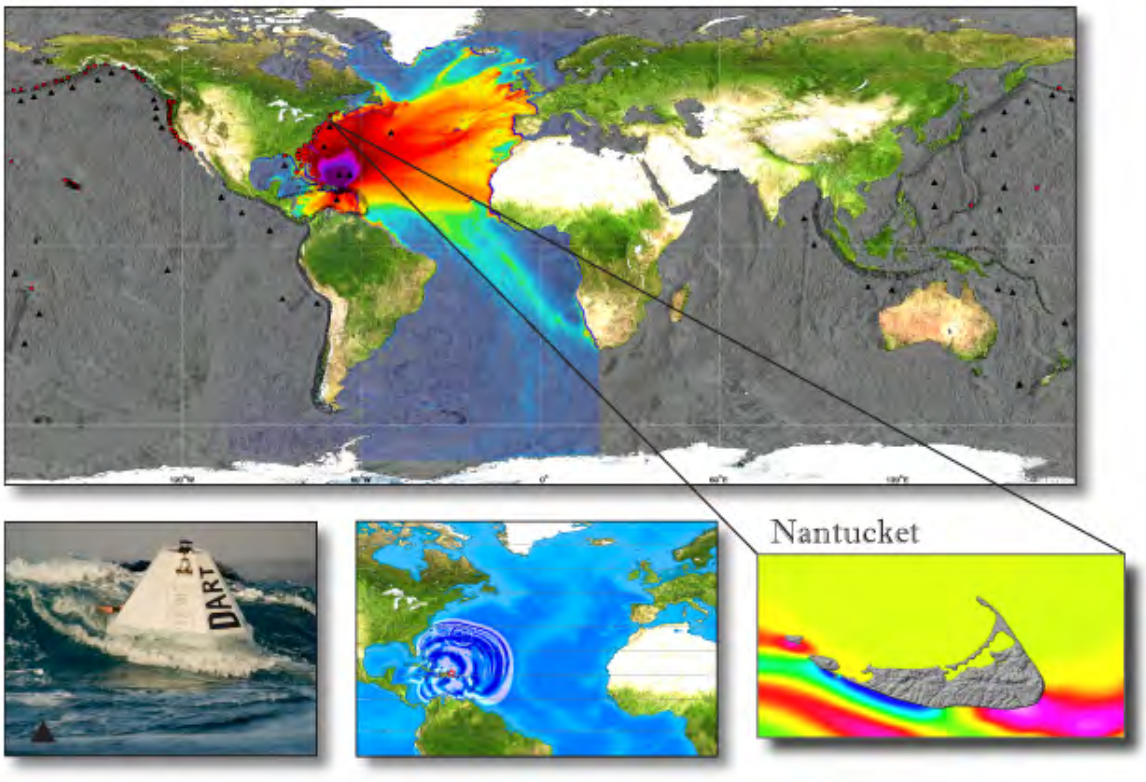

NOAA Center for Tsunami Research (NCTR)
Pacific Marine Environmental Laboratory

Front cover image: Overview of NOAA tsunami forecast system. Top frame illustrates components of the tsunami forecast using the August 1946 Dominican Republic event as an example: DART systems (black triangles), precomputed tsunami source function database (unfilled black rectangles) and high-resolution forecast models in the Pacific, Atlantic, and Indian oceans (red squares). Colors show computed maximum tsunami amplitudes of the offshore forecast. Black contour lines indicate tsunami travel times in hours. Lower panels show the forecast process sequence left to right: tsunami detection with the DART system (third generation DART ETD is shown); model propagation forecast based on DART observations; coastal forecast with high-resolution tsunami inundation model.

PDF versions of the PMEL Tsunami Forecast Series reports are available at
http://nctr.pmel.noaa.gov/forecast_reports

NOAA OAR Special Report

PMEL Tsunami Forecast Series: Vol. 8
A Tsunami Forecast Model for Nantucket, Massachusetts

M.C. Spillane[1,2]

1 Joint Institute for the Study of the Atmosphere and Ocean (JISAO), University of Washington, Seattle, WA
2 NOAA/Pacific Marine Environmental Laboratory (PMEL), Seattle, WA

January 2015

UNITED STATES DEPARTMENT OF COMMERCE

Penny Pritzker
Secretary

NATIONAL OCEANIC AND ATMOSPHERIC ADMINISTRATION

Kathy Sullivan
Under Secretary for Oceans and Atmosphere/Administrator

Office of Oceanic and Atmospheric Research

Craig McLean
Assistant Administrator

NOTICE from NOAA

Mention of a commercial company or product does not constitute an endorsement by NOAA/ OAR. Use of information from this publication concerning proprietary products or the tests of such products for publicity or advertising purposes is not authorized. Any opinions, findings, and conclusions or recommendations expressed in this material are those of the authors and do not necessarily reflect the views of the National Oceanic and Atmospheric Administration.

Contribution No. 3400 from NOAA/Pacific Marine Environmental Laboratory

Contribution No. 2108 from Joint Institute for the Study of the Atmosphere and Ocean (JISAO)

Also available from the National Technical Information Service (NTIS)

(http://www.ntis.gov)

Contents

List of Figures

List of Tables

Foreword

Tsunamis have been recognized as a potential hazard to United States coastal communities since the mid-twentieth century, when multiple destructive tsunamis caused damage to the states of Hawaii, Alaska, California, Oregon, and Washington. In response to these events, the United States, under the auspices of the National Oceanic and Atmospheric Administration (NOAA), established the Pacific and Alaska Tsunami Warning Centers, dedicated to protecting United States interests from the threat posed by tsunamis. NOAA also created a tsunami research program at the Pacific Marine Environmental Laboratory (PMEL) to develop improved warning products.

The scale of destruction and unprecedented loss of life following the December 2004 Sumatra tsunami served as the catalyst to refocus efforts in the United States on reducing tsunami vulnerability of coastal communities, and on 20 December 2006, the United States Congress passed the "Tsunami Warning and Education Act" under which education and warning activities were thereafter specified and mandated. A "tsunami forecasting capability based on models and measurements, including tsunami inundation models and maps" is a central component for the protection of United States coastlines from the threat posed by tsunamis. The forecasting capability for each community described in the PMEL Tsunami Forecast Series is the result of collaboration between the National Oceanic and Atmospheric Administration office of Oceanic and Atmospheric Research, National Weather Service, National Ocean Service, National Environmental Satellite, Data, and Information Service, the University of Washington's Joint Institute for the Study of the Atmosphere and Ocean, National Science Foundation, and United States Geological Survey.

NOAA Center for Tsunami Research

PMEL Tsunami Forecast Series: Vol. 8
A Tsunami Forecast Model for Nantucket, Massachusetts

M.C. Spillane[1,2]

Abstract. Operational tsunami forecasting by NOAA's Tsunami Warning Centers relies on the detection of tsunami wave trains in the open ocean, inversion of these data (telemetered via satellite) to quantify their source characteristics, and real-time modeling of the impact on threatened coastal communities. For each such community, the latter phase of the process involves a pre-tested forecast model capable of predicting the impact, in terms of inundation and dangerous inshore currents, with sufficient resolution and within the time constraints appropriate to an emergency response. To achieve this goal, considerable advance effort is required to tune each forecast model to the specific bathymetry and topography, both natural and manmade, of the impact area, and to validate the model's performance with a broad set of tsunami sources. Where possible, the validation runs should replicate observed responses to historical events, but the sparse instrumental record of these rare but occasionally devastating occurrences dictates that comprehensive testing also include a suite of scenarios that represent potential future events.

During the forecast model design phase, and in research mode outside the pressures of an emergency situation, more detailed and slower-running models can be investigated. Such a model, referred to as a reference model, represents the most credible numerical representation of tsunami response for a study region, using the most detailed bathymetry available and without the run-time constraint of operational use. Once a reference model has been developed, the process of forecast model design is to determine where efficiencies can be gained by reducing the grid resolution and increasing the model time step, while still adequately representing the salient features of the full solution.

This report documents the reference and forecast model development for Nantucket, Massachusetts. South of Cape Cod and east of Martha's Vineyard, the name Nantucket applies to the county, the island, and the community upon it. The harbor opens to the north and the shallow Nantucket Sound; the east and south coasts are exposed to the North Atlantic and can be impacted by the passage of hurricanes and tropical storms. A similar pattern of exposure applies to tsunamis and, although there are no reports of tsunami impact to date, this report will document that the island is not immune should a significant earthquake occur, in particular one centered north of Puerto Rico. The population of Nantucket expands greatly with vacationers in the summer months. While the hazard associated with tsunamis is of low probability, the drastic impact of such events demonstrated around the globe in recent years has illustrated the need for emergency preparedness. This report addresses the tsunami aspects of the natural hazard spectrum.

1 Joint Institute for the Study of the Atmosphere and Ocean (JISAO), University of Washington, Seattle, WA
2 NOAA/Pacific Marine Environmental Laboratory (PMEL), Seattle, WA

1. Background and Objectives

1.1 The setting

Nantucket is a county of the state of Massachusetts. The crescent-shaped island (**Figure 1**) has a long history of occupation dating back to its original inhabitants, the Native American Wampanoag people, and into colonial times. Its current year-round population is 10,172 (Census Bureau, 2010). This swells to 50,000 or more during the summer months when Nantucket is a popular vacation destination with air links to several points in the northeast U.S. and ferry service to the mainland and to Martha's Vineyard. The island was a center of marine chandlery and whaling activities, supporting a large population, until a mid-1800s decline. This resulted from lack of rail transport available to mainland ports, silting of the harbor, and an 1846 fire (`www.nha.org/history/faq/index.html`). Later, an industry-wide decline ensued as mineral oil replaced whale oil. After reaching a low of 2797 in 1920, the population began a rebound, particularly after 1950, associated with recreational activities.

NOAA Chart 13241, reproduced in **Figure 2**, shows the main island, which together with two smaller islands to the west, Tuckernuck and Muskeget, compose Nantucket County. At the northeast corner of Nantucket Island is a long spit leading to Great Point, which is the site of Great Point Lighthouse. This spit is occasionally breached during the passage of hurricanes or tropical storms and, as seen in this report, could be severely impacted in the event of a tsunami. Together with Monomoy Island, extending south from the Massachusetts mainland near Chatham, and Martha's Vineyard to the west, the shallow Nantucket Sound is largely enclosed, as seen in NOAA Chart 13237 reproduced in **Figure 3**. Extensive shoaling is present to the south and east of Nantucket, the entire region being the remnants of what was once a terminal moraine during the last period of glaciation.

South of Nantucket, the continental shelf is wide and extends eastward into Georges Bank. Nantucket Sound has been treacherous to shipping over the years. Some dramatic incidents in the last century include the SS *Andrea Dorea* collision in 1956 and the 1976 grounding of the tanker *Argo Merchant*, which led to a massive oil spill. The entrance to Nantucket Harbor, the terminus of year-round ferry service on the island's north side, receives some protection by the shallow sound and submerged jetties. Simulated tsunamis investigated during model development have far greater impact on community and vacation developments along the south and east coasts, such as Madaket, Miacomet, and Siasconset. Adjacent to the south coast is Nantucket Memorial Airport; the south end of its main runway is about 330 m from the shoreline at an elevation of only 8.5 m above mean high water (MHW) level. These areas, whose locations are indentified in **Figure 2**, were evaluated during model development and are discussed below. The primary focus of the model is, however, the Nantucket Harbor area where population and infrastructure are concentrated. The harbor area is shown in **Figure 4**; the location of the tide gauge is marked. Although at the time of writing no tsunamis have

been recorded on Nantucket, the tide gauge is the warning point for the Nantucket model. The harbor has only a narrow entrance with a dredged channel flanked by jetties but extends eastward, screened from the sound by Coatue Spit, which links to the previously mentioned Great Point Spit. The broader setting of Nantucket in the northwestern Atlantic is shown in **Figure 5**.

1.2 Tsunami and other coastal hazards

Unlike the forecast model sites of the Pacific basin, those on the eastern seaboard of the U.S. and the Caribbean have a very limited historic record of tsunami inundation. **Figure 5** shows potential sites for seismic generation of tsunamis, and the location of DART (Deep-ocean Assessment and Reporting of Tsunami) tsunameters available for their detection. Siting of the DART array was discussed by Spillane *et al.* (2008). The devastating tsunami that accompanied the 1755 Lisbon earthquake was not reported on the U.S. mainland despite a colonial population engaged in coastal pursuits; Nantucket's first lighthouse at Brant Point, for example, was authorized at a town meeting in 1746. Tsunami waves from Lisbon were felt in the eastern Caribbean and possibly the Maritime Provinces of Canada. The landslide-generated Newfoundland tsunami of 1929 (Fine *et al.*, 2005) produced a runup of 0.68 m at Atlantic City, New Jersey, lesser amounts at Ocean City, Maryland, and Charleston, South Carolina, but only non-quantified reports from Maine, New Hampshire, Massachusetts, and Rhode Island (Lander and Lockridge, 1989). East Coast forecast models, and the current report for Nantucket in particular, suggest the greatest tsunami threat is associated with the trench north of Puerto Rico. An earthquake of moment magnitude (Mw) 7.3 in the Mona Passage in 1918, while causing severe damage and loss of life in Puerto Rico and the Virgin Islands, was only weakly felt on the U.S. mainland (0.06 m in Atlantic City). Two events in August 1946, northeast of the Dominican Republic and of slightly larger magnitude, caused severe local impacts but only nonquantified effects to Atlantic City and Daytona Beach, Florida, were reported. The only explicit mention of Nantucket in the National Geophysical Data Center (NGDC) tsunami hazard database (Dunbar, 2007) is an 1879 account of a sailing party that encountered "a vast, huge wave stretching shore to shore" in the Tuckernuck Channel (Holbrook, 1924). The wave may have resulted from a submarine landslide, and while a boon to fishing, shoals surrounding Nantucket, referred to as "the rips," can cause hazardous wave conditions. In summary, there are no historical events with which to validate tsunami model predictions for Nantucket.

Inundation and coastal erosion of the islands is not, however, an unusual occurrence. Winter storms, or the passage nearby of hurricane and tropical storm tracks, have caused damage in the past. Notable is the New England Hurricane of 1938, also referred to as the "Yankee Clipper" or the "Long Island Express," but earlier regional impacts were felt in 1635, 1815, 1821, 1869, and 1893. **Figure 6** includes a composite of storm tracks from a compilation described by McAdie *et al.* (2009) and available from the National Hurricane Center. Though eclipsed by damage to New Jersey and New York, some streets in Nantucket were inundated and property damage occurred at the west end of the island during the 2012 "Frankenstorm" Hurricane Sandy (Inquirer and Mirror, 2012).

The U.S. Army Corps of Engineers (USACE, 1997) has simulated hurricane impact on the counties of southern Massachusetts. Based on the National Hurricane Center's SLOSH (Sea, Lake, and Overland Surges from Hurricanes) model and categories of hurricane intensity and forward speed, a set of inundation maps are available online. The USACE study reports more than 25% of the summer population of Nantucket as vulnerable to "weak" hurricane surge flooding, and issues such as shelter availability and evacuation times are addressed. The Nantucket chart, reproduced in **Figure 7**, closely resembles the patterns found for the most severe tsunami scenarios investigated in this report: those originating near Puerto Rico. The road network and pattern of habitation on Nantucket clearly reflect the hurricane surge inundation hazard and, given the several hours of tsunami travel time likely, the USACE results are likely quite relevant to a major seismically generated tsunami event. Submarine landslides, triggered by seismic events, can cause significant local tsunami waves: for example, Newfoundland's Burin Peninsula was strongly impacted in 1929, as was the north coast of Biak Island during the 1996 Irian Jaya tsunami. Landslide-generated tsunami waves are not currently included in the forecast methodology, nor are meteorologically generated tsunamis. However, to the extent that the waves they produce are detected by the DART array (see **Figure 5**), some warning of their presence may be available.

1.3 Tsunami warning and risk assessment

The forecast model development described here will permit Nantucket, Massachusetts, to be incorporated into the tsunami forecasting system, SIFT (Short-term Inundation Forecasting for Tsunamis), developed at NCTR (NOAA Center for Tsunami Research) and now in operational use at the U.S. Tsunami Warning Centers (TWCs). The system has had considerable success in accurately forecasting the impact of both moderate and severe Pacific basin tsunami events in recent years and, in the following section, the methodology that permits such forecasts is described. Although the absence of historical records precludes validation of the Nantucket model, the stability it has exhibited during extensive testing suggests it will provide accurate real-time forecasts to inform local emergency response in the future. Additionally, the synthetic scenarios investigated during model development and reported here provide an initial tsunami risk assessment by determining the relative impacts to Nantucket associated with different source regions, as described in Section 4 of this report.

2. Forecast Methodology

2.1 The tsunami model

In operational use, a tsunami forecast model is used to extend a precomputed deep-water solution into the shallows, and onshore as inundation if appropriate. The model consists of a set of three nested grids named A (outermost with coarse resolution), B (intermediate), and C (innermost). The latter provides fine resolution that, in a real-time application of the MOST (Method of Splitting Tsunami; Titov and González, 1997; Titov and Synolakis, 1998) model, permits forecasts at spatial scales (as little as a few tens of meters) relevant to local emergency management. The validity of the MOST model applied in this manner, and the operational effectiveness of the forecast system built around it, has been demonstrated during unplanned tests in the Pacific basin triggered by several mild to moderate tsunami events in the years since the 2004 Indian Ocean disaster (Wei *et al.*, 2008). Successful hindcasting of observed historic events, even mild ones, during forecast model development lends credence to the ability to accurately forecast the impact of future events. Such validation of tsunami modeling procedures is documented in other volumes of this series. Before proceeding to a description of the forecast model development for Nantucket, Massachusetts, it is useful to describe the steps in the overall forecast process.

2.2 NOAA's tsunami forecast system

Operational tsunami forecasts are generated at TWCs, staffed continuously around the clock in Alaska and Hawaii, using the SIFT tool, developed at NCTR. The semi-automated process facilitates the steps by which TWC operators assimilate data from an appropriate subset of DART tsunami sensors, "invert" the data to determine the linear combination of precomputed propagation solutions that best match the observations, then initiate a set of forecast model runs if coastal communities are threatened, or, if warranted, cancel the warning. Steps in the process are as follows:

- When a submarine earthquake occurs, the global network of seismometers registers it. Based on the epicenter, the unit sources in the propagation database (Gica *et al.*, 2008) that are most likely to be involved in the event and the DART array elements (Spillane *et al.*, 2008) best placed to detect the waves' passage are identified. TWC operators can trigger DARTs into rapid sampling mode in the event that this did not occur automatically in response to the seismic signal.
- There is now a delay while the tsunami waves are in transit to the DARTs. At least a quarter of a cycle of the first wave in the train must be sampled before moving to the "inversion" step. In the interim, SIFT allows the operator to request a "seismic solution" based on the location and reported magni-

tude of the earthquake. This solution, however, may only poorly represent the tsunami; magnitude estimates may be substantially revised as more seismic data accumulate. Only when sea level fluctuations are detected can the reality and scale of the waves be determined

- When sufficient data have accumulated at one or more DARTs, the observed time series are compared with the model series from the candidate unit sources. Since the latter are precomputed (using the MOST code), and the dynamics of tsunami waves in deep water are linear, a least squares approach can quickly identify the unit sources (and the appropriate scale factors for each) that best fit the observations. The inversion methodology is described by Percival *et al.* (2011).
- Drawing again on the propagation database, the scale factors are applied to produce a composite basin-wide solution with which to identify the coastal regions most threatened by the radiating waves.
- It is at this point that one or more forecast models are run. The composite propagation solution is employed as the boundary condition to the outermost (A-grid) domain of a nested set of three real-time MOST model grids that telescope with increasingly fine scale to the community of concern. A-grid results provide boundary conditions to the middle B grid, which, in turn, forces the innermost C grid. Nonlinear processes, including inundation, are modeled so that, relying on the validation procedures during model development, credible forecasts of the current event are available.
- Each forecast model provides quantitative and graphic forecast products with which to inform the emergency response or to serve as the basis for canceling or reducing the warnings. Unless the tsunami source is local, the forecast is generally available before the waves arrive. Even when lead time cannot be provided, the several hour duration of a significant event (in which the first wave may not be the most damaging) gives added value to the multi-hour forecasts provided.

Because multiple communities may be at risk, it may be necessary to run, simultaneously or in a prioritized manner, multiple forecast models. Each must be optimized to run efficiently in as little time as possible. The current standard is that an operational forecast model should be capable of simulating 4 hr of real time within about 10 min of CPU time on a fast workstation computer.

3. Model Development

3.1 Digital elevation models

Water depth determines local tsunami wave speed and subaerial topography determines the extent to which tsunami waves inundate the land. Thus, a prerequisite for credible tsunami modeling is the availability of accurate gridded bathymetric and topographic datasets, termed digital elevation models, or DEMs. Given their expertise in this area and the number of coastal communities needing tsunami forecast capability, NCTR relies on the NGDC to provide the DEMs needed. The Nantucket DEM, a composite of multiple data sources merged and converted to a common datum of MHW, was produced and documented by Eakins *et al.* (2009), and is employed in creating the B and C grids of both the reference and forecast models. Salient features of the DEM are provided in **Table 1** and an oblique view from the report is reproduced as **Figure 8**. NCTR maintains an atlas of lower-resolution gridded bathymetries, and other resources—such as the GEBCO (General Bathymetric Chart of the Ocean) digital atlas, published by the British Oceanographic Data Centre—can be used for the A grids, as described later.

The use of MHW as the "zero level" for forecast models is standard. The MOST model does not include tidal fluctuations, and, since a tsunami may arrive at any stage of the tide, it is best to employ a "worst-case" approach by assuming high tide when forecasting inundation. For some forecast models, grounding of vessels and the strong and rapidly varying currents often associated with even mild tsunamis are of concern. Nantucket Harbor, the ferry terminal, and much of the recreational vessel moorings lie on the sheltered northern side of the island. Here, water level excursions are less severe than on the south and east coasts, but the potential risks of low-water impacts will be addressed during the later discussion.

3.2 Tides and sea level variation

The history of tidal observation at Nantucket dates back only to 1963. The tide station NOS 8449130 is located on the west side of Steamboat Wharf, which also houses the ferry terminal (see **Figure 4**). The instrumentation was upgraded in 2008 to include a tsunami-capable gauge sampling at 1-min intervals; data from 1996 to the present, sampled at 6-min intervals, are conveniently available online.[3]

Station characteristics for NOS 8449130 are provided in **Table 2**, based on the wealth of online tidal information available at NOAA's CO-OPS (Center for Operational Oceanographic Products and Services) website, `tidesandcurrents.noaa.gov`. Note that the diurnal range is just over 1 m and, while the long-term rate of change in sea level is low (compared to more seismically active areas), there is substantial seasonal, interannual, and short-term variability. In 2009, an anomalous rise in sea level lasting several weeks at a number of east coast tide gauges was reported by Sweet *et al.* (2009).

3 Tide gauge data available at `opendap.co-ops.nos.noaa.gov/axis/`

Table 1: Specifications for the Nantucket, Massachusetts digital elevation model.

Coverage Area	70.67° to 69.49°W; 40.81° to 41.71°N
Coordinate System	Geographical decimal degrees
Horizontal Datum	World Geodetic System 1984 (WGS84)
Vertical Datum	Mean High Water (MHW)
Vertical Units	Meters
Cell Size	1/3 arc sec
Grid Format	ESRI Arc ASCII grid
Version Employed	Completed 10 October 2008

Table 2: Tidal characteristics of the Nantucket tide gauge.
Nantucket Island, Massachusetts: Station 8449130 (41°17.9′N, 70°05.8′W)
Established 04 October 1963—Present installation 18 September 1990

Tidal Datum and Range Values (Epoch 1983–2001)			
MHHW (Mean Higher High Water)	2.004 m	Great Diurnal Range 1.089 m	Mean Range 0.925 m
MHW (Mean High Water)	1.900 m		
MSL (Mean Sea Level)	1.454 m		
MLW (Mean Low Water)	0.976 m		
MLLW (Mean Lower Low Water)	0.915 m		
Sea Level Trends and Cycles			
Long-term Sea Level Trend	Increasing 2.95 ± 0.46 mm/yr		
Seasonal Cycle Range	Min. –38 mm (March); Max. +37 mm (October)		
Interannual Variation (from 1990)	Min. –13 mm (1994); Max. +19 mm (2010)		
Extremes to Date (February 2013)			
Maximum	3.313 m on 30 October 1991		
Minimum	0.262 m on 12 February 1981		

3.3 The CFL condition and other considerations for grid design

Water depth-dependent wave speed, in conjunction with the spacing of the spatial grid representation, places an upper limit on the time step permissible for stable numerical solutions employing an explicit scheme. This is the CFL (Courant-Friedrichs-Levy) limit, which requires careful consideration when the grids employed for a reference or forecast model are being designed. Finer-scale spatial grids, or greater water depths, require shorter time steps, thereby increasing the amount of computation required to simulate a specific real-time interval.

Another feature of the application of gridded numerical solutions to the tsunami wave problem is the shortening that the wave train encounters in moving from deep water onto the shelf. In deep water, a grid spacing of 4 arc min (of latitude and longitude, corresponding to ~7 km) is normally used to represent propagating wave trains with a typical wavelength of the order of a few hundred kilometers. The stored results of such propagation model runs are typically decimated by a factor of 4, resulting in a database of ~30 km spacing (and 1 min temporal sampling) with which to generate the boundary conditions for the outermost (A grid) of the nested

grids in a model solution. The extraction of the boundary conditions (of wave height and the two horizontal velocity components) is achieved by linear interpolation in space and time. To provide realistic interpolated values, the stored fields for these variables must be smoothly varying and have adequate sampling in space and time to resolve their structure. This necessitates the placement of the outer boundary of the forecast model domain well offshore.

3.4 Specifics of the model grids

The extents and resolutions of the nested grids were initially chosen by Aurelio Mercado (2009, personal communication), and were implemented in a preliminary version of the forecast model. While performing satisfactorily in various simulations, more stringent tests, conforming to current protocols, suggested the potential for instability under some micro- and mega-tsunami scenarios. The reference model was more susceptible to instability. As a result, the grids were redeveloped and are illustrated in **Figures 9**–**11**.

The A-grid domain extends from Cape May, at the southern tip of New Jersey, to Cape Sable, the southernmost point of the Nova Scotia peninsula. Water depths along the southern boundary reach 4795 m, and a number of seamounts of the New England chain are included. Among these is Bear Seamount, which rises to within 1100 m of the surface, with the potential to scatter incoming tsunami waves (Mofjeld *et al.*, 2001). The eastern boundary of the A grid is chosen to adequately represent waves propagating westward over Georges Bank and later waves possibly arriving at Nantucket via the Gulf of Maine. Tsunami wave trains investigated for this report are more likely to arrive at Nantucket Island from the south or southwest. By extending the southern boundary to the mainland near Cape May it is hoped that such waves are adequately represented. The A grids are compared in **Figure 9**; both the reference and forecast model versions share the same extent in latitude and longitude. The reference model employs the full 30-arc-sec GEBCO resolution in both directions while the forecast model A grid is smoothed and decimated to 60 arc sec. Full details are provided in **Tables 3** and **4**.

The B grids for both the reference and forecast model versions also share the same domain extent, employing almost the entire area covered by the NGDC DEM for Nantucket (Eakins *et al.*, 2009). It was curtailed slightly in the west to exclude Buzzards Bay and in the north to limit land coverage. The eastern and southern boundaries were chosen to include most of Nantucket Shoals. Tsunami wave access to Nantucket Sound (and the Nantucket warning point, which is in the harbor on the north side of the island) can come from the east via the Great Point Shoal Channel, from the south via the Muskeget Channel between Martha's Vineyard and Muskeget Island or several channels through Tuckernuck Bank, or from the west between Martha's Vineyard and the Massachusetts mainland. At this latitude, a 4:3 ratio of zonal to meridional grid cell extents (in degree units) results in almost square spatial cells, which is desirable for modeling purposes. The B grid extents are displayed in **Figure 10** with details provided in **Tables 3** and **4**.

Delineated with red rectangles in **Figure 11** are the differing extents of the reference and forecast model C grid domains. The extent of the forecast model C grid is curtailed in order to bring the forecast model run-time within the target

10 min per 4 hr of simulation time suited to use in an actual emergency situation. The tests in this report are designed to demonstrate that no significant loss in model accuracy between the reference and forecast model predictions results from restrictions in domain extent and spatial resolution. **Figure 11** contrasts the reference and forecast model C grids and details are given in **Tables 3** and **4**. The rectangle in the upper panel of **Figure 11** indicates the smaller region covered by the forecast grid seen in the lower panel.

Some smoothing and editing were necessary for all grids to eliminate erroneous points or grid features that tend to cause model instability. For example, "point" islands, where an isolated grid cell stands above water, are eliminated, as are narrow channels or inlets one grid unit wide; these tend to resonate in the numerical solution. Large depth changes between adjacent grid cells can also cause numerical problems; customized tools are available to correct many of these grid defects. An additional constraint on the bathymetry (Elena Tolkova, personal communication), which identifies excessive depth changes in the discrete representation, was applied.

Table 4 lists the maximum depth, the CFL time step requirement that must not be exceeded, and the actual time steps chosen for the reference and forecast model runs. Since the numerical solutions in the three grids proceed simultaneously, in the current version of MOST employed by SIFT, there is a requirement that the A and B grid time steps be integer multiples of the (innermost) C grid time step, in addition to satisfying their individual CFL requirements. For both reference and forecast models, the CFL requirement of the C grid was the most stringent. The values chosen are shown in **Table 4** and are such that an integer multiple of each time step (8 × for the forecast model, 24 × for the reference) is identically 30 sec, the chosen output time interval for both models (see Appendix A).

3.5 Model run input and output files

In addition to providing the model grid file names, the appropriate time step, and A and B grid multiples as provided in the tables discussed above, the designer must provide a number of additional parameters in an input file. These include the Manning friction coefficient (n), a depth threshold to determine when a grid point becomes inundated, and the threshold amplitude at the A-grid boundary that will start the model. An upper limit on wave amplitude is specified in order to terminate the run if the waves grow beyond reasonable expectation. Standard values are used: 0.0009 for the squared friction coefficient (n^2) and 0.1 m for the inundation threshold. The latter causes the inundation calculation to be avoided for insignificant water encroachments that are probably below the level of uncertainty in the topographic data. Inundation can, optionally, be ignored in the A and B grids, as is the norm in the (non-nested) MOST model runs that generate the propagation database. When A- and/or B-grid inundation is excluded, water depths less than a specified "minimum offshore depth" are treated as land; in effect, a "wall" is placed at the corresponding isobath. When invoked, a typical value of 1 m is applied as the threshold, although A and B inundation is normally permitted as a way to gain some knowledge of tsunami impact beyond the scope of the C-grid domain. Other parameter settings allow decimation of the output in space and/or time. As

noted above, 30 sec output has been the target and output at every spatial node is preferred. These choices avoid aliasing in the output fields that may be suggestive of instability (particularly in graphical output), when none, in fact, exists.

Finally, the input file (supplied in Appendix A) provides options that control the output produced. Output of the three variables—wave amplitude, zonal (positive to the east) velocity, and meridional (positive to the north) velocity—can be written (in netCDF format) for any combination of the A, B, and C grids. These files can be very large. A separate file, referred to as a SIFT file, contains the time series of wave amplitude at each time step at discrete cells of a selected grid. Normally, the time series at a reference or warning point, typically the location of a tide gauge,

Table 3: Specifics of the reference and forecast model grids employed for Nantucket, Massachusetts. For the paired values in the resolution and grid points columns, the zonal (east to west) value is listed first, followed by the meridional (north to south) value.

Reference Model for Nantucket, Massachusetts

Minimum offshore depth: 1 m; Water depth for dry land: 0.1 m; Friction coefficient (n^2): 0.0009; CPU time for a 4-hr simulation: 265 min

Grid	Zonal Extent		Meridional Extent		Resolution	Grid Points
A	74.90°W	65.40°W	39.00°N	43.50°N	30" × 30"	1141 × 541
B	70.60°W	69.50°W	40.81°N	41.70°N	8" × 6"	496 × 535
C	70.40°W	69.80°W	41.10°N	41.50°N	4/3" × 1"	1621 × 1441

Forecast Model for Nantucket, Massachusetts

Minimum offshore depth: 1 m; Water depth for dry land: 0.1 m; Friction coefficient (n^2): 0.0009; CPU time for a 4-hr simulation: 8.2 min

Grid	Zonal Extent		Meridional Extent		Resolution	Grid Points
A	74.90°W	65.40°W	39.00°N	43.50°N	60" × 60"	571 × 271
B	70.60°W	69.50°W	40.81°N	41.70°N	24" × 18"	166 × 179
C	70.35°W	69.85°W	41.20°N	41.45°N	4" × 3"	451 × 331

CPU times for a 4-hr simulation are based on use of a single Intel® Xeon® E5670 2.93GHz processor.

Table 4: Grid file names and grid-related parameters for Nantucket, Massachusetts. The time steps for the A and B grids must be integer multiples of the basic time step chosen for the C grid.

Grid	File Name	Maximum Depth (m)	Minimum CFL (s)	Model Time Step (s)	Water Cells
A	NantucketMA_RM_A	4794.6	3.325	2.50 (2×)	450,781
	NantucketMA_FM_A	4787.6	6.657	3.75 (1×)	112,920
B	NantucketMA_RM_B	143.42	4.926	2.50 (2×)	245,021
	NantucketMA_FM_B	141.92	14.858	2.0 (2×)	27,328
C	NantucketMA_RM_C	51.34	1.375	1.25	2,204,293
	NantucketMA_FM_C	44.84	4.429	3.75	121,058

is selected to permit validation in the case of future or historical events. Due to the protected location of the Nantucket warning point (the tide gauge site), several additional sites that are more exposed to potential tsunami impact were specified during development and are discussed in Section 4 of this report. The SIFT file also includes the distribution of the overall minimum and maximum wave amplitude and speed in each grid. By contrast with the complete space-time results of a run, the SIFT file (also netCDF) is very compact.

By default, two additional output files are generated. The "listing" file summarizes run specifications, progress, and performance in terms of run time, as well as information to determine the reason, should a run not start or terminate early. The "restart" file is produced so that a run can be resumed from the time it ended, either normally or by operator intervention.

The input files described above are specific to the model itself. For an actual run, the program must be pointed toward the files that contain the boundary conditions of wave amplitude (H) and velocity components (U, V) to be imposed at the A-grid boundary. Time-varying conditions are generally extracted as a subset of a basin-wide propagation solution (either a single unit source or several, individually scaled and linearly combined) that mimics a particular event. These boundary-forcing files typically consist of 24 hr of values (beginning at the time of the earthquake), sampled at 1 min intervals and available on a 16 arc min grid. Occasionally, for more remote seismic sources, such as the South Sandwich subduction zone arc, the time span of the propagation run available for forcing is extended beyond one day. The seismic sources employed during the development and discussion of the Nantucket model are listed in **Table 5** and illustrated in **Figures 12**, **13**, and **14**.

Table 5: Synthetic tsunami scenarios employed for Nantucket, Massachusetts model testing.

Scenario	Source Zone	Tsunami Source	α [m]
Mega-tsunami (Mw 9.3) Scenario			
ATSZ 48–57	Atlantic, North of Puerto Rico	A48–57, B48–57	25
ATSZ 82–91	Caribbean, South of Hispaniola	A82–91, B82–91	25
ATSZ 38–47	Atlantic, East of Puerto Rico	A38–47, B38–47	25
ATSZ 58–67	Caribbean, Cayman Trough	A58–67, B58–67	25
ATSZ 68–77	Caribbean, Gulf of Honduras	A68–77, B68–77	25
SSSZ 1–10	South Sandwich Subduction Arc	A1–10, B1–10	25
HS 1–2	Eastern Atlantic	Ad hoc non-unit source	
Mw 7.5 and 7.8 Scenario			
ATSZ B52	Atlantic, North of Puerto Rico	B52	1
ATSZ B53	Atlantic, North of Dominican Republic (mimics 1946 event)	B53	2.81
Micro-tsunami Scenario			
SSSZ B11	South Sandwich Subduction Arc	B11	0.01

4. Results and Discussion

Before proceeding to an extensive suite of model runs that explore the threat to Nantucket Island, Massachusetts, from various source regions, the stability of the model is tested in both low and extreme amplitude situations. The former we refer to as "micro-tsunami" testing, where the boundary forcing is at such a low level (but not precisely zero) that the response is expected to be negligible. This test can be highly valuable in revealing localized instabilities that may result from undesirable features in the discretized bathymetric representation. Inlets or channels that are only one grid-cell wide may "ring" or resonate in a non-physical way in the numerical solution. Land-locked water bodies, particularly if poorly resolved, can oscillate or develop unrealistic water levels. While an instability may not grow large enough to cause the model to fail, in a run with typical tsunami amplitudes, its presence may be masked by actual wave variability.

Forcing by extreme events, which we refer to as "mega-tsunami" events, is also tested. In addition to the need to test model stability under such circumstances, there is a parameter in the input file that truncates the run if a prescribed threshold is exceeded. For operational use, the threshold must be set high enough so that an extreme event run is not unnecessarily terminated. Tests should be performed for synthetic sources whose waves enter the model domain from different directions since, although stable for one set of incoming waves, an instability may be encountered for another. The micro- and mega-tsunami event testing of the forecast and reference models is reported in the following subsections. The tests employ the standard set of synthetic scenarios recommended for Atlantic forecast model development, listed in **Table 5**. An additional mega-tsunami source in the eastern Atlantic near Portugal is included.

Further evidence of stability is provided by the extensive set of scenarios aimed at exploring the dependence of impact on source location, described later, and in independent testing by other members of the NCTR team before the revised model is released for operational use.

4.1 The micro-tsunami tests

The standard synthetic scenario for this purpose employs unit source SSSZ B11 (see **Figure 13**) in the South Sandwich subduction zone. The forcing files from the propagation database (Gica *et al.*, 2008; see Appendix B) were scaled down by a factor of 100 so as to mimic a Mw 6.1667 / Slip 0.01 m "micro"-source rather than the Mw 7.5 / Slip 1 m standard. A number of grid cells in the B and C grids emerged as potential sources of instability. These were generally minor indentations of the coastline barely resolved by the grids, or narrow channels. A limited number of grid cells in the outermost (A) grid required correction. After an iterative process of grid correction and retesting using the micro-source, both of the reference and forecast model grids were deemed satisfactory and the testing of large-scale events

could begin. The upper panel (a) of **Figure 15** illustrates a step in the process where a deficiency in the reference model grid generated a mild instability (in the SSSZ B11 micro-tsunami scenario), causing the reference model time series at the reference point, initially in close agreement with the forecast model, to develop unrealistic, high-frequency oscillations. Though not growing without bound, such features could behave erratically in simulating real events. Modification of the reference model bathymetry eliminated the problem, as seen in the middle panel (b) of **Figure 15** where the reference and forecast model time series at the warning point are in good agreement. The lower panel (c) shows good agreement of the reference and forecast model solutions in Madaket Harbor, an inlet north of the Madaket Beach spit, over the period simulated. A weak high-frequency oscillation had been evident near Madaket late in the micro-tsunami run. The final round of adjustments to the forecast model C grid removed this artifact.

4.2 The mega-tsunami tests

As has been found for other forecast models along the U.S. eastern seaboard, the greatest tsunami threat is associated with the Puerto Rico Trench, north of that island. A synthetic "mega-tsunami" is simulated by linearly combining 20 unit sources from the propagation database (see Appendix B) and scaling up the slip in each by a factor of 25. As described by Gica *et al.* (2008), each unit source represents a 100×50 km area of the fault surface with the long axis parallel to the plate boundary. The B row is shallowest, sloping from a nominal depth of 5 km (unless a depth estimate has been provided by the USGS based on the earthquake catalogs), row A is deeper, followed by rows Z, Y, X, . . .where appropriate. Thus, the extreme case sources represent 1000 km long ruptures with a width of 100 km; the corresponding moment magnitude is Mw 9.3.

We focus first on the mega-source ATSZ 48–57 (see **Figure 12**) with impacts summarized in **Figures 16–21**. The simulated reference and forecast model maximum amplitude (H_{max}) results are compared in **Figure 16**. Here, the full extent of the C grid is displayed for both models to confirm that no unrealistic behavior is seen along the boundary of the curtailed forecast model domain. The agreement between the reference and forecast model amplitude distributions is good, with similar structures in each. The greatest amplitude is seen along the shoal to the east of the island and along the southeast coast. Land areas are colored grey in order to accentuate with color those areas that are inundated. A black line delineates the undisturbed MHW coastline. The most noticeable difference between the reference and forecast model distribution of H_{max} is the degree to which offshore features are blurred in the forecast model representation. It is well known that small-scale bathymetric features can focus or disperse tsunami waves, and the relative coarseness of the forecast C grid is evidently blurring some alongshore spatial structure. Larger-scale features, however, such as the weaker coastal impact near the midpoint of the south coast, are captured in the forecast model results. Several points (1–6) around the coast are marked in the lower panel of **Figure 16**; time series from these locations will be presented to compare the reference and forecast model results. They are:

1. The Nantucket warning point, the tide gauge location in the main harbor;
2. Madaket Beach;
3. Nantucket Memorial Airport, south end of main runway;
4. Tom Nevers Beach;
5. Siasconset Beach; and
6. Great Point Spit, the east-facing side.

Impacts at these sites are discussed for this (ATSZ 48–57) and subsequent synthetic scenarios. Notice an almost ten-fold reduction of maximum wave amplitude in both representations along the northern coastline that faces Nantucket Sound. In some island locations, such as American Samoa during the 2009 event, tsunami waves wrap around the island resulting in similar impacts in the lee as to the coast facing the source. For Nantucket's north shore, the constricted entrances to the sound appear to greatly attenuate the wave field.

In the companion **Figure 17**, the distributions of maximum speed (S_{max}) in the reference and forecast model predictions for the synthetic ATSZ 48–57 scenario are contrasted. The agreement is close, perhaps exceeding that for the H_{max} fields, in the magnitude and location of prominent features of the speed distribution. A prominent feature in speed extends northeast from Great Point, the most northerly point on the island. The steeply shoaling bathymetry in this region, evident in **Figure 11**, is named Great Point Rip. Other offshore loci of extreme S_{max} can be associated with other known "rips" along the east coast where submerged sand waves approach the surface. Strong nearshore currents are found in the southeast between Tom Nevers Beach and Siasconset, and to the west where the Madaket Beach area becomes inundated in this mega-tsunami scenario.

To confirm the agreement between the reference and forecast model results, the time series of wave height at the six sites indicated in **Figure 16** are compared in **Figure 18**. For this, and for subsequent figures of the same type, the Nantucket warning point has its own vertical scale while the remaining five sites are assigned a common scale. The model runs extend for 18 hr beyond the time at which the waves first exceeded the threshold value at the A-grid boundary, and the common horizontal axis is marked in hours since the "event." The degree of agreement between the reference and forecast model solutions is good, although the forecast model series do show a tendency to "spikes" exceeding those in the reference model series. Three times are highlighted with green arrows as representing the arrival time of the first wave peak at three sites: (a) Siasconset, (b) Great Point Spit, and (c) the Nantucket tide gauge. In **Figures 19–21**, "snapshots" of the wave amplitude and current vector fields from the reference and forecast models are compared. To facilitate the comparison, the reference model results are limited to the forecast model C-grid domain, and both vector fields are decimated with the same subsampling. In **Figure 19**, waves appear to impinge first on the coast near Madaket then progress counterclockwise around the island. Arrival at the Nantucket tide gauge is approximately one hour later than at Madaket.

Figure 19 is the first "snapshot," when the leading wave crest has just reached Siasconset. The current vectors indicate the wave is receding from the south and southwestern part of the island, having inundated the low-lying areas, and is beginning to flood into Nantucket Sound around Tuckernuck and Muskeget islands. To the east, the wave is beginning to proceed northward into an essentially quiescent region. The reference and forecast model amplitude and current vector fields are in good agreement with the exception of the extreme southwest corner, where the second wave in the reference model solution is beginning to arrive, suggesting a slight mismatch in the reference and forecast model timing. The overall impression from this sample time is that the solutions are in good agreement.

Figure 20 contrasts the solutions at a time when the leading wave has reached the Great Point Spit sample point. Inundation of the low-lying area southwest of Siasconset has progressed from that seen in **Figure 19**, and Great Point Spit has been overtopped. For this (ATSZ 48–57) scenario, penetration of Nantucket Sound from the west has preceded that from the east, and the water level at the Nantucket tide gauge has begun to rise as a result. While the agreement between the reference and forecast model solutions is good overall, some differences are apparent. Flooding into the large Sesachacha Pond, midway up the east coast, has begun in the forecast model, though, evidently, the barrier to the ocean in the reference model has yet to be overwhelmed. As before, the greatest disparity lies to the southwest of Madaket where the reference model leads, or is more structured than, the forecast model equivalent.

In **Figure 21**, the solutions are compared at the time of the first wave peak at the Nantucket tide gauge. Inundation of the Great Point area and the triangle of land north of the eastern end of Nantucket Harbor (named Head of the Harbor) is extensive, but greater in the forecast model results. The eastern portion of Nantucket Sound appears to be draining through the channel north of Great Point Rip, south of which the currents are to the south–southeast. Confused, though generally consonant, current and wave height patterns are seen in the east. With the exception of Sesachacha Pond, which remains unaffected in the reference model, the patterns of inundation in the reference and forecast model solutions are consistent. To summarize, the H_{max}, S_{max}, time series, and individual snapshots from the reference and forecast model solutions for this scenario are in good agreement.

Next, we examine the results from the ATSZ 82–91 mega-tsunami scenario. This source combination represents an event in the Los Muertos Trough region south of Puerto Rico (see **Figure 12**). To be expected is a reduced impact in the North Atlantic as the waves are constrained to emerge through the Windward and Mona passages, west and east of Hispaniola, respectively. The results are presented in a set of graphics that parallel those employed above in the discussion of the ATSZ 48–57 scenario. **Figures 22** and **23** contrast the maximum wave amplitude and current speed fields (H_{max} and S_{max}, respectively) from the reference and forecast model solutions over an 18-hr period. As will be seen, in the time series comparisons of **Figure 24**, the wave train from this simulated event has longer wave periods than those seen for the source north of Puerto Rico. The leading wave of the ATSZ 82–91 event arrives at Nantucket as a trough. In **Figure 22**, the maximum wave amplitude is only one-fifth that of the previous scenario but

still occurs offshore near the eastern "rips" and near Great Point where the bathymetric step causes growth of the waves. Waves are also strong along the south coast and, probably as a result of the longer waves in this scenario, there is less of the fine-scale structure in H_{max} that reduced the agreement between the reference and forecast model results of the ATSZ 48–57 scenario. There appears to have been a slight inundation of the smaller Coskata Pond in the forecast model solution that is absent in the reference model distribution of H_{max}. To the west of Nantucket Harbor, there is evidence of waves of a half meter or so in excess of any seen in the harbor itself, and the reference and forecast model representations of their amplitude and distribution match well. The S_{max} distributions, as seen in **Figure 23**, are also in good agreement, with the strongest currents predicted in the vicinity of Great Point Rip.

The time series comparisons for the Los Muertos Trough scenario (ATSZ 82–91) are shown in **Figure 24**. As for the source north of Puerto Rico, the wave train appears to arrive first at the west end of the island (Madaket Beach) and progress counterclockwise, arriving some 90 min later at the Nantucket tide gauge. The agreement between the reference and forecast model time series at all six sites is quite good, with one noticeable difference at the tide gauge ~10 hr into the simulation, where the forecast model solution appears to miss a peak. Green arrows labeled A, B, and C identify selected times for "snapshot" comparison in **Figures 25**, **26**, and **27** as the leading trough arrives off Siasconset, Great Point Spit, and the Nantucket tide gauge, respectively. In **Figure 25**, the leading trough has reached Siasconset while the crest that follows is entering the domain in the southwest. Perhaps due to the longer period and larger scale of the waves in this scenario, there is excellent agreement between the reference and forecast model solutions everywhere for both the wave height and the direction and strength of the current vectors. Water is being drawn from the western part of Nantucket Sound around Tuckernuck and Muskeget islands to build the incoming wave while, to the east, a strong southward flow is evident. In **Figure 26**, as the wave trough arrives near the Great Point Spit, there is a strong convergence of currents in the northwest of the domain, with water being drawn eastward out of Nantucket Sound via the channel north of Great Point Rip and south from the vicinity of the spit to build the following wave crest. The leading wave crest from the southwest in the previous snapshot has progressed into the western portion of Nantucket Sound. Finally, in **Figure 27**, as the leading trough is felt at the Nantucket tide gauge, there is strong flow into Nantucket Sound from both the west and the east, and a train of waves appears to propagate up the east coast. Within and in the vicinity of Nantucket Harbor, there is good agreement in the wave amplitude field and in the current speed and direction.

4.3 Simulation of the remaining synthetic mega-tsunamis

Three other mega-tsunami scenarios originating in the ATSZ source area (see **Table 5**) were investigated with similarly positive results for agreement between their reference and forecast model representations. The first of these is ATSZ 38–47 (see **Figure 12**), north of the Antillies but east of the ATSZ 48–57 scenario that has the greatest impact on the Nantucket region of the cases considered. **Figures 28**

to **30** illustrate the H_{max}, S_{max}, and time series comparisons. While the time series at the six sample sites (in **Figure 30**) are in reasonable agreement with regard to the timing of peaks and troughs throughout the 18 hr simulation, there are noticeable differences in the heights seen in the reference and forecast model versions. This translates into visible differences in the H_{max} and S_{max} distributions. Forecast model values exceed those from the reference model in the southeast, and there is inundation of the low-lying Tom Nevers area in the forecast model that is absent in the reference model version. For the southwest coast of Nantucket Island and in the rip area off the southeast coast, the reference model solution, as measured by H_{max} and S_{max}, exceeds that resulting from the forecast model. The solutions are not grossly different, and within Nantucket Sound and the harbor, the fields match well. Inundation is limited and, with the exception of the Tom Nevers area mentioned above, agrees well between the reference and forecast model results.

The next mega-tsunami scenario discussed is ATSZ 58–67 to the west of Puerto Rico (see **Figure 12**), comprising much of the Cayman Trench. The unit sources combined for this composite are mainly screened from the North Atlantic by the Turks and Caicos Islands and Cuba, and should be less capable of causing a major impact to Nantucket than scenarios ATSZ 48–57 or ATSZ 38–47. This conjecture is borne out by the results presented in **Figures 31–33**. There is good agreement between the reference and forecast model results for H_{max} and S_{max} and the six sample time series. A similar result is true of the ATSZ 68–77 mega-tsunami scenario composed of unit sources entirely within the Caribbean, between Honduras and Jamaica (see **Figure 12**). An 1856 earthquake of magnitude 7.6 in the Gulf of Honduras (Lander and Lockridge, 1989) generated a local tsunami but was not reported elsewhere. As was seen for the other intra-Caribbean mega-tsunami source ATSZ 82–91, the waves arriving at Nantucket have longer periods and wavelengths than those originating from sources in the Atlantic. The results, presented in **Figures 34–36**, show excellent agreement between the reference and forecast model versions. The apparent slight anomalies are a weak high-frequency component in the east coast sample time series late in the reference model run and an elevated response in the H_{max} field of the forecast model for North Pond in the northwest corner of Tuckernuck Island.

Completing the set of unit source-based mega-tsunami scenarios is SSSZ 01–10, associated with the South Sandwich subduction zone (see **Figure 13**). The results of the reference and forecast model comparison are presented in **Figures 37–39**. The wave amplitudes are larger than might be expected for such a remote source, with waves of up to 1 m near Great Point. This is likely the result of topographic steering by the mid-Atlantic Ridge. The match between reference and forecast model results is again good throughout the duration of the model run, which is slightly reduced from 18 hr as a result of the limited duration of the propagation model forcing available. Approximately 15 hr elapse before the waves encounter Nantucket's A-grid boundary.

The propagation database currently contains no unit sources representative of the eastern Atlantic. Despite its strength, there is question regarding the source of the 1755 Lisbon earthquake and tsunami. The Gulf of Cadiz and the region west of Cape St. Vincent have numerous fault lines (Baptista *et al.*, 2003; Duarte *et al.*,

2010), some of which have been proposed as potential sources. While this report does not purport to model the 1755 event, it is deemed necessary for completeness in the stability testing of the Nantucket forecast model that an eastern Atlantic source be included. Previous experience has shown that differences in source direction may potentially expose an instability in a set of model grids, and Barkan *et al.* (2009) have discussed the threat to the east coast from such sources.

Available at NCTR from other studies (for the Nuclear Regulatory Commission and the USGS) are propagation solutions for two rectangular areas: one at 106×70 km represents the Horseshoe Fault, the other at 88×70 km represents the Marqués de Pombal fault zone. The two solutions are combined using the ComMIT (Community Modeling Interface for Tsunamis) tool (Titov *et al.*, 2011) and rescaled to represent a magnitude 9.3 mega-tsunami with evenly distributed slip designated HS 01–02 in **Table 5**. This composite source representing the eastern Atlantic is applied to the Nantucket reference and forecast models. The results are presented in **Figures 40–42** using the same format employed for the unit source-based scenarios described above. Within the domain common to the forecast and reference model C grids, there is reasonable agreement between the H_{max} and S_{max} fields, though the reference model fields exhibit more fine-scale structure. In the southern part of the reference model domain, near 41.15°N, 70°W in **Figure 40**, there is an area of strong H_{max} response that was not encountered in other scenarios. The feature is less prominent in the S_{max} field (**Figure 41**) and there is no evidence that its influence extends beyond the immediate area. In particular, there appears to be good agreement between the reference and forecast model results in the most strongly impacted area between Tom Nevers Beach and Great Point. The time series of **Figure 42** confirm this conclusion, though the forecast model has more pronounced peaks and, in the case of the Nantucket tide gauge, the reference to forecast model agreement deteriorates later in the solution.

4.4 Intermediate magnitude synthetic scenarios

Two further scenarios, listed in **Table 5** and illustrated in **Figure 12**, are employed in the Nantucket model testing. The first of these, designated ATSZ B52, is part of the standard forecast model testing protocol and consists of a single unit source, representing an intermediate magnitude Mw 7.5 event. The second, again a single propagation database element (ATSZ B53), is scaled up by a factor of 2.81 as an ad hoc representation of an 1946 Dominican Republic event of magnitude Mw 7.8. This was observed weakly along the U.S. east coast (Lander and Lockridge, 1989).

The results for scenario ATSZ B52 are presented using the same style employed for the mega-tsunami scenarios: time series for the six standard locations along the Nantucket shore and H_{max} and S_{max} comparison fields. The time series in **Figure 43** suggest a poorer level of agreement than was obtained with the mega-tsunami scenarios. Though there is general agreement between the reference and forecast model time series, disparities in the maxima are apparent, with peaks and troughs in the reference model series considerably exceeding those found in the forecast model results. The H_{max} comparison shown in **Figure 44** reinforces this impression and there appears to be excessive forecast model response in Coskata Pond

and North Pond at the west end of Tuckernuck Island. The S_{max} comparison shown in **Figure 45** also shows disparities.

The origin of the greater disparity in the ATSZ B52 results over that seen for ATSZ B48–57, which includes unit source B52, appears to lie in the spatial structure of the wave field. The H_{max} fields for a subregion of the forecast model's A grid for B52 and for a number of its neighbors are shown in **Figure 46**. Selected isobaths (20 m, 50 m, 100 m, 200 m, 500 m, 1000 m, and 2000 m) are overlaid to indicate the bathymetry (see also **Figure 9**). There is considerable alongshore structure in the response. Numerous lobes of enhanced response associated with bathymetric features are evident along the continental slope, the strongest (for sources B50–52) occurring south of Nantucket Shoals. A low level of H_{max} is seen at the Hudson Canyon in the western portion of the A grid; greater wave speed in canyons tends to cause wave energy to converge on the shallower water along their flanks. Nantucket Shoals projects south as a rather narrow feature and may be a convergence region with wave energy incident from the deeper waters to the east and west. To the extent that short-scale features are less accurately represented in the lower-resolution forecast grids, it is not suprising that the solutions inshore of such features differ.

The question arises whether the results from synthetic single unit source scenarios, such as ATSZ B52, warrant a redefinition of the forecast model grids. Tests were conducted to ascertain how many other unit sources give similar responses, and how the effect might be mitigated by enhanced forecast model grid resolution. A forecast model A grid with an intermediate (60×45 rather than 60×60 arc sec) resolution was explored, together with extending the B-grid domain in both the reference and forecast model to the shelf break. The strong narrow lobe south of Nantucket Shoals was found to decline for unit sources west and east of the cluster B50–52. The disparity in the reference and forecast model time series on the island is not fully eliminated by the enhanced forecast model grid resolution, and a considerable run-time penalty (almost a doubling) is incurred. A further possibility is that the coarseness of the stored propagation database results, relative to the scale of the Nantucket Shoals feature, is the source of the problem.

The distribution of the maximum amplitude (in cm) for all B row unit sources of the ATSZ is shown graphically in **Figures 47** and **48**. The upper panel of Figure 47 shows the unit source rectangles, color coded with the impact each causes at the Nantucket warning point. The strongest impacts come from the area of the Puerto Rico Trench. The unit sources used to create **Figure 46** are indicated. The remaining panels of **Figures 47** and **48** show the corresponding distributions of impact for the five sites on the south and east coasts. A common color scale is employed to facilitate intercomparison; it appears that for unit source forcing (Mw 7.5) the impact at Nantucket is typically one-third that of the more exposed sites. The center of maximum amplitude differs slightly with impact site but generally lies north and east of Puerto Rico. Elsewhere, unit sources adjacent to passes through the islands or east of Trinidad, where the main beam of the tsunami is likely to be directed more northward, have enhanced impact on Nantucket Island.

As noted earlier, no historical records of tsunami impact to Nantucket are available. To partially fill this gap, the results for the ATSZ B53 scenario, an

ad hoc representation of the 1946 Dominican Republic tsunami, are presented in the same format employed for scenario ATSZ 48-57. **Figure 49** compares the time series. While those from the reference model show some crests and troughs with amplitudes exceeding their forecast model equivalents, the overall degree of agreement is better than was seen for the ATSZ B52 scenario (**Figure 43**). In particular, the agreement in the first wave amplitudes and arrival times is better: comparable to that seen with the mega-tsunami comparisons. The structure of the H_{max} and S_{max} fields, shown in **Figures 50** and **51**, respectively, are similar, though the maximum wave amplitudes along the south coast in the forecast model solution are weaker than in the reference model. Comparisons of the wave amplitude and vector current distributions are made at three times, indicated with green arrows A, B, and C in **Figure 49**. In all three—**Figure 52**, where the wave reaches Siasconset, **Figure 53**, where it reaches Great Point Spit, and **Figure 54**, where it enters Nantucket Harbor—there is good agreement between the reference model (upper panel) and forecast model (lower panel) results. These results reinforce the impression that more extensive and highly resolved forecast model grids should not be pursued at present. In terms of impact to Nantucket, wave amplitudes of 15 cm or less (less than 5 cm at the tide gauge) are predicted. Since this proxy for one of the largest seismic events of the last century was located in the region to which New England is most vulnerable, it would appear that only events with magnitudes exceeding Mw 8.0 will be of concern to Nantucket, Massachusetts.

5. Conclusions

In addition to the scenarios run by the author and reported here, further tests have been made by the NCTR, and will continue to be made by staff at the TWCs and others, perhaps in training situations. Among the many related tools developed at NCTR is ComMIT (Titov *et al.*, 2011), which provides a highly intuitive graphical environment in which to exercise and explore forecast models for any combination of propagation database unit sources. Were any of these avenues to reveal a problem with the model, its origin (most likely in some quirk of the bathymetric files) would be located and corrected, then the revised version re-installed for operational use.

With the exception of the modest mismatch of the reference and forecast model predictions for singleton unit sources in the vicinity of ATSZ B52, the agreement between the model solutions appears quite acceptable. Actual events likely to pose a threat to Nantucket, Massachusetts, are those involving several unit sources. The results for the ATSZ 48-57 scenario suggest better agreement for more extended sources, and it is recommended that the set of forecast model grids developed and described in this report be adopted for operational use. As noted earlier, experiments with more extensive and highly resolved grids suggested that a major increase in model run-time, well above the currently recommended target of 10 min per 4 hr of simulation, would be required to achieve a significant improvement in forecast performance for short spatial-scale sources. The development of the forecast system is a dynamic process, with improvements to bathymetric datasets and revisions to the propagation database likely to continue. Use of supercomputers, rather than the current paradigm of workstations, for forecast computations may permit the current limits on run time and operationally feasible model resolution and extent to be relaxed.

6. Acknowledgments

A preliminary set of forecast model grids for Nantucket, Massachusetts, was produced in 2008 by Aurelio Mercado of the University of Puerto Rico, Mayaguez, and employed in earlier versions of SIFT. Members of the NCTR group provided valuable assistance during the production of this report. In particular, Liujuan Tang edited the first draft for content and style; grid stability test animations and the cover imagery were generated by Jean Newman; and SIFT testing was performed by Lindsey Wright. MassGIS is an online resource for Massachusetts geographic information. Hurricane and storm track data and an inundation chart were obtained from National Hurricane Center and USACE publications. The modeling could not proceed without the detailed DEM produced at NGDC by the painstaking combination of numerous bathymetric and topographic surveys. This publication is partially funded by the Joint Institute for the Study of the Atmosphere and Ocean (JISAO) under NOAA Cooperative Agreements NA17RJ1232 and NA10OAR4320148. This is JISAO Contribution No. 2108, PMEL Contribution No. 3400, and NOAA ISI ID290.

7. References

Baptista, M.A., J.M. Miranda, F. Chierici, and N. Zitellini (2003): New study of the 1755 Earthquake source based on multi-channel seismic survey data and tsunami modeling. *Nat. Haz. and Earth System Science, 3*, 330–340.

Barkan, R., U.S. ten Brink, and J. Lin (2009): Far field tsunami simulations of the 1755 Lisbon earthquake: Implications for tsunami hazard to the US East Coast and the Caribbean. *Marine Geology, 264*(1), 109-122.

Census Bureau (2010): United States Census Bureau American FactFinder Community Facts. URL: `factfinder2.census.gov/faces/nav/jsf/pages/index.xhtml`.

Duarte, J.C., P. Terrinha, F.M. Rosasa, V. Valadares, L.M. Pinheiro, L. Matias, V. Magalhaes, and C. Roque (2010): Crescent-shaped morphotectonic features in the Gulf of Cadiz (offshore SW Iberia). *Marine Geology, 271*(3 4), 236–249.

Dunbar, P. (2007): Increasing public awareness of natural hazards via the internet. *Nat. Hazards, 42*(3) doi:10.1007/s11069-006-9072-3, 529–536.

Eakins, B.W., L.A. Taylor, K.S. Carignan, R.R. Warnken, E. Lim, and P.R. Medley (2009): Digital Elevation Model of Nantucket, Massachusetts: Procedures, Data Sources and Analysis. NOAA Technical Memorandum NESDIS NGDC-26, Dept. of Commerce, Boulder, CO, 29 pp.

Fine, I.V., A.B. Rabinovich, B.D. Bornhold, R.E. Thomson, and E.A. Kulikov (2005): The Grand Banks landslide-generated tsunami of November 18, 1929: Preliminary analysis and numerical modeling. *Marine Geology*, *215*(1), 45–57.

Gica, E., M. Spillane, V.V. Titov, C.D. Chamberlin, and J.C. Newman (2008): Development of the forecast propagation database for NOAA's Short-term Inundation Forecast for Tsunamis (SIFT). NOAA Tech. Memo. OAR PMEL-139, NTIS: PB2008-109391, 89 pp.

Holbrook (1924): An account of a sailing adventure from 1879. *New York Times*, Letters to the Editor, 16 August 1924.

Inquirer and Mirror, (2012): Nantucket's bout with Hurricane Sandy. `http://www.ack.net/SandyPhotoJournal102912.htm`.

Lander, J.F., and P.A. Lockridge (1989): United States tsunamis (including United States possessions): 1690–1988. US Department of Commerce, NOAA, NESDIS, and NGDC, Publication 41-2, 265 pp.

McAdie, C., C. Landsea, C.J. Neumann, J.E. David, and E.S. Blake (2009): Tropical Cyclones of the North Atlantic Ocean, 1851-2006: With 2007 and 2008 Track Maps Included. US Department of Commerce, NOAA, NWS, and NESDIS.

Mofjeld, H.O., V.V. Titov, F.I. González, and J.C. Newman (2001): Tsunami scattering provinces in the Pacific Ocean. *Geophys. Res. Lett., 28*(2), doi:10.1029/2000GL011710, 335–337.

Percival, D.B., D.W. Denbo, M.C. Eble, E. Gica, H.O. Mofjeld, M.C. Spillane, L. Tang, and V.V. Titov (2011): Extraction of tsunami source coefficients via inversion of DART® buoy data. *Nat. Hazards, 58*(1), doi:10.1007/s11069-010-9688-1, 567–590.

Spillane, M.C., E. Gica, V.V. Titov, and H.O. Mofjeld (2008): Tsunameter network design for the U.S. DART® arrays in the Pacific and Atlantic oceans. NOAA Tech. Memo. OAR PMEL-143, 165 pp.

Sweet, W., C. Zervas, and S. Gill (2009): Elevated East Coast Sea Level Anomaly: June–July 2009. NOAA Tech. Report NOS CO-OPS 051.

Titov, V., and F.I. González (1997): Implementation and testing of the Method of Splitting Tsunami (MOST) model. NOAA Tech. Memo. ERL PMEL-112, NTIS: PB98-122773, NOAA/Pacific Marine Environmental Laboratory, Seattle, WA, 11 pp.

Titov, V.V., and C.E. Synolakis (1998). Numerical modeling of tidal wave runup. *J. Waterw. Port Coast. Ocean Eng., 124*(4), 157–171.

Titov, V.V., C. Moore, D.J.M. Greenslade, C. Pattiaratchi, R. Badal, C.E. Synolakis, and U. Kânoğlu (2011): A new tool for inundation modeling: Community Modeling Interface for Tsunamis (ComMIT). *Pure Appl. Geophys., 168*(11), 2121–2131, doi:10.1007/s00024-011-0292-4.

USACE (1997): Southern Massachusetts Hurricane Evacuation Study Technical Data Report, Department of the U.S. Army Corps of Engineers, New England Division, 260 pp. `http://www.nae.usace.army.mil/Portals/74/docs/topics/HurricaneStudies/MA/Nantucket.pdf`.

Wei, Y., E. Bernard, L. Tang, R. Weiss, V. Titov, C. Moore, M. Spillane, M. Hopkins, and U. Kânoğlu (2008): Real-time experimental forecast of the Peruvian tsunami of August 2007 for U.S. coastlines. *Geophys. Res. Lett., 35*, L04609, doi:10.1029/2007GL032250.

FIGURES

Figure 1: Nantucket, as seen from the International Space Station, lies south of the Massachusetts mainland and southeast of Martha's Vineyard.

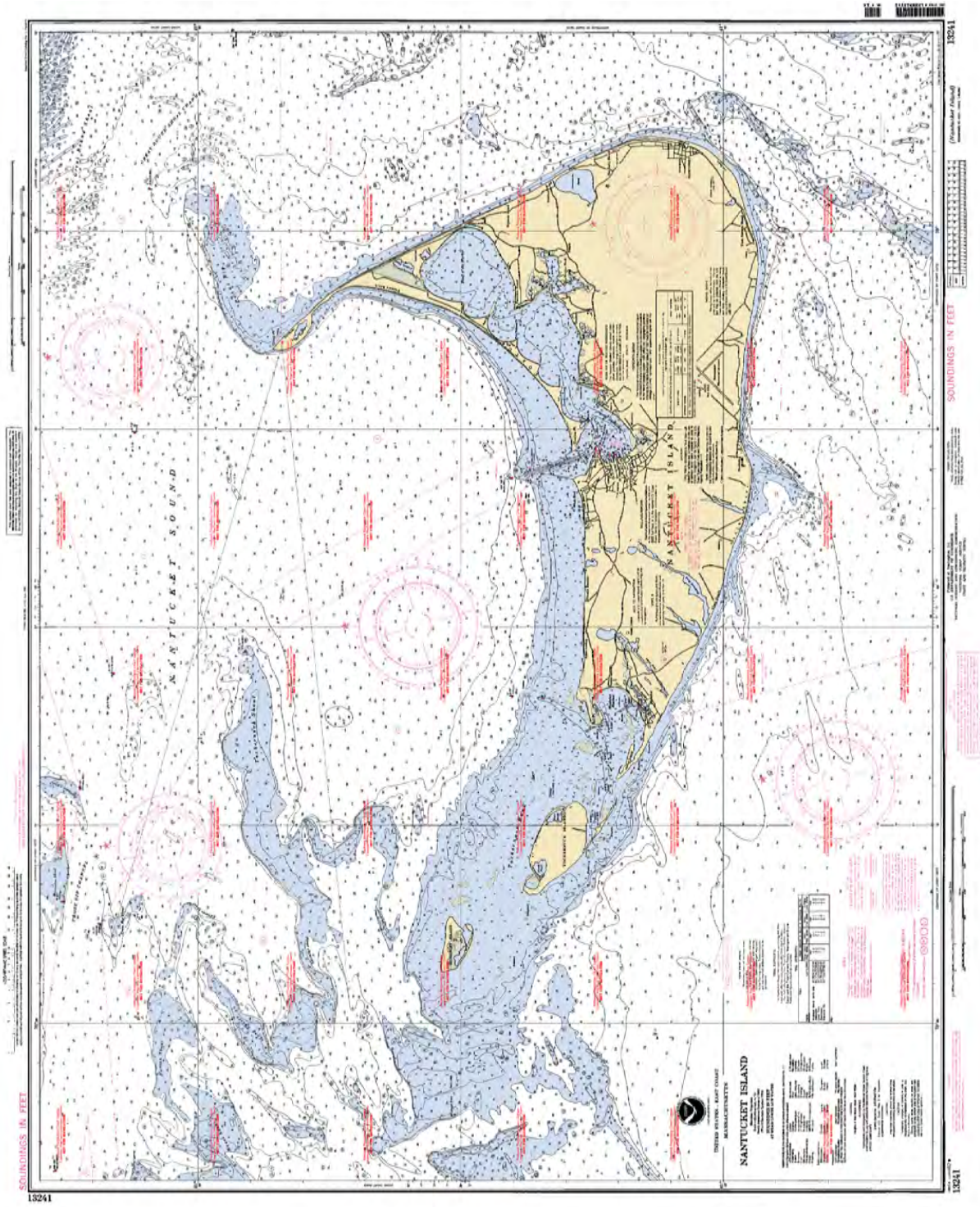

Figure 2: NOAA Chart 13241 for Nantucket Island and the smaller Tuckernuck and Muskeget islands at its west end. The tsunami warning point is at the tide gauge in the harbor on the north side; its entrance has a dredged channel leading into the shallow Nantucket Sound.

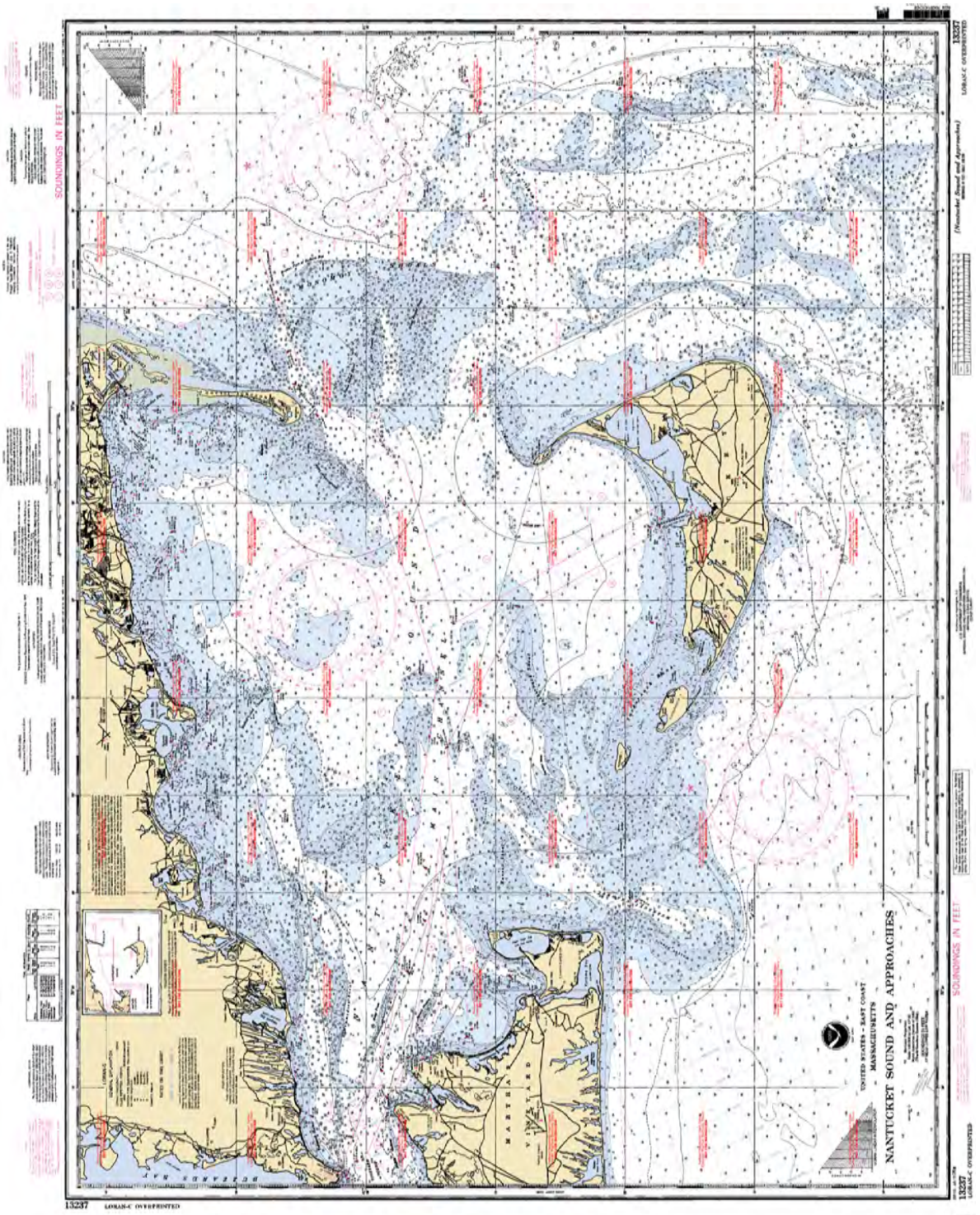

Figure 3: NOAA Chart 13237 for Nantucket Sound with its extensive shoals. The deeper access channels are Great Round Shoal Channel, near Great Point at the northeast end of Nantucket Island, and Muskeget Channel, close to Martha's Vineyard.

Figure 4: Nantucket's harbor area from Google Earth, annotated with the tide gauge location on Steamboat Wharf, which is elevated on piles and is the ferry terminus.

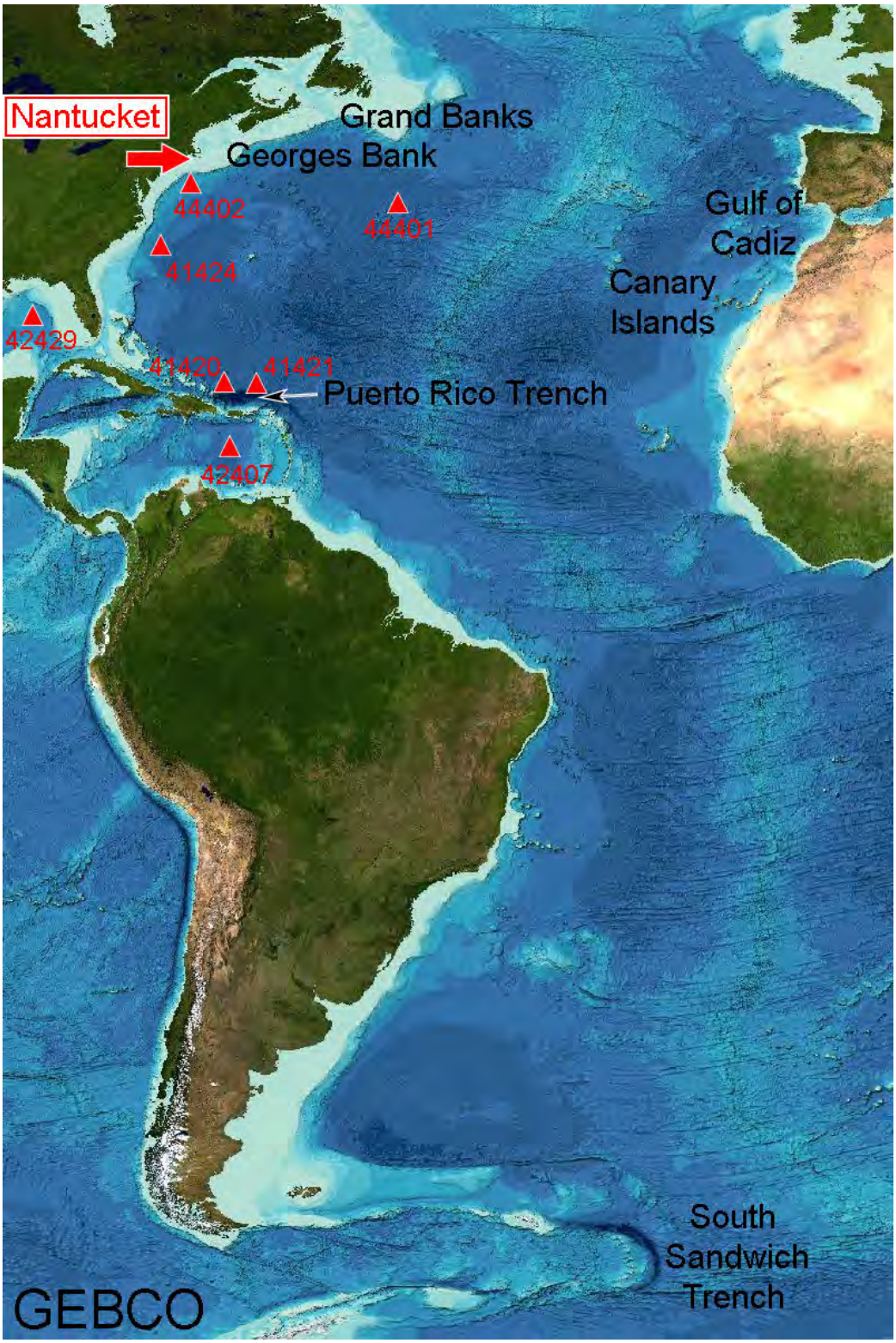

Figure 5: Nantucket's location in the northwest Atlantic. The underlying chart is based on the GEBCO dataset and is annotated with potential tsunami source areas. Red triangles mark the position of DART® tsunameters that would be assimilated during an event as input to the SIFT forecast system.

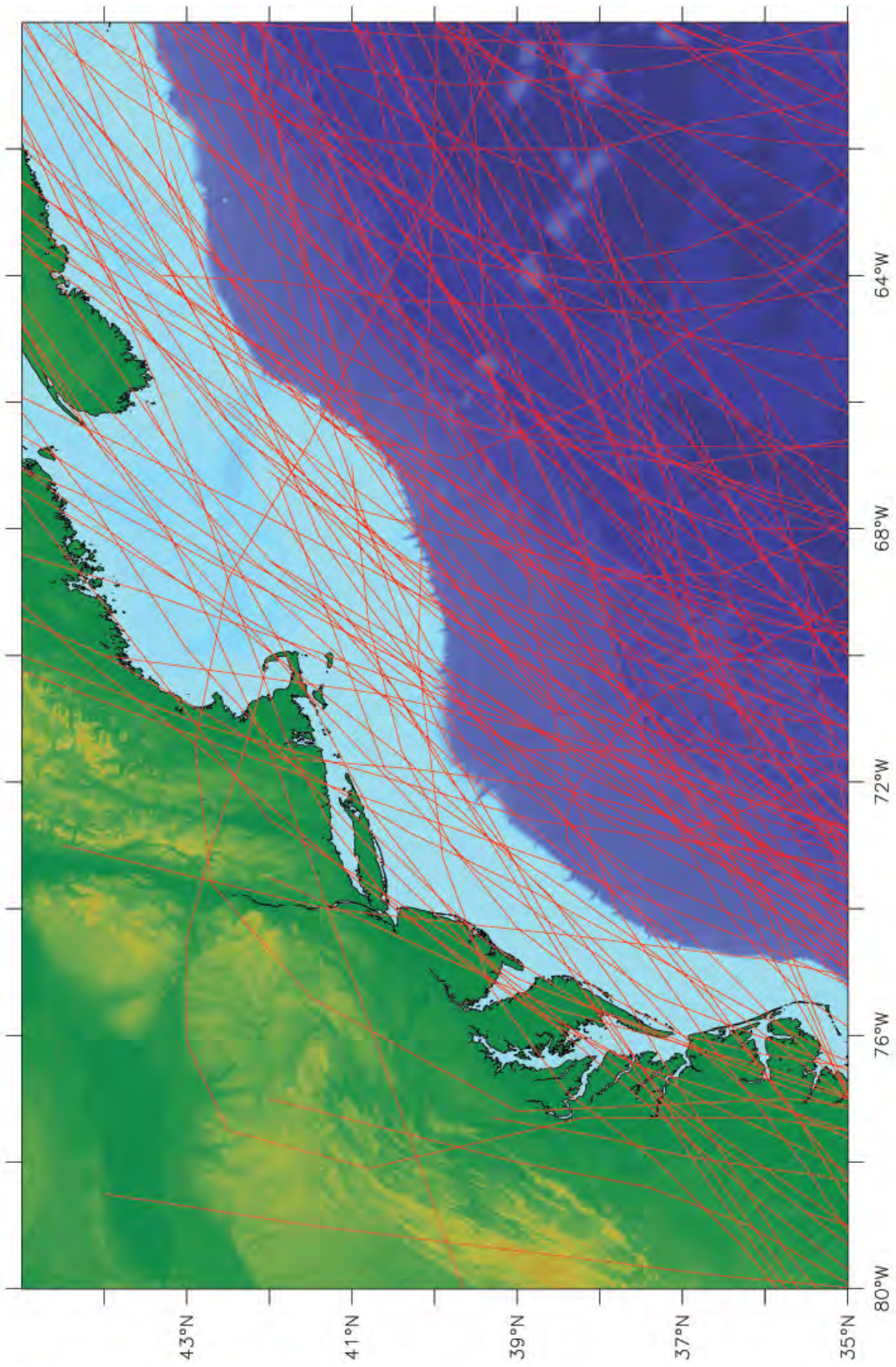

Figure 6: Hurricane and tropical storm tracks (1851–2012) that have passed near the northeastern seaboard of the U.S. (database maintained by the National Hurricane Center).

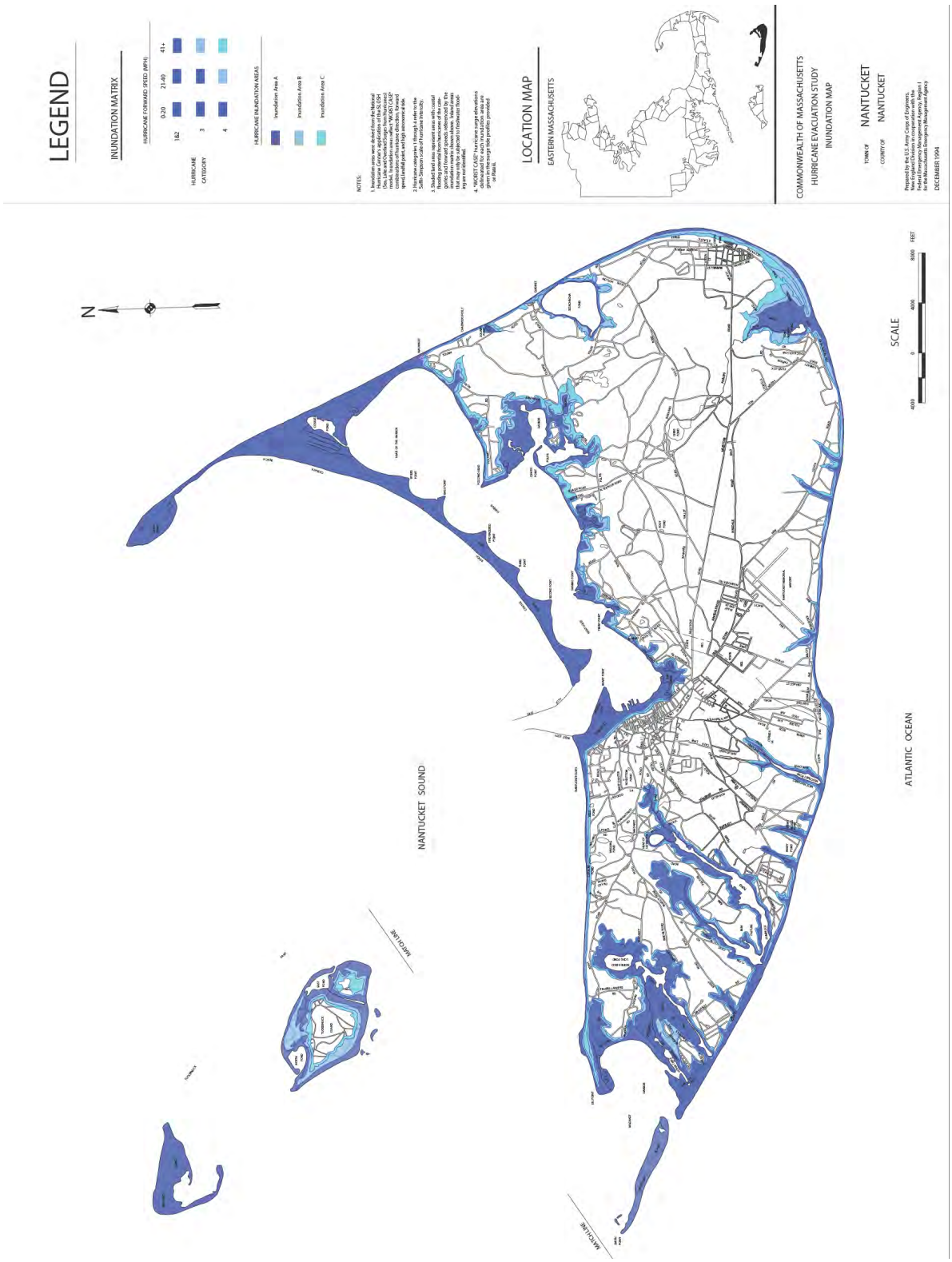

Figure 7: Areas of potential inundation for Nantucket, during passage nearby of hurricanes or tropical storms, computed by the USACE using the SLOSH model. The pattern of inundation has similarities to that seen in severe tsunami scenarios investigated during model testing.

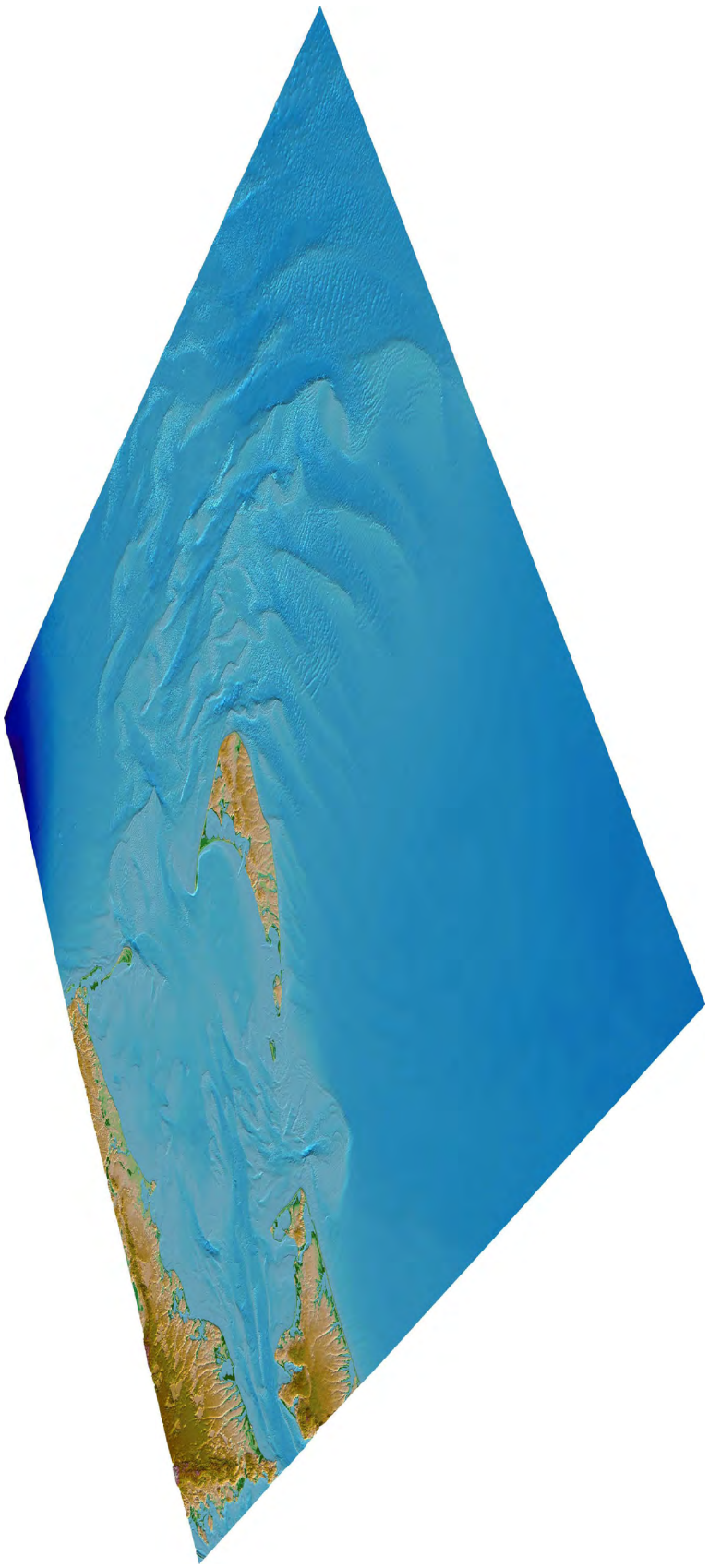

Figure 8: Digital elevation model for Nantucket, Massachusetts, provided by the National Geophysical Data Center. The extensive region of submerged sand waves to the south and east of Nantucket, named the Nantucket Shoals, have a major impact on tsunami dynamics.

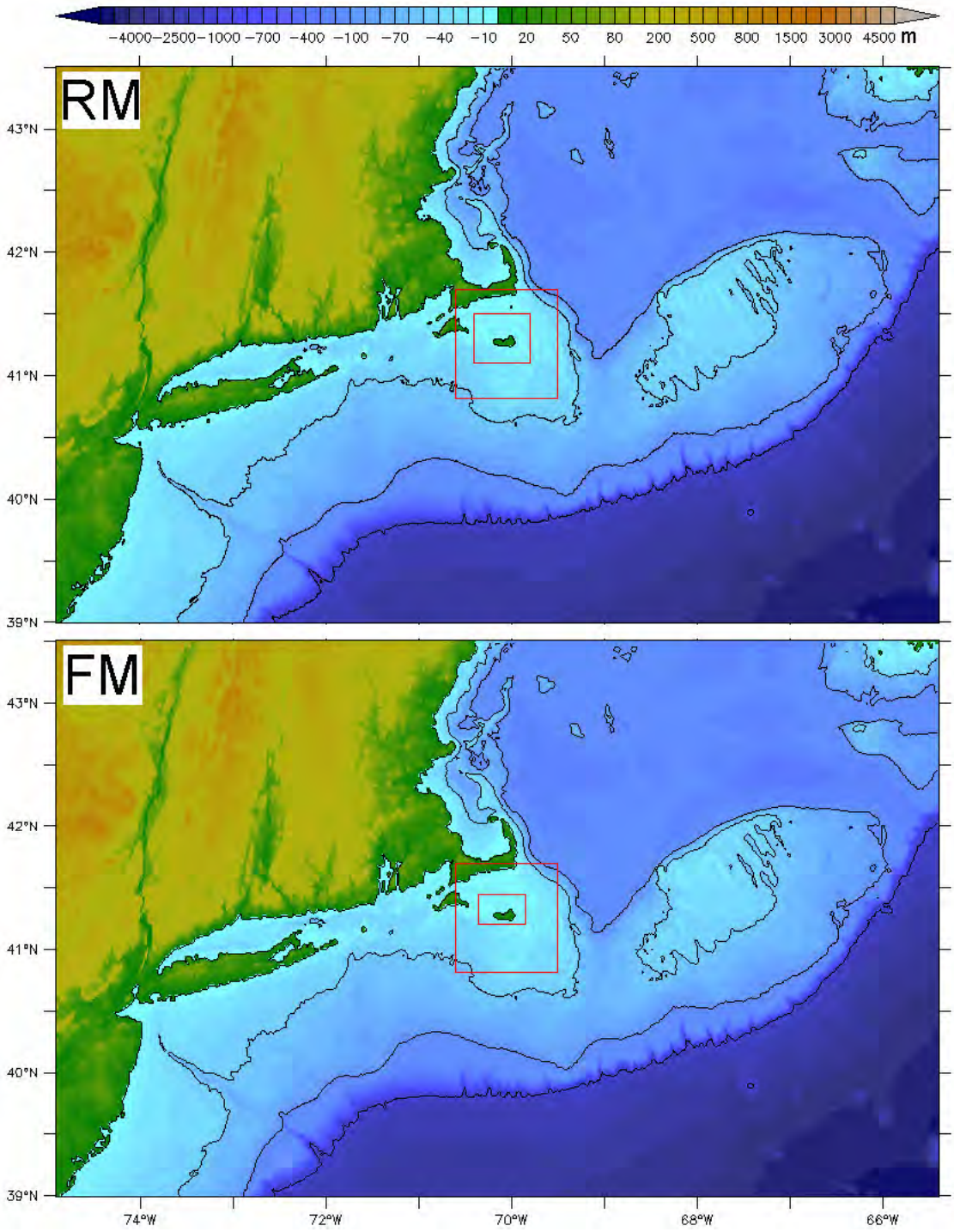

Figure 9: Comparison of the reference (RM, upper panel) and forecast (FM, lower panel) models for the outermost A grid. The subregions covered by the B grid and C grid for each case are delineated in red.

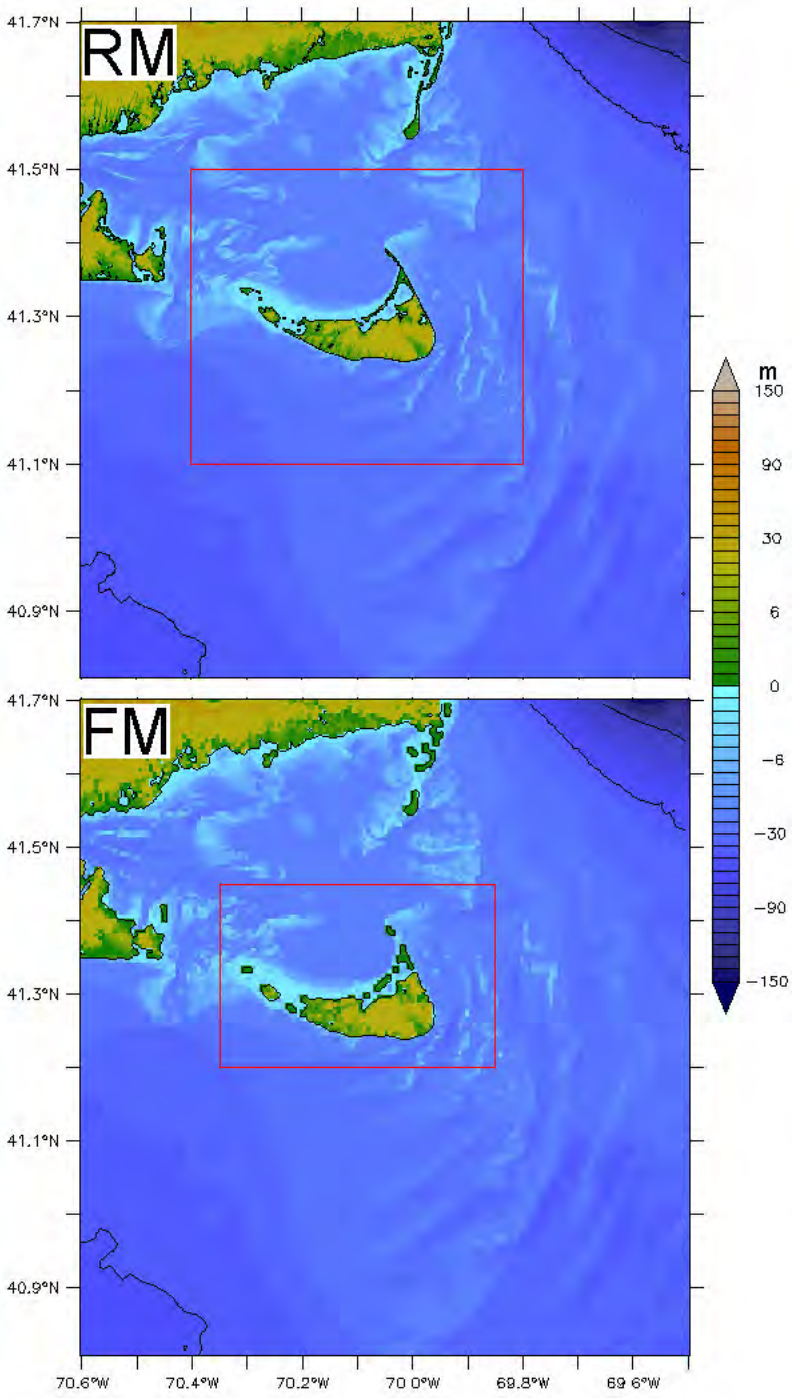

Figure 10: Comparison of the reference (RM, upper panel) and forecast (FM, lower panel) models for the intermediate B grid. The subregions covered by the C grid for each case are delineated in red.

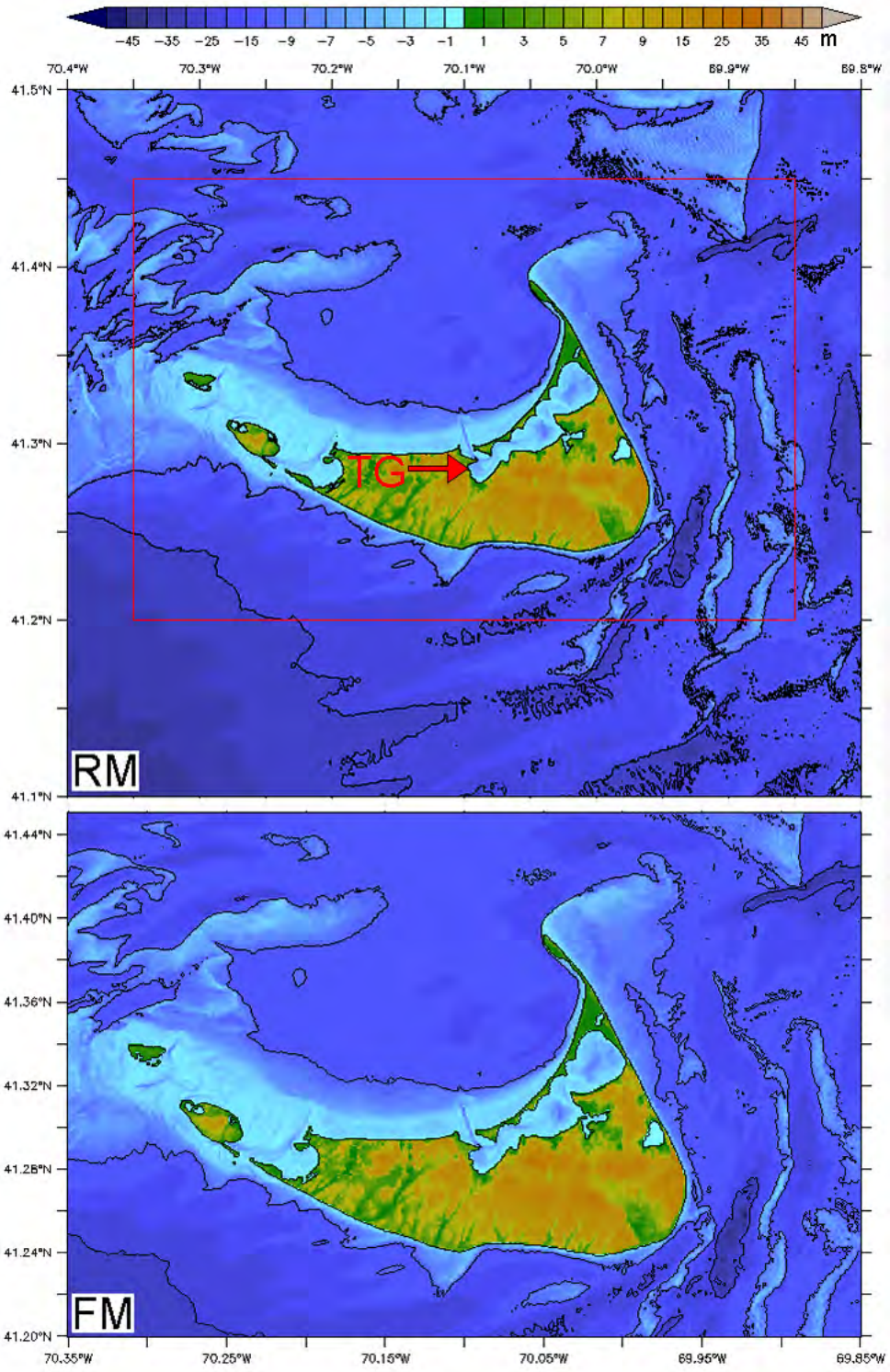

Figure 11: Comparison of the reference (RM, upper panel) and forecast (FM, lower panel) models for the innermost C grid. The smaller C grid domain of the forecast model is delineated in red in the upper panel. The location of the tide gauge (TG) is indicated.

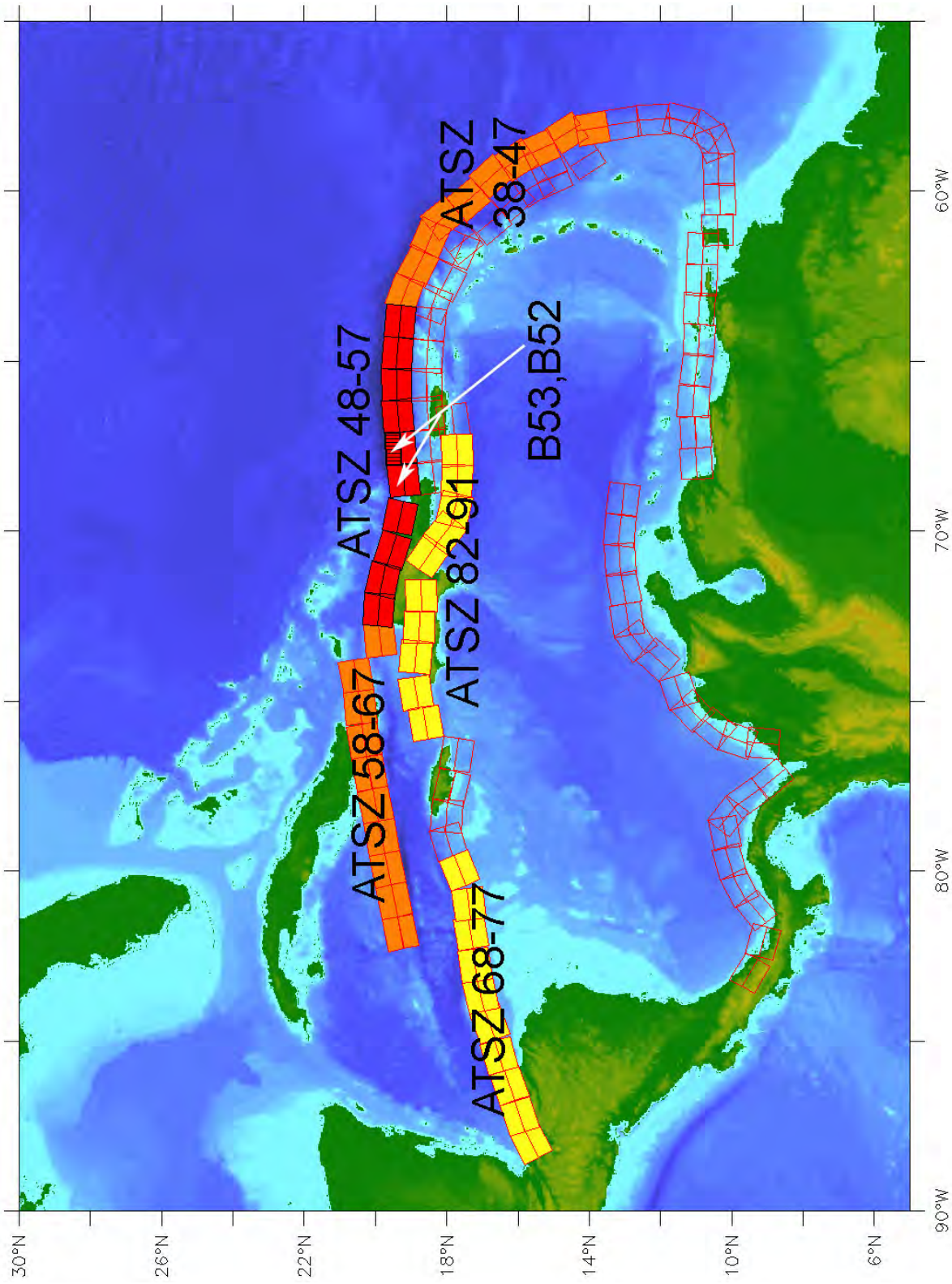

Figure 12: Equally weighted combinations of 20 unit sources with a slip of 25 m are used as mega-tsunami scenarios. ATSZ 48-57 (red) is the most threatening to Nantucket; ATSZ 82-91, ATSZ 38-47, and ATSZ 58-67 are less threatening by a factor of two; and ATSZ 68-77 the least threatening. Unit source B52 is a standard test case while B53, scaled up by a factor of 2.81, represents the 1946 historical event north of the Dominican Republic.

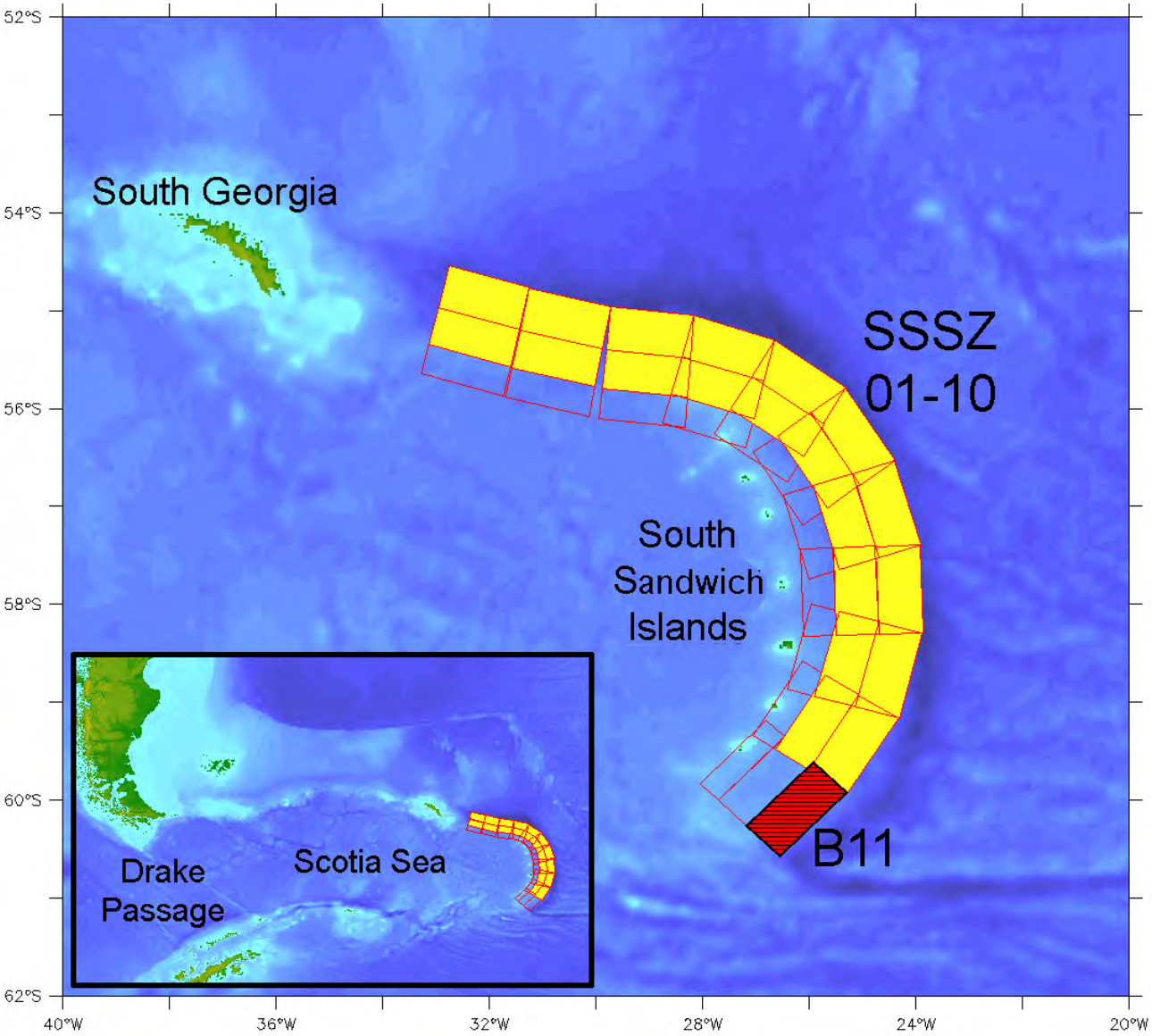

Figure 13: Unit sources, shaded yellow, from the South Sandwich region of the South Atlantic are combined in a mega-tsunami scenario SSSZ 01-10. The single source B11 (shaded red), scaled down by a factor of 0.01, is employed as a "micro" source.

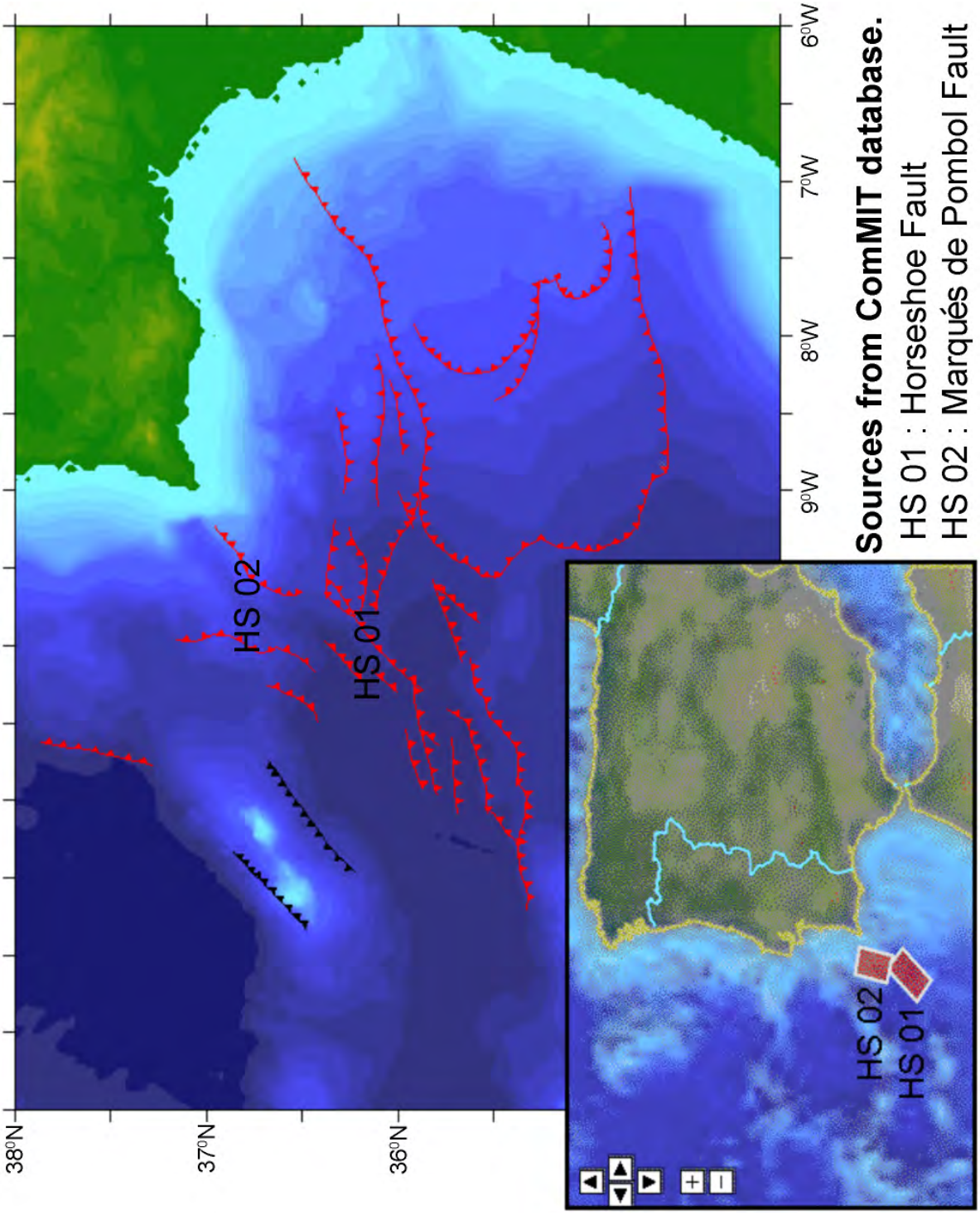

Figure 14: An ad hoc mega-tsunami scenario for the eastern Atlantic is based on two non-unit sources, HS 01–02. The source files were combined using the ComMIT tool, for a magnitude Mw 9.3 with uniformly distributed slip.

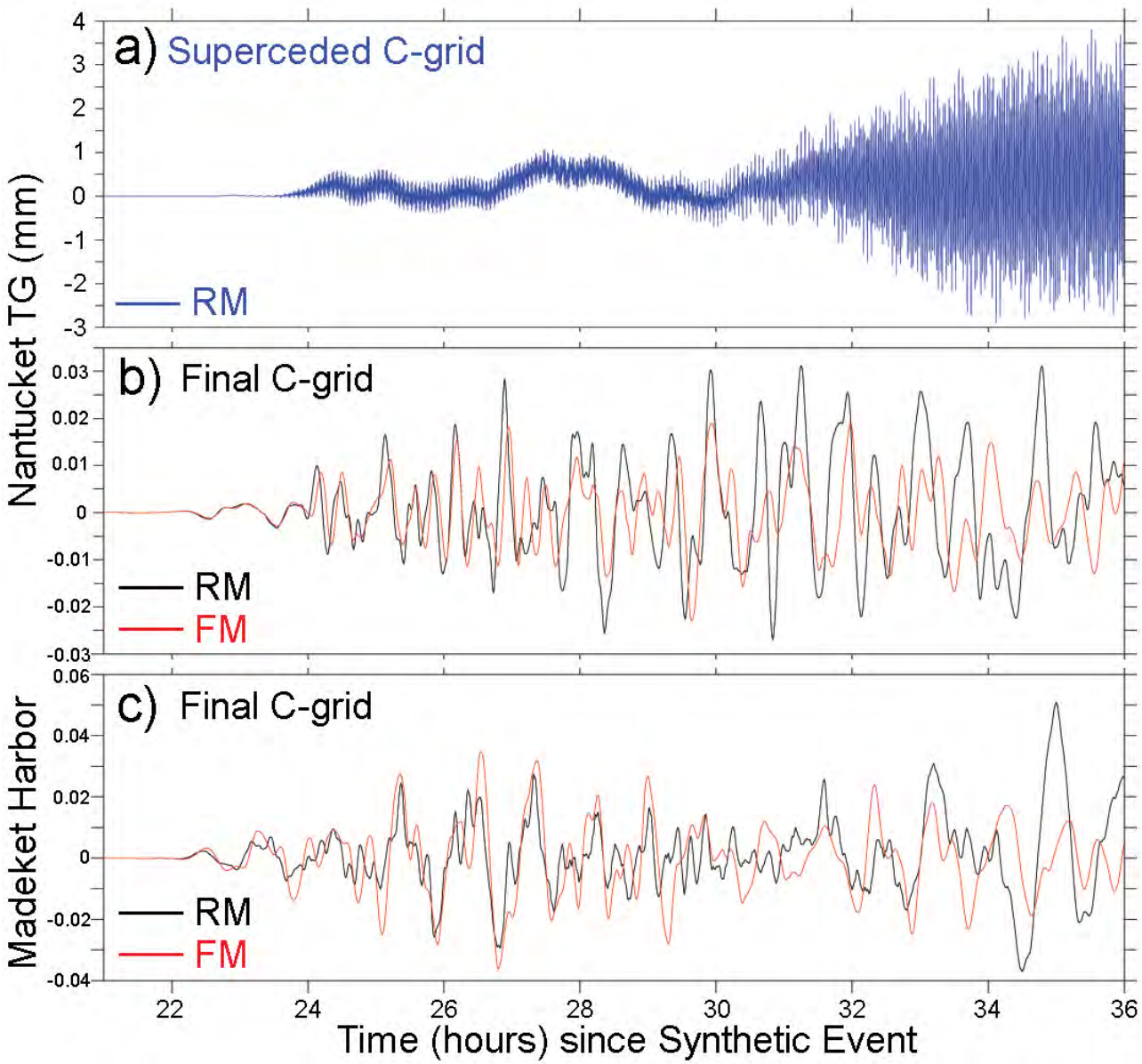

Figure 15: Stages in grid refinement using the "micro"-event scenario SSSZ B11: (a) small-scale instability associated with poorly resolved features in a superceded reference model C grid; (b) consistent warning point time series from the reference (RM, black) and forecast (FM, red) model solutions; (c) similarly consistent comparison to that in the previous panel, but for a site representative of Madaket Harbor.

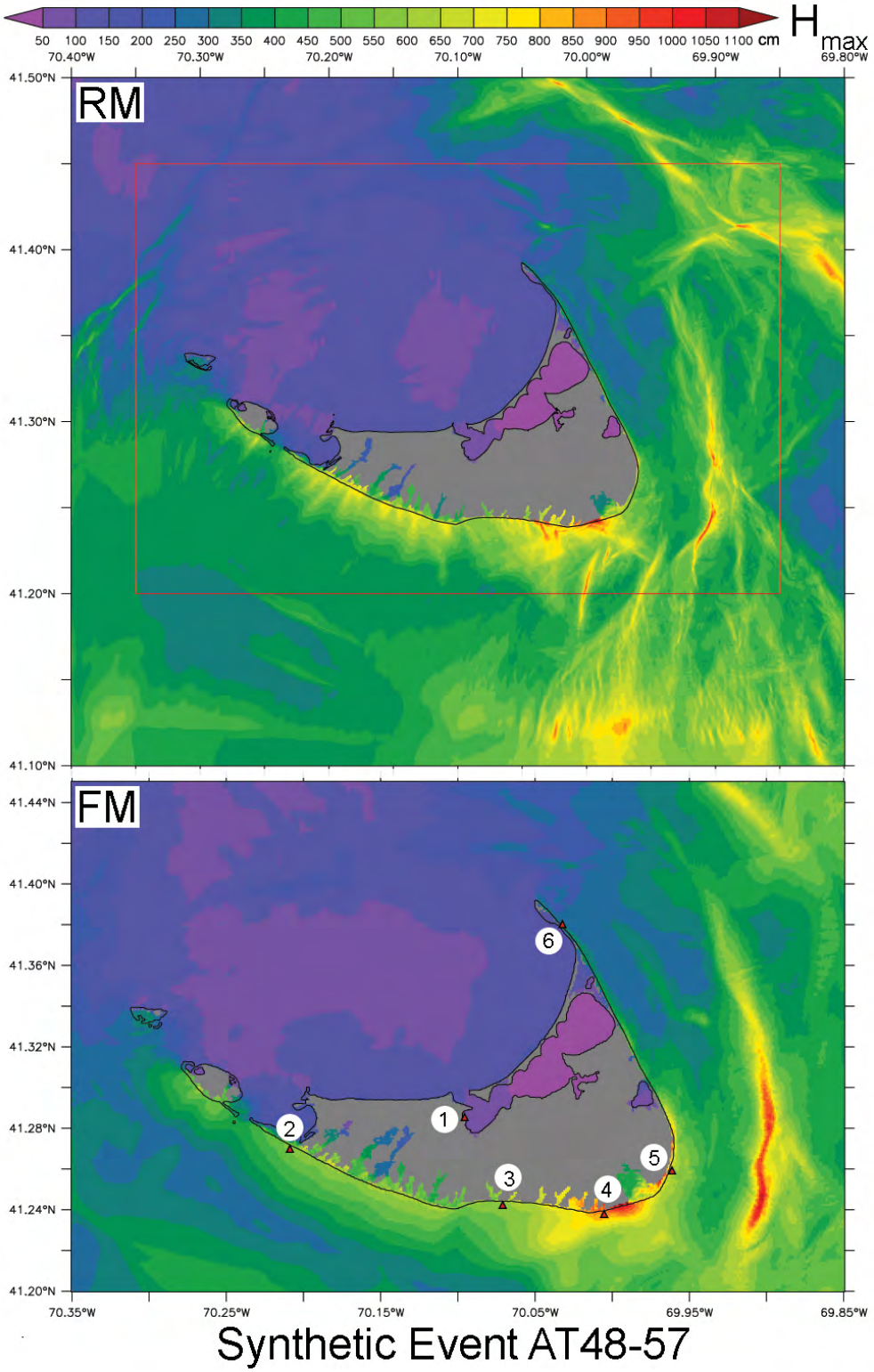

Figure 16: Comparison of the reference (RM, upper panel) and forecast (FM, lower panel) model maximum wave height (cm) of the innermost C grid for the ATSZ 48–57 mega-tsunami scenario. Time series comparison sites are marked by triangles in the lower panel: 1—Nantucket, 2—Madaket Beach, 3—Airport Runway, 4—Tom Nevers Beach, 5—Siasconset, and 6—Great Point Spit.

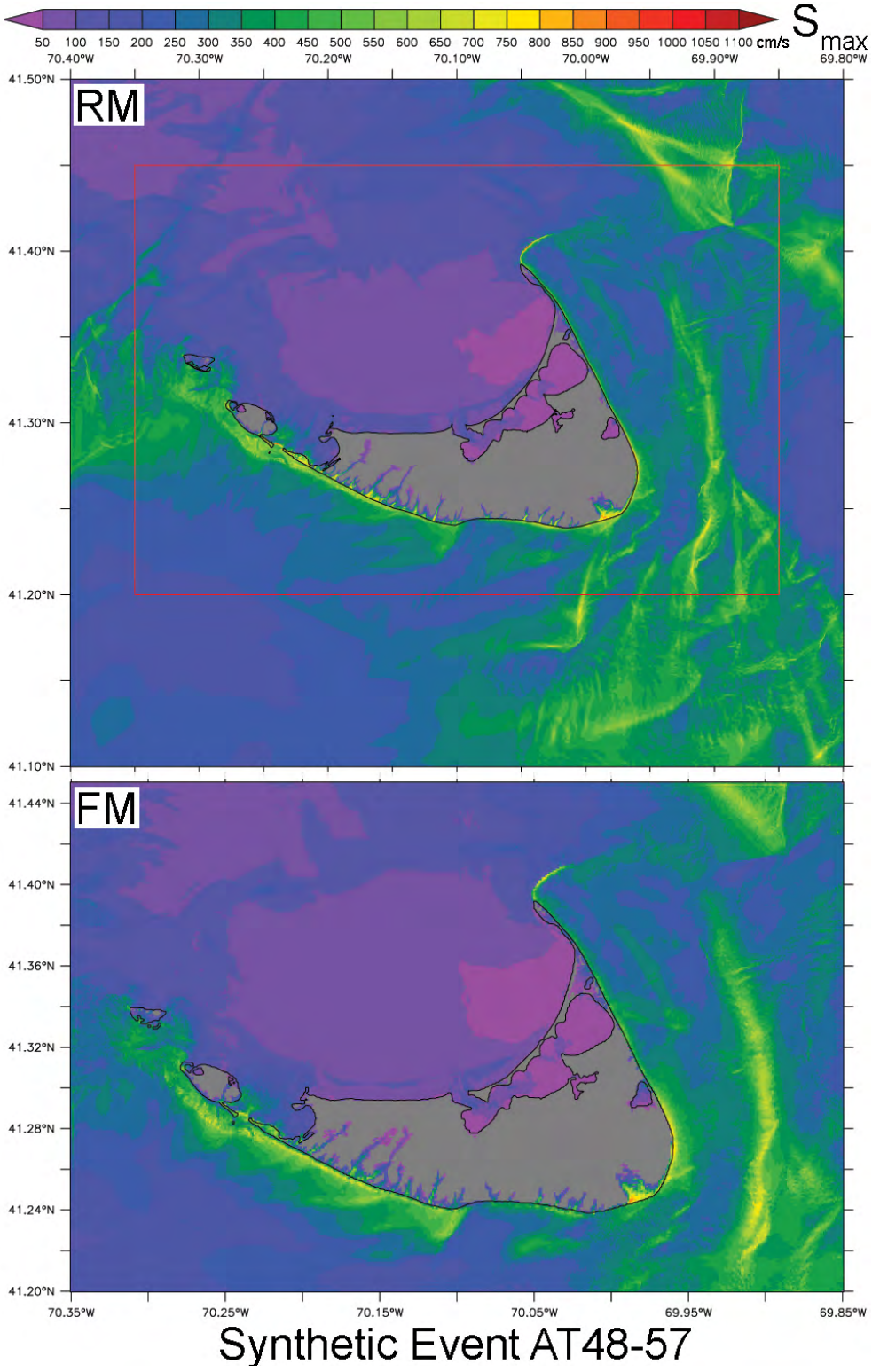

Figure 17: Comparison of the reference (RM, upper panel) and forecast (FM, lower panel) model maximum speed (cm/s) of the innermost C grid for the ATSZ 48–57 mega-tsunami scenario. Both panels share a common color scale.

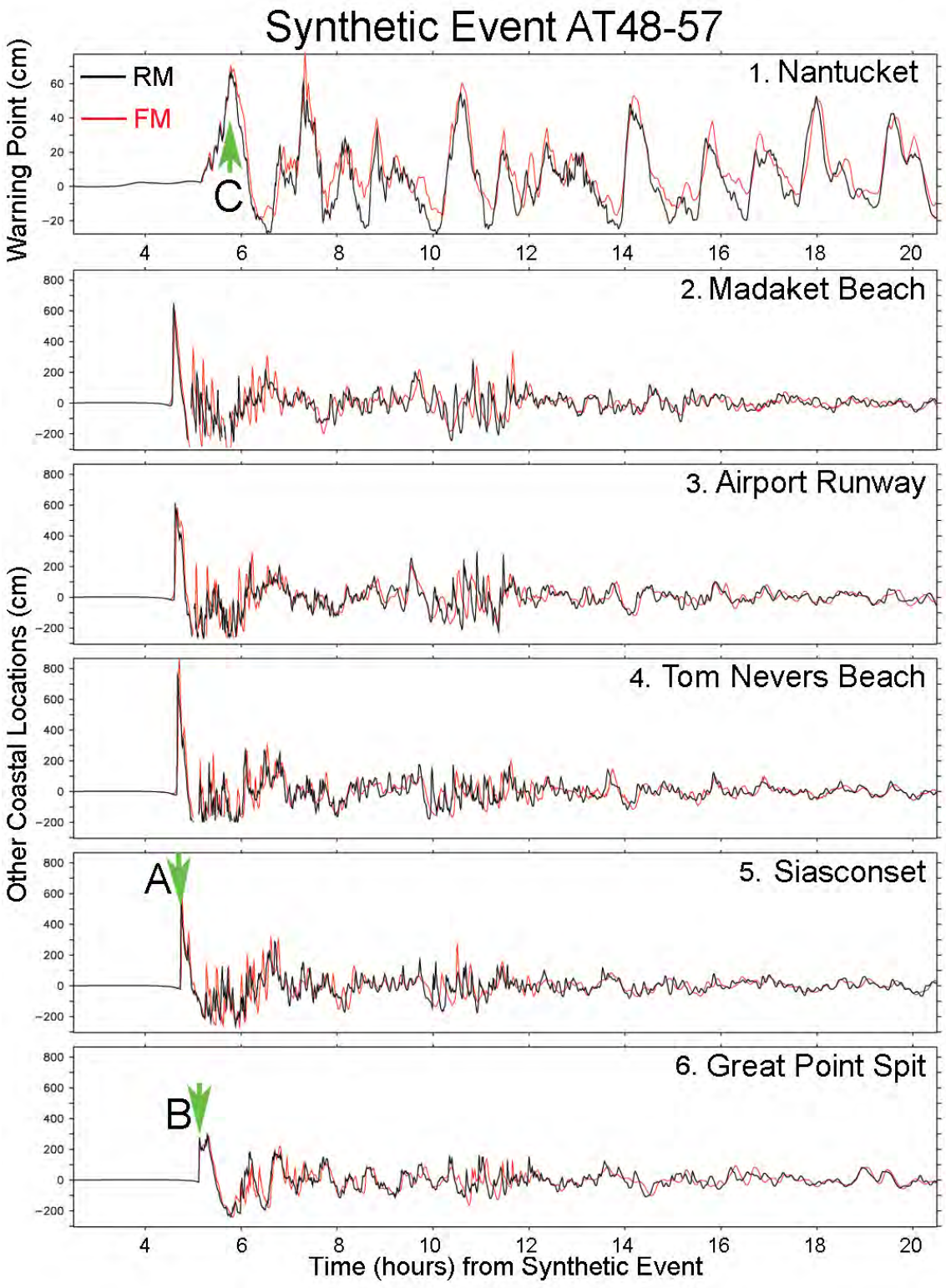

Figure 18: Comparison of reference (RM, black) and forecast (FM, red) model wave height time series at the warning point (upper panel) and five other coastal sites during the ATSZ 48–57 mega-tsunami scenario. Green arrows indicate discrete times (A, B, C) at which the reference and forecast model wave height and vector current fields are compared in **Figures 19–21**.

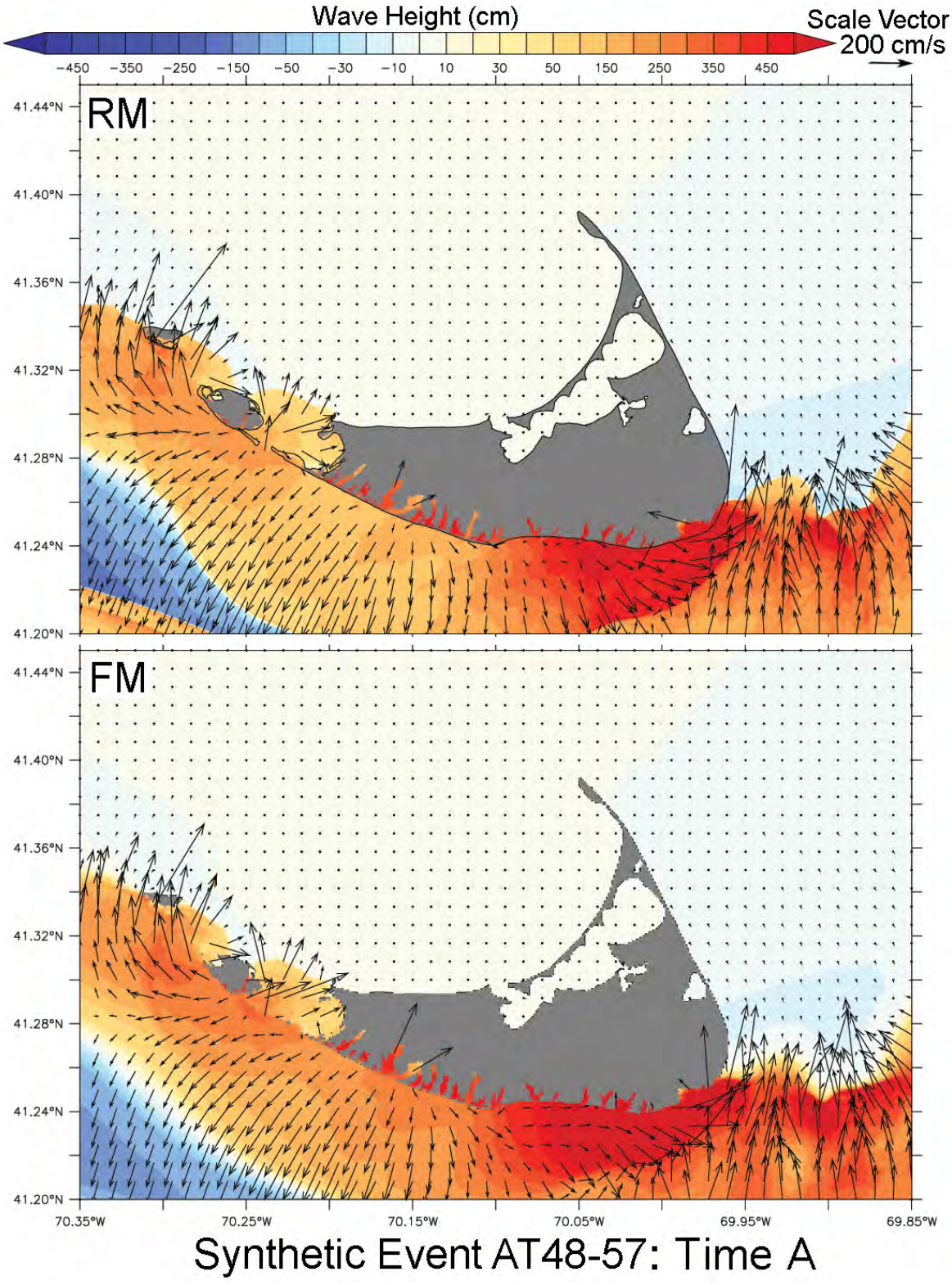

Figure 19: Comparison of the reference (RM, upper panel) and forecast (FM, lower panel) model wave height (cm) and vector current speed (cm/s) of the innermost C grid for the ATSZ 48–57 mega-tsunami scenario. Both panels share a common color bar and a common scale vector (200 cm/s) is displayed in the upper right corner. Time A: the leading wave crest reaches Siasconset.

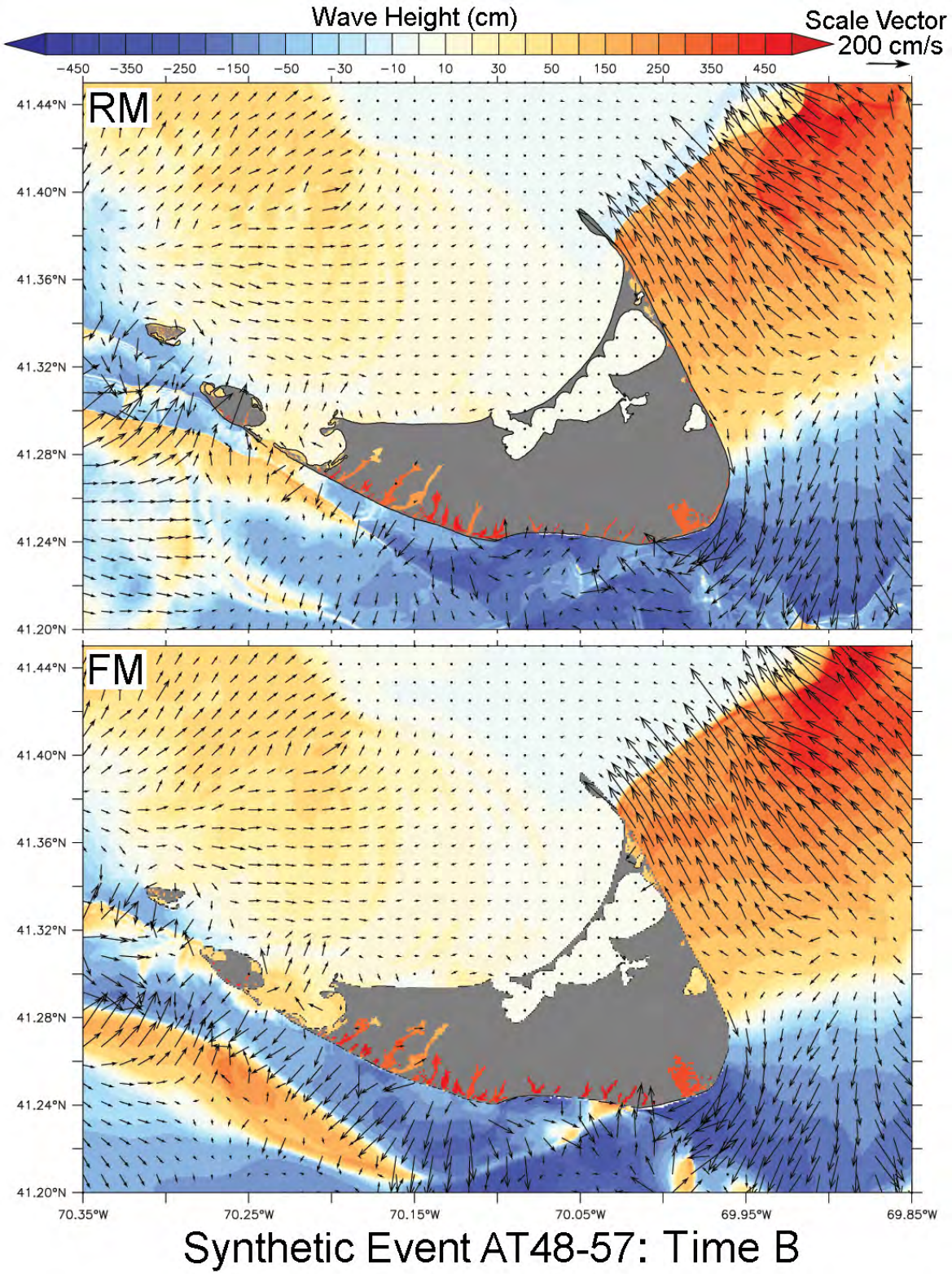

Figure 20: Comparison of the reference (RM, upper panel) and forecast (FM, lower panel) model wave height (cm) and vector current speed (cm/s) of the innermost C grid for the ATSZ 48–57 mega-tsunami scenario. Time B: the leading wave crest reaches Great Point Spit.

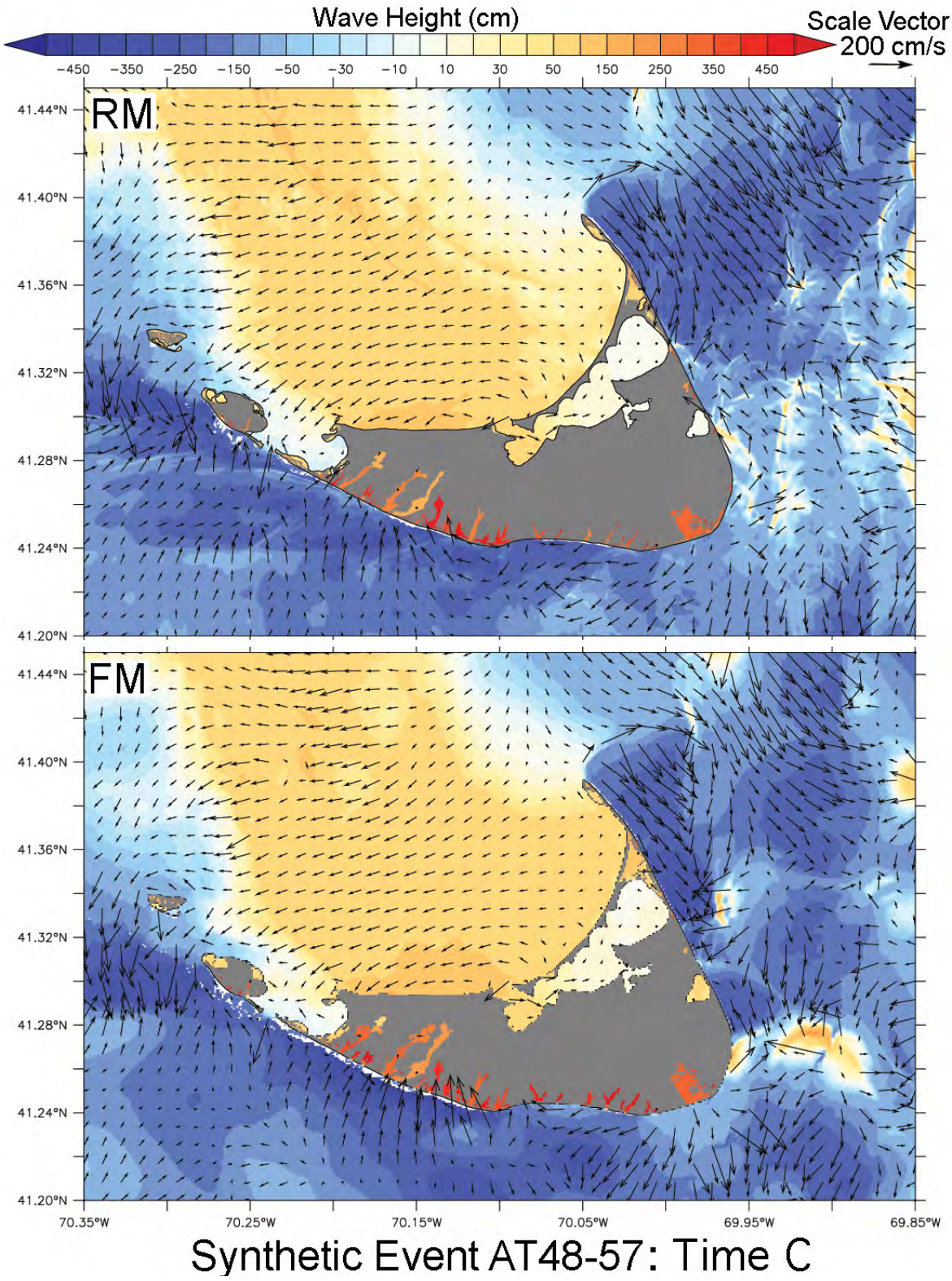

Figure 21: Comparison of the reference (RM, upper panel) and forecast (FM, lower panel) model wave height (cm) and vector current speed (cm/s) of the innermost C grid for the ATSZ 48–57 mega-tsunami scenario. Time C: the leading wave crest reaches Nantucket Harbor.

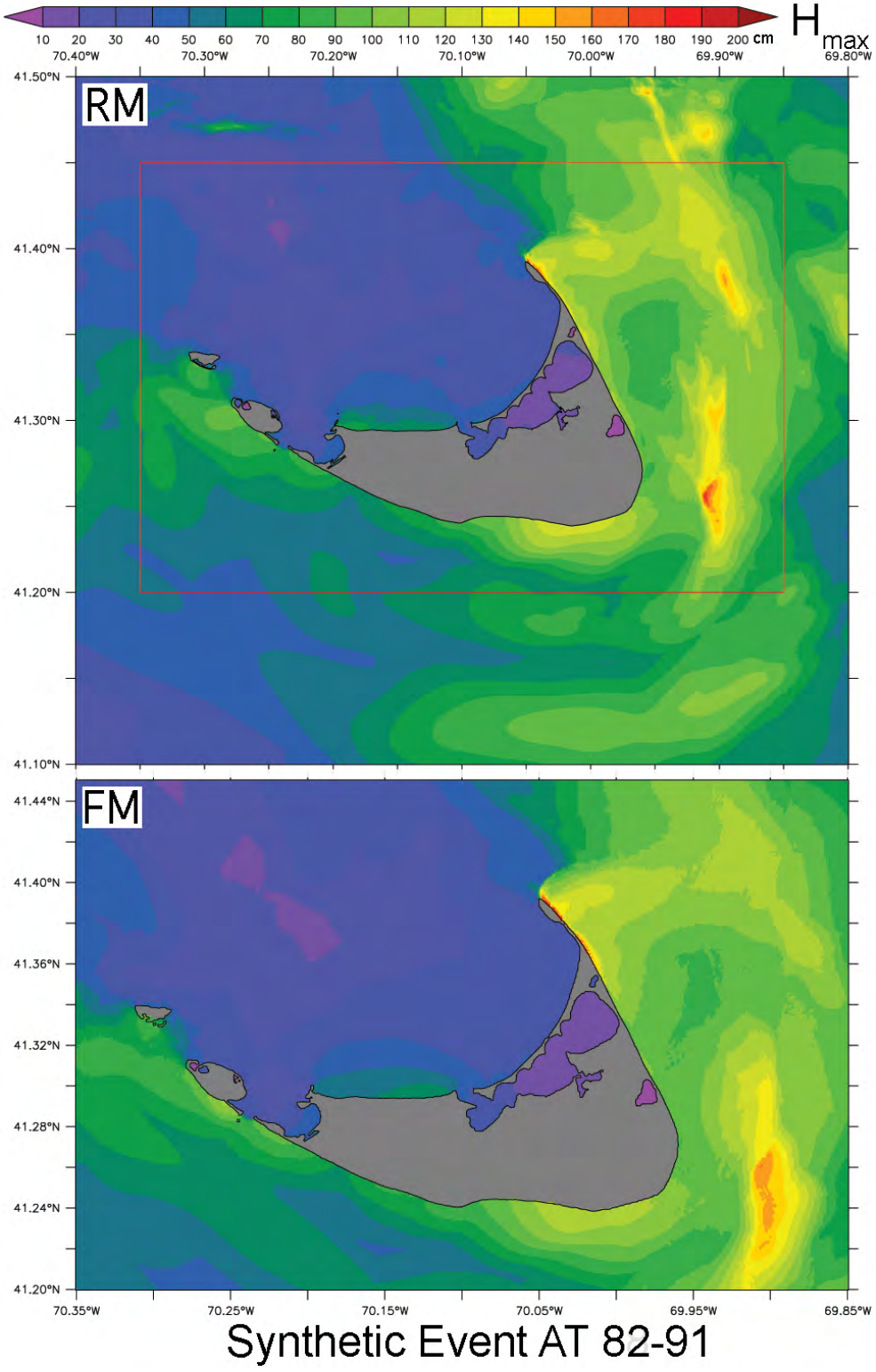

Figure 22: Comparison of the reference (RM, upper panel) and forecast (FM, lower panel) model maximum wave height (cm) of the innermost C grid for the ATSZ 82–91 mega-tsunami scenario.

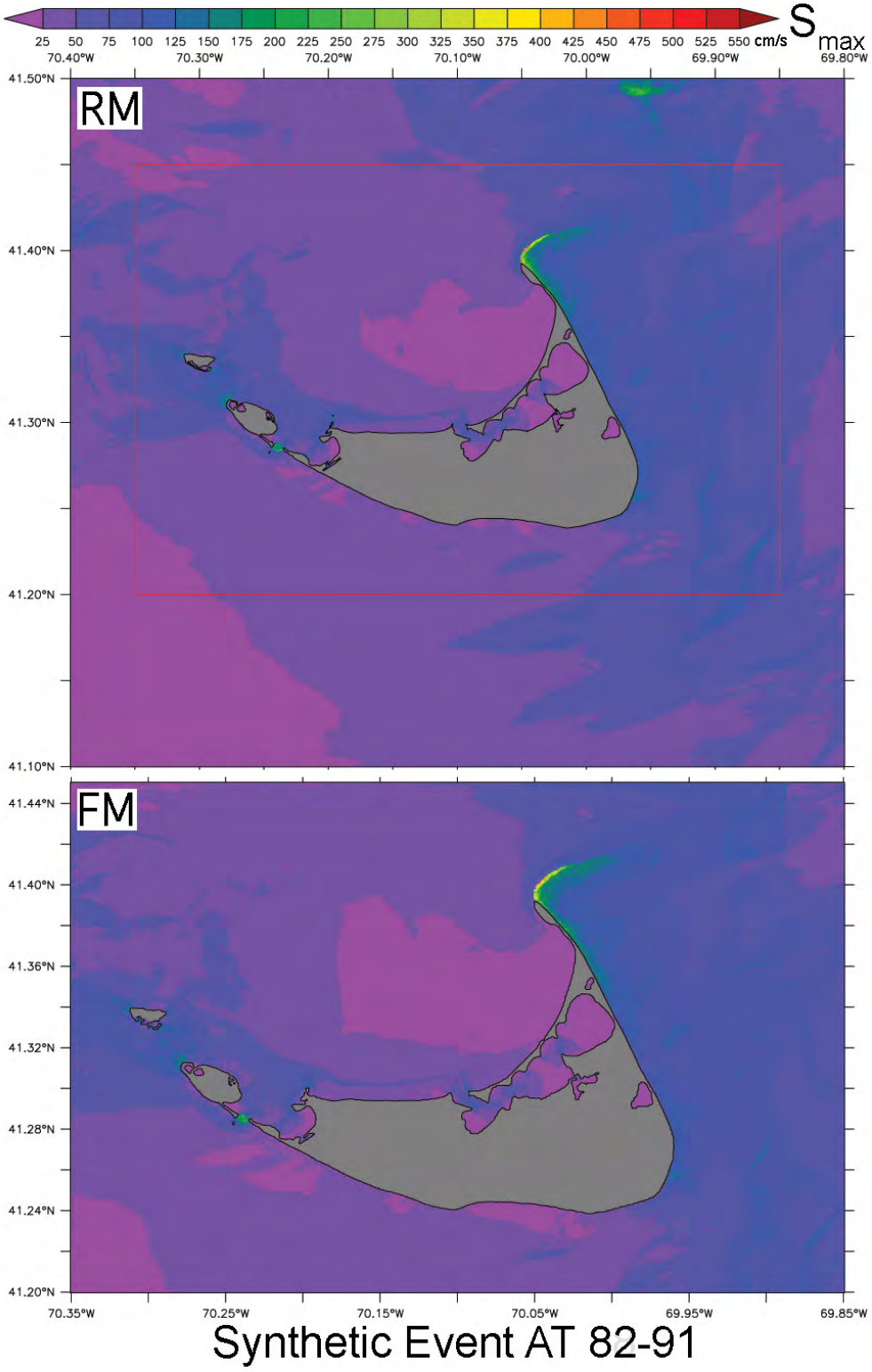

Figure 23: Comparison of the reference (RM, upper panel) and forecast (FM, lower panel) model maximum speed (cm/s) of the innermost C grid for the ATSZ 82–91 mega-tsunami scenario.

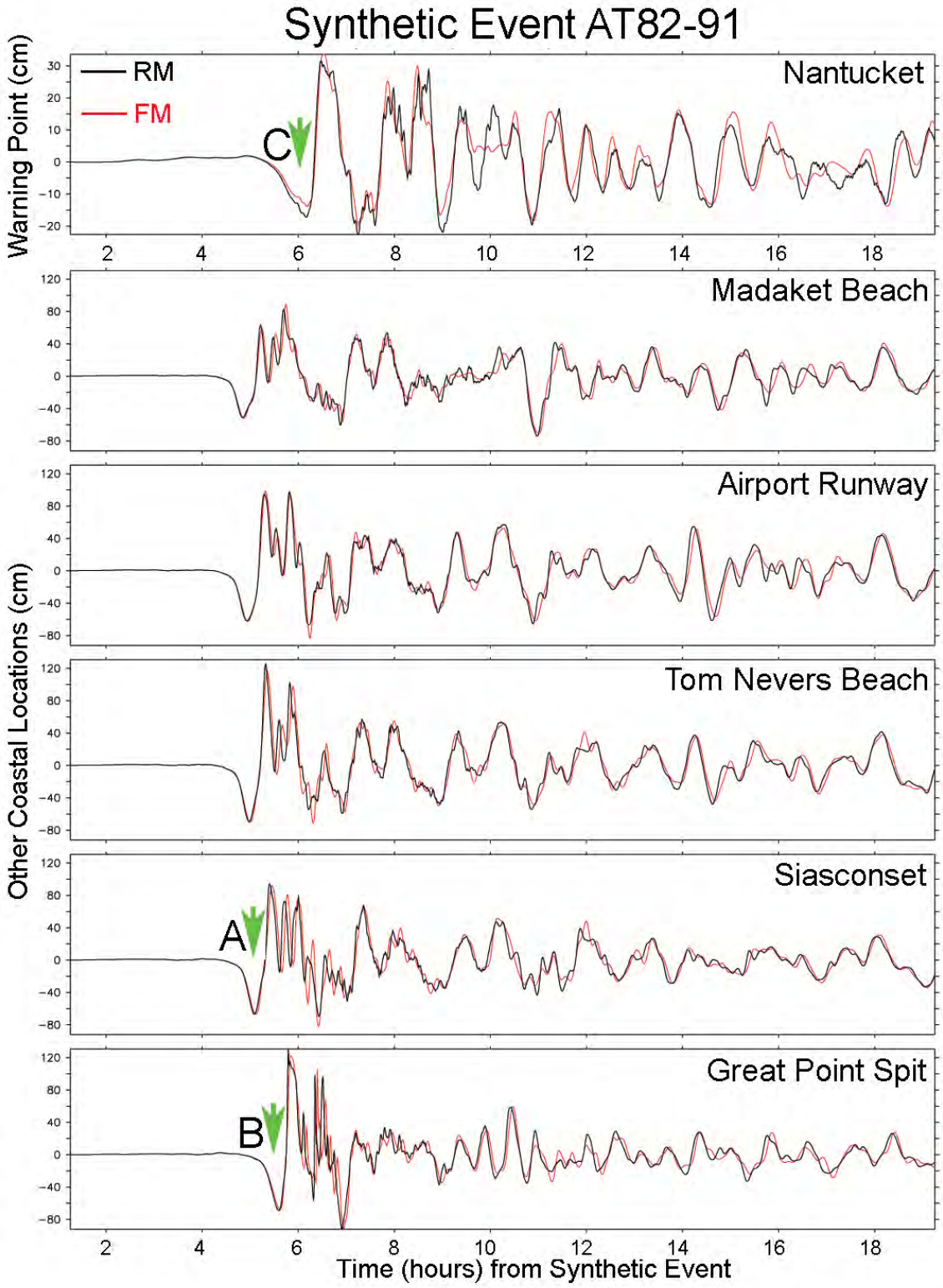

Figure 24: Comparison of the reference (RM, black) and forecast (FM, red) model wave height time series at the warning point (upper panel) and five other coastal sites during the ATSZ 82–91 mega-tsunami scenario. Green arrows indicate discrete times (A, B, C) at which the reference and forecast wave height and vector current fields are compared in **Figures 25–27**.

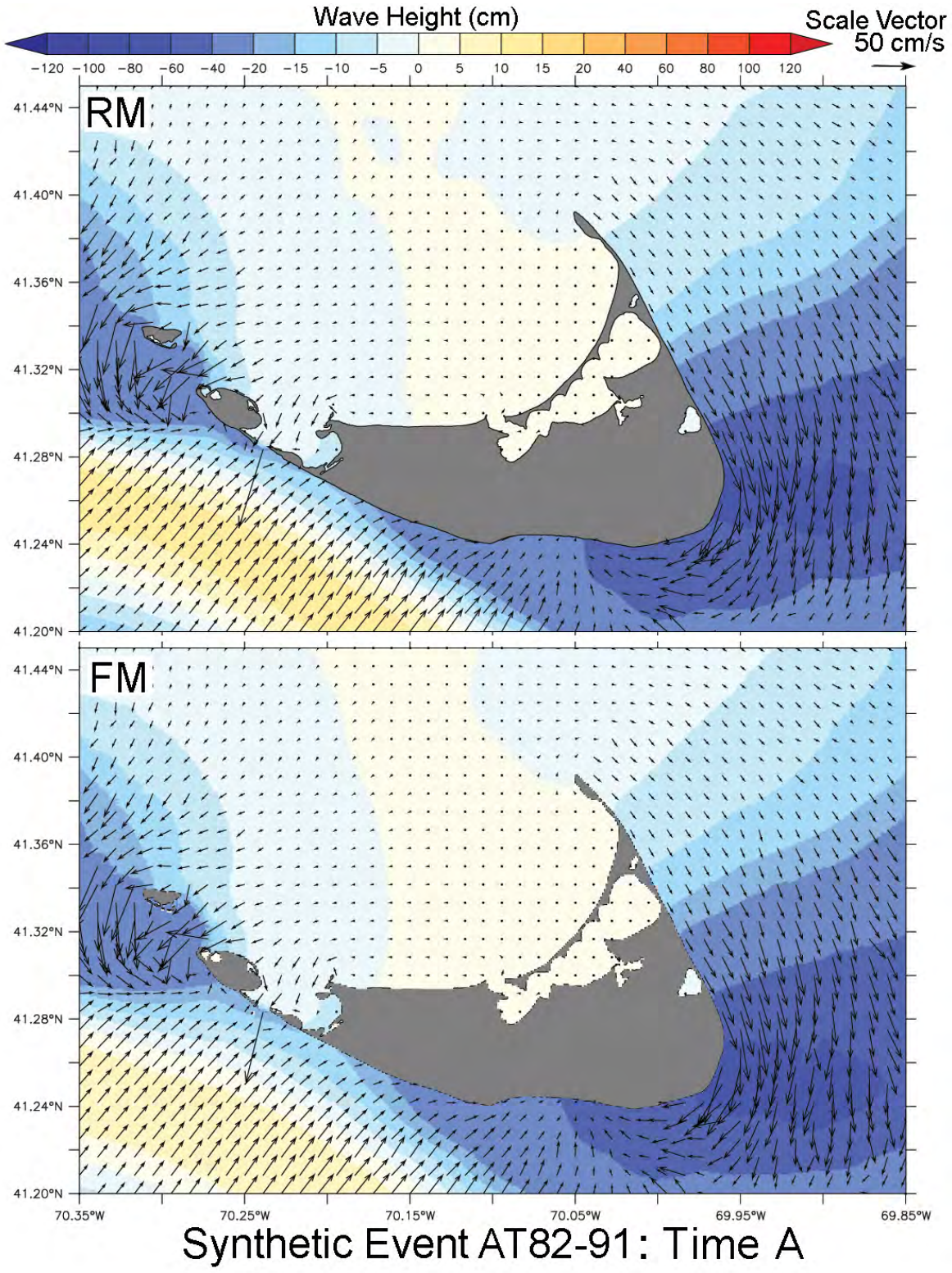

Figure 25: Comparison of the reference (RM, upper panel) and forecast (FM, lower panel) model wave height (cm) and vector current speed (cm/s) of the innermost C grid for the ATSZ 82–91 mega-tsunami scenario. Time A: the leading wave trough reaches Siasconset.

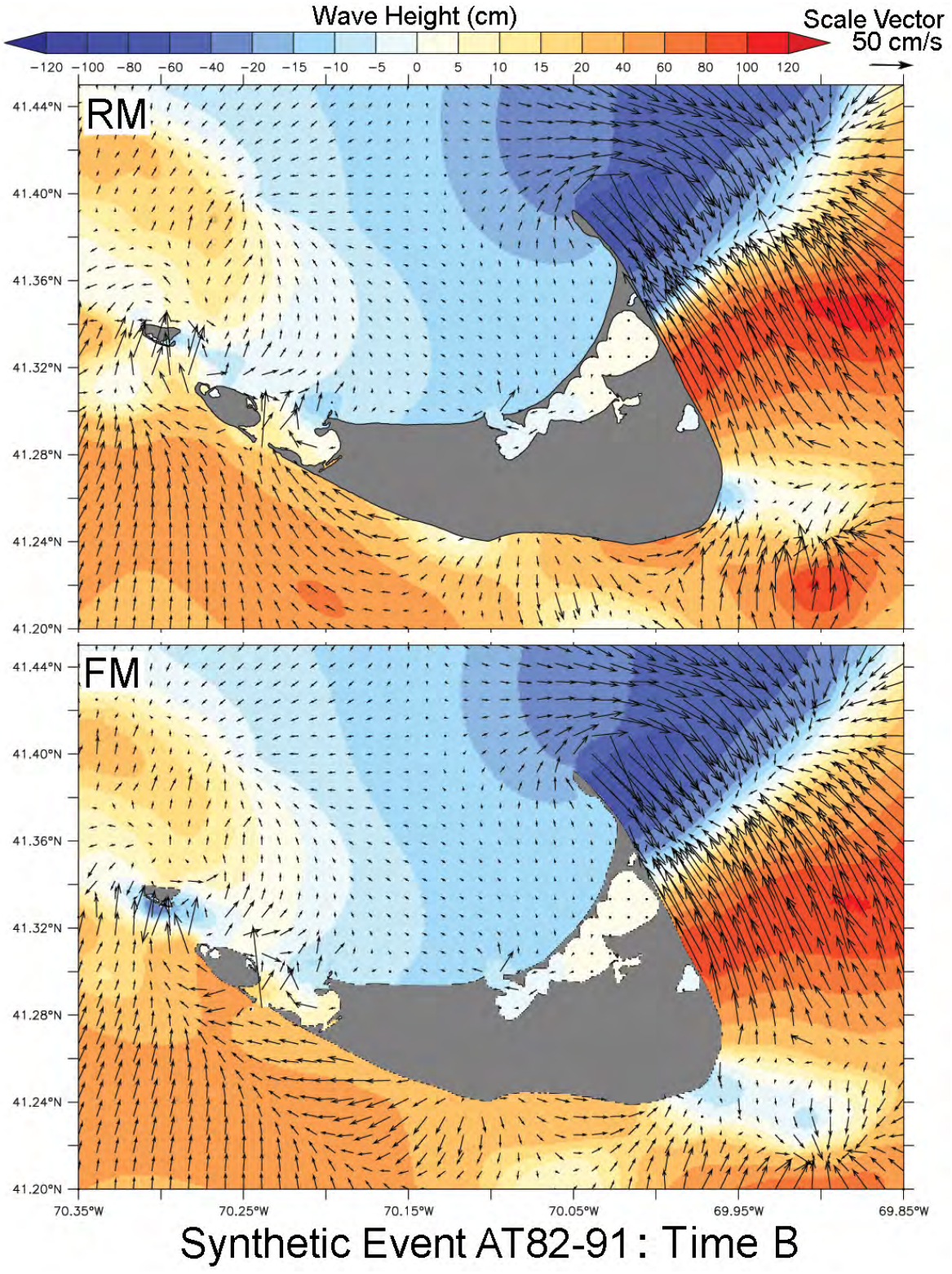

Figure 26: Comparison of the reference (RM, upper panel) and forecast (FM, lower panel) model wave height (cm) and vector current speed (cm/s) of the innermost C grid for the ATSZ 82–91 mega-tsunami scenario. Time B: the leading wave trough reaches Great Point Spit.

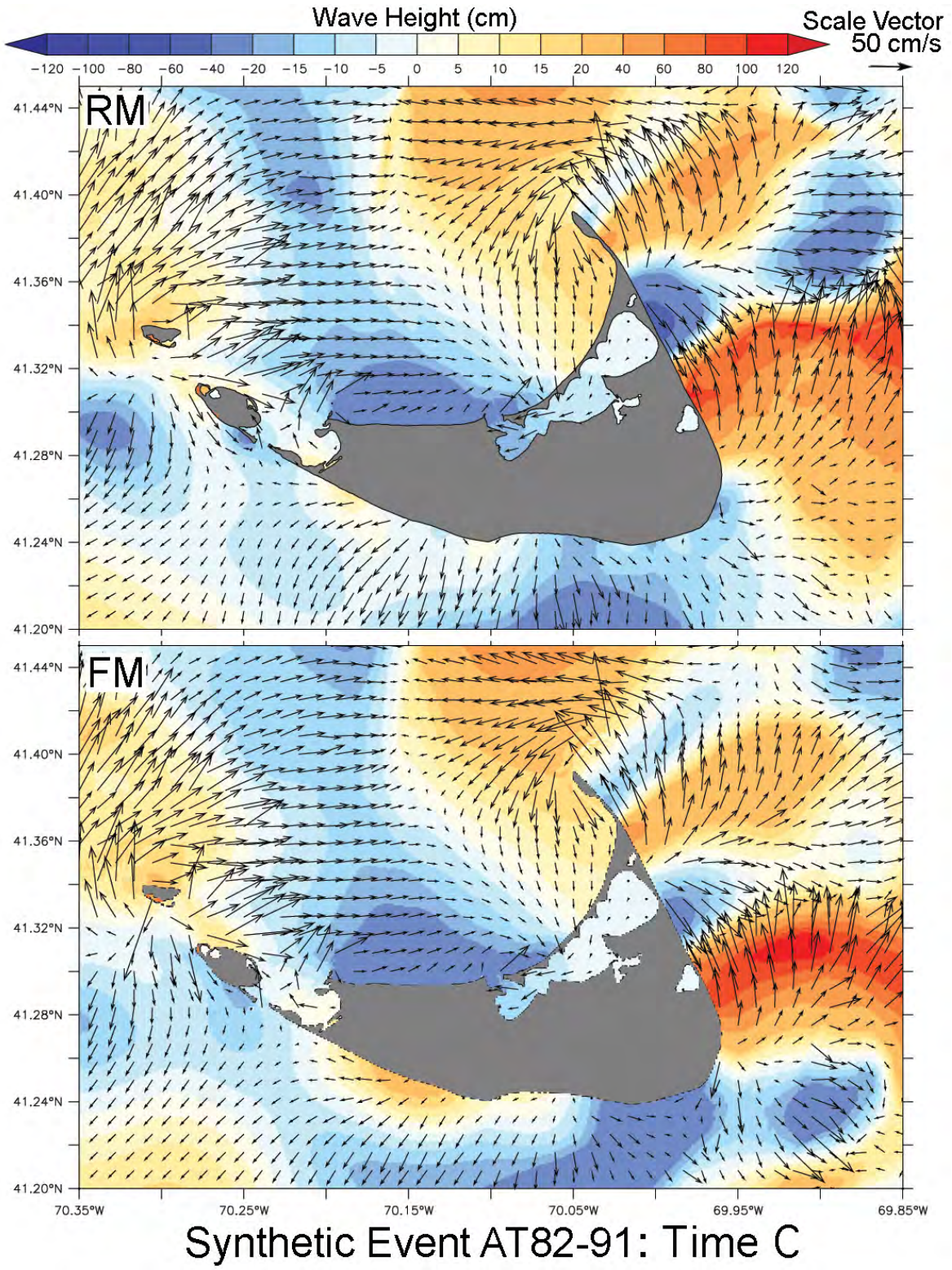

Figure 27: Comparison of the reference (RM, upper panel) and forecast (FM, lower panel) model wave height (cm) and vector current speed (cm/s) of the innermost C grid for the ATSZ 82–91 mega-tsunami scenario. Time C: the leading wave trough reaches Nantucket Harbor.

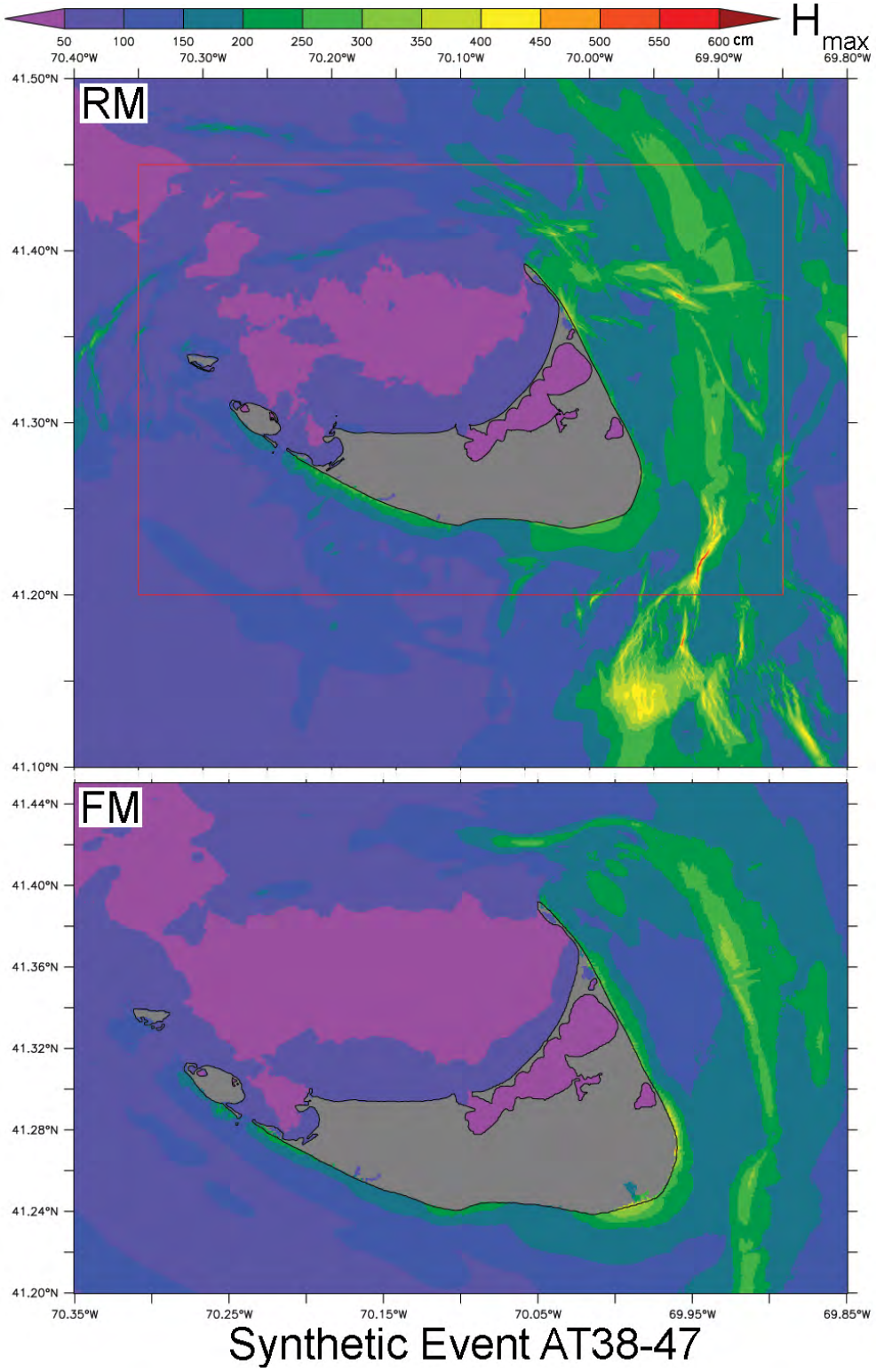

Figure 28: Comparison of the reference (RM, upper panel) and forecast (FM, lower panel) model maximum wave height (cm) of the innermost C grid for the ATSZ 38–47 mega-tsunami scenario.

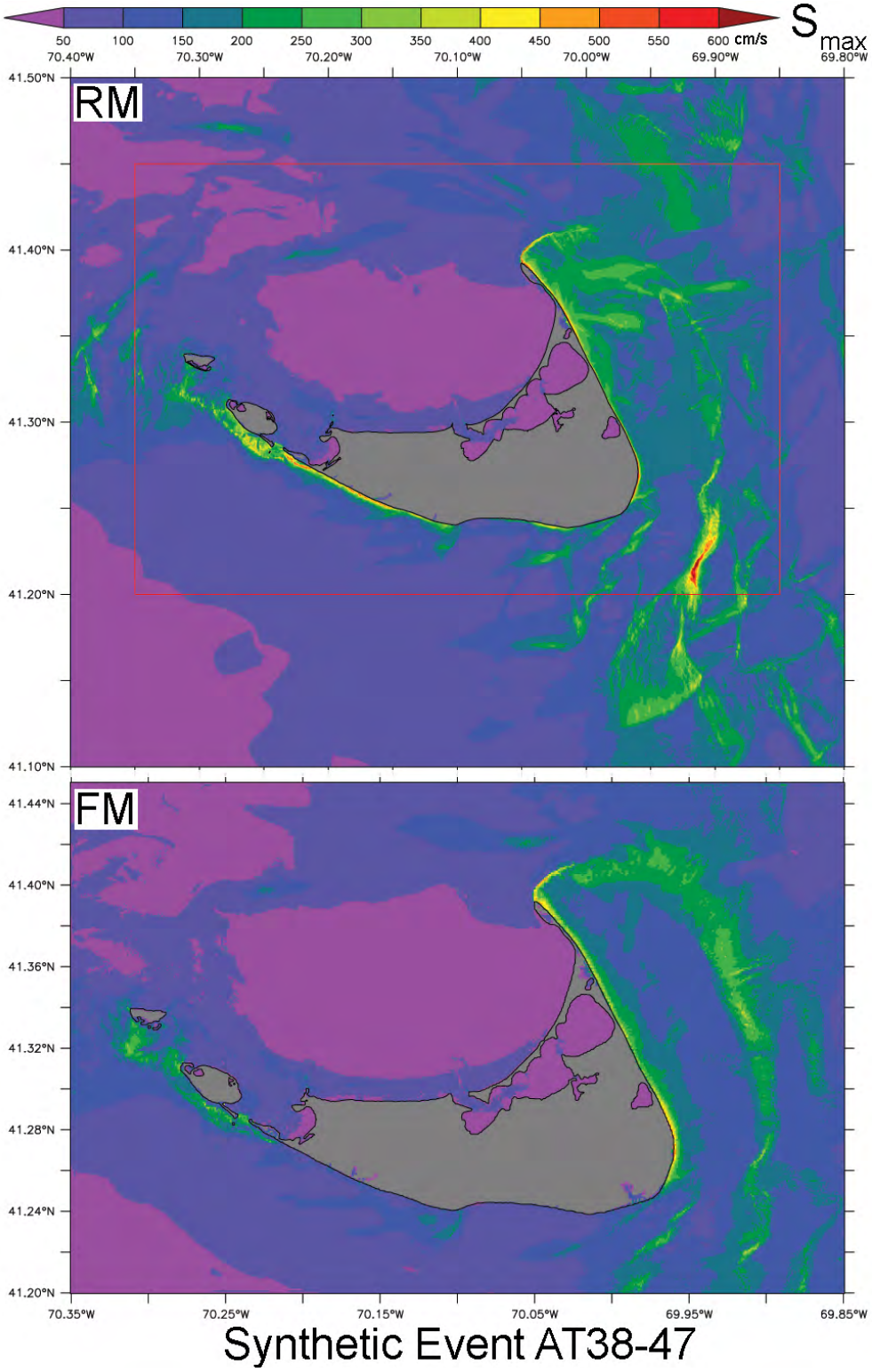

Figure 29: Comparison of the reference (RM, upper panel) and forecast (FM, lower panel) model maximum speed (cm/s) of the innermost C grid for the ATSZ 38–47 mega-tsunami scenario.

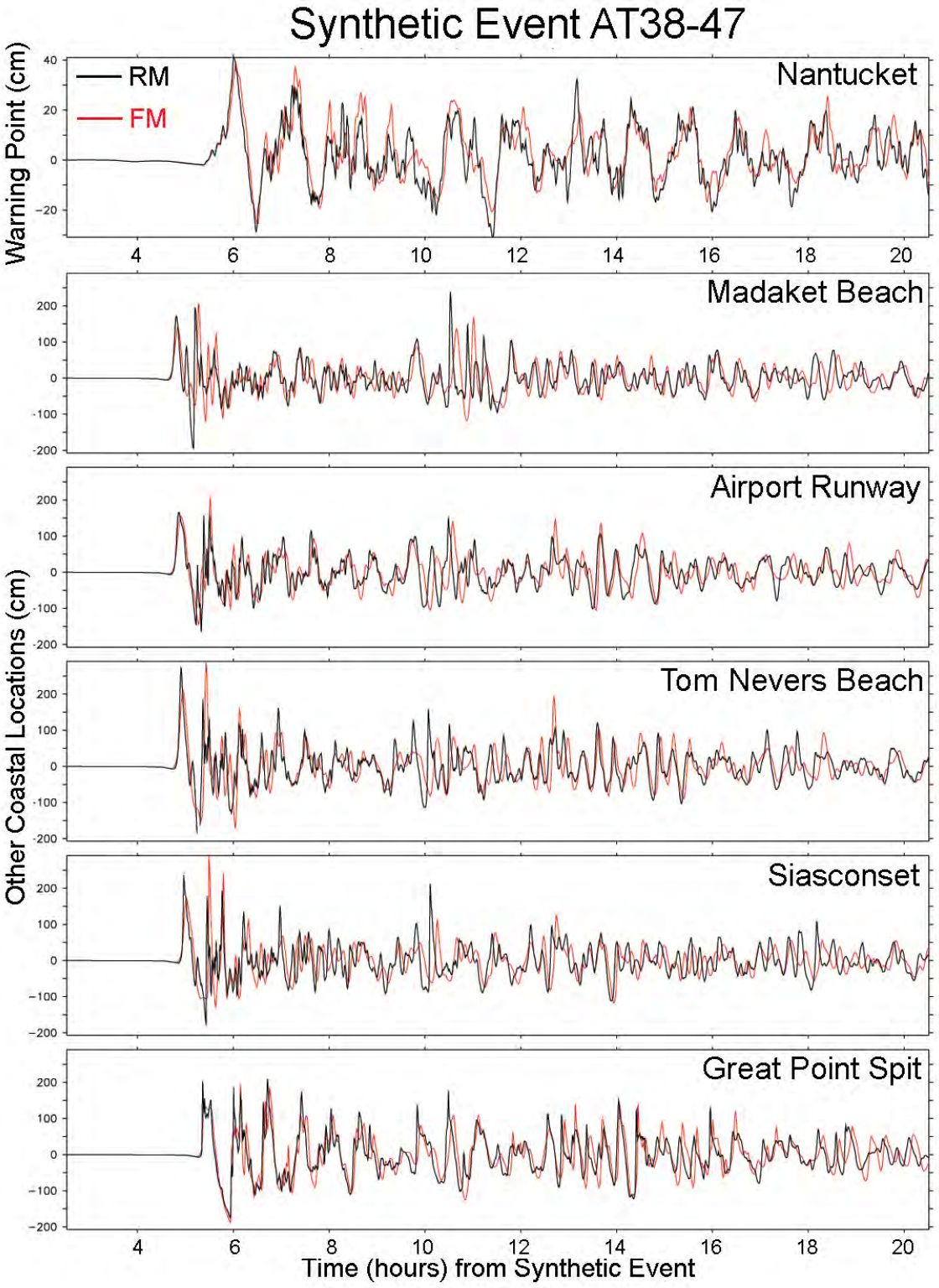

Figure 30: Comparison of the reference (RM, black) and forecast (FM, red) model wave height time series at the warning point (upper panel) and five other coastal sites during the ATSZ 38–47 mega-tsunami scenario.

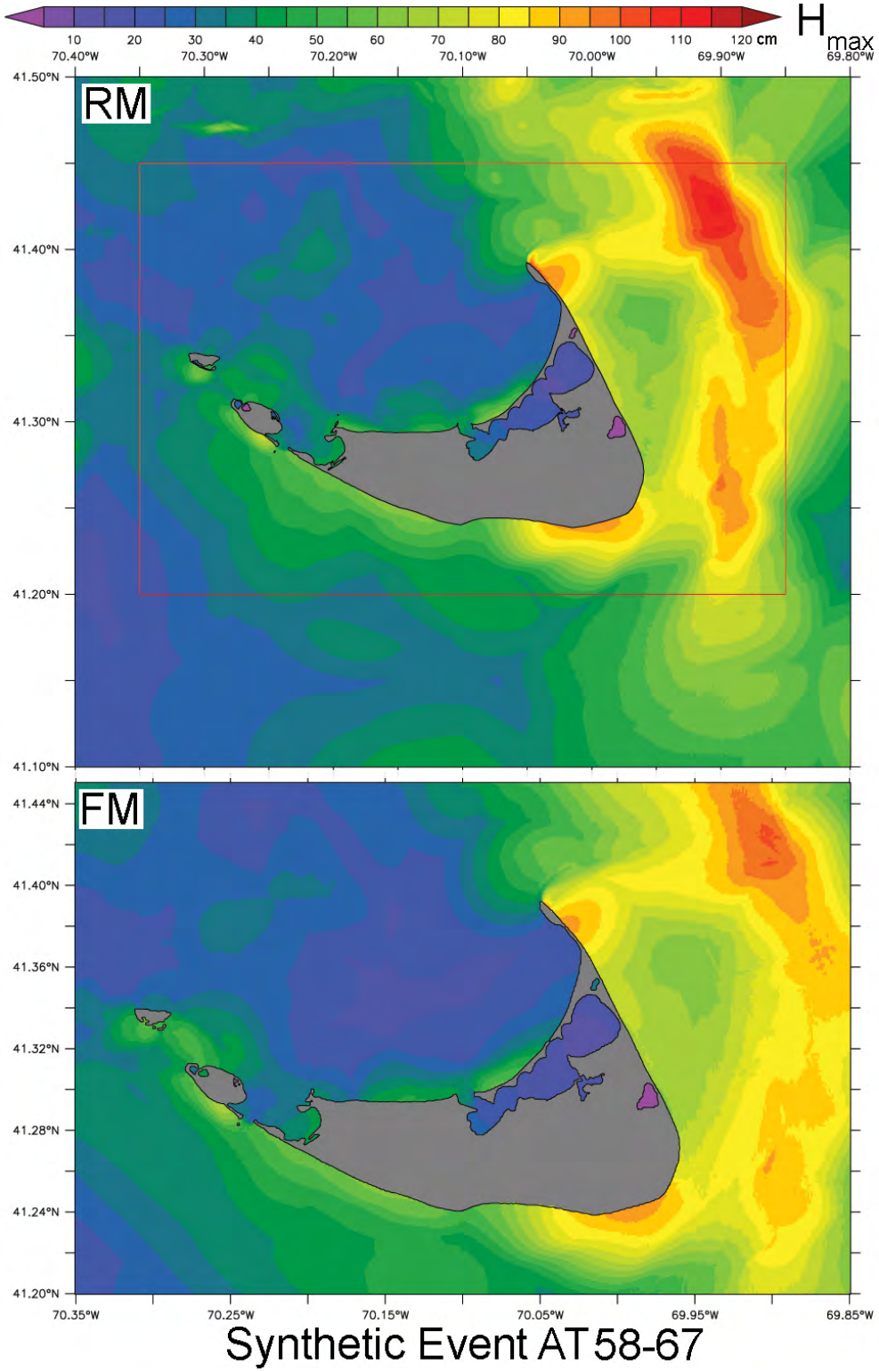

Figure 31: Comparison of the reference (RM, upper panel) and forecast (FM, lower panel) model maximum wave height (cm) of the innermost C grid for the ATSZ 58–67 mega-tsunami scenario.

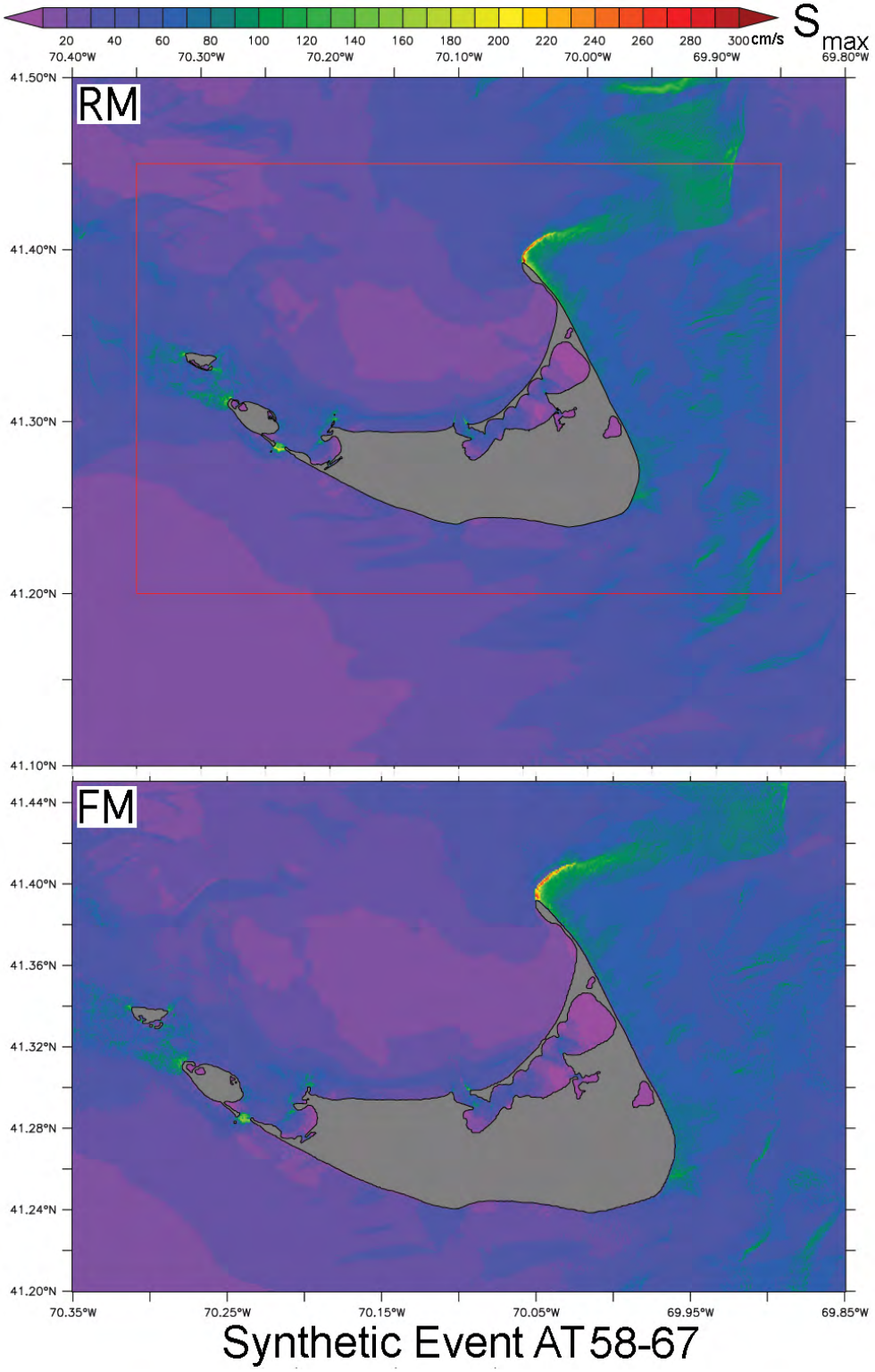

Figure 32: Comparison of the reference (RM, upper panel) and forecast (FM, lower panel) model maximum speed (cm/s) of the innermost C grid for the ATSZ 58–67 mega-tsunami scenario.

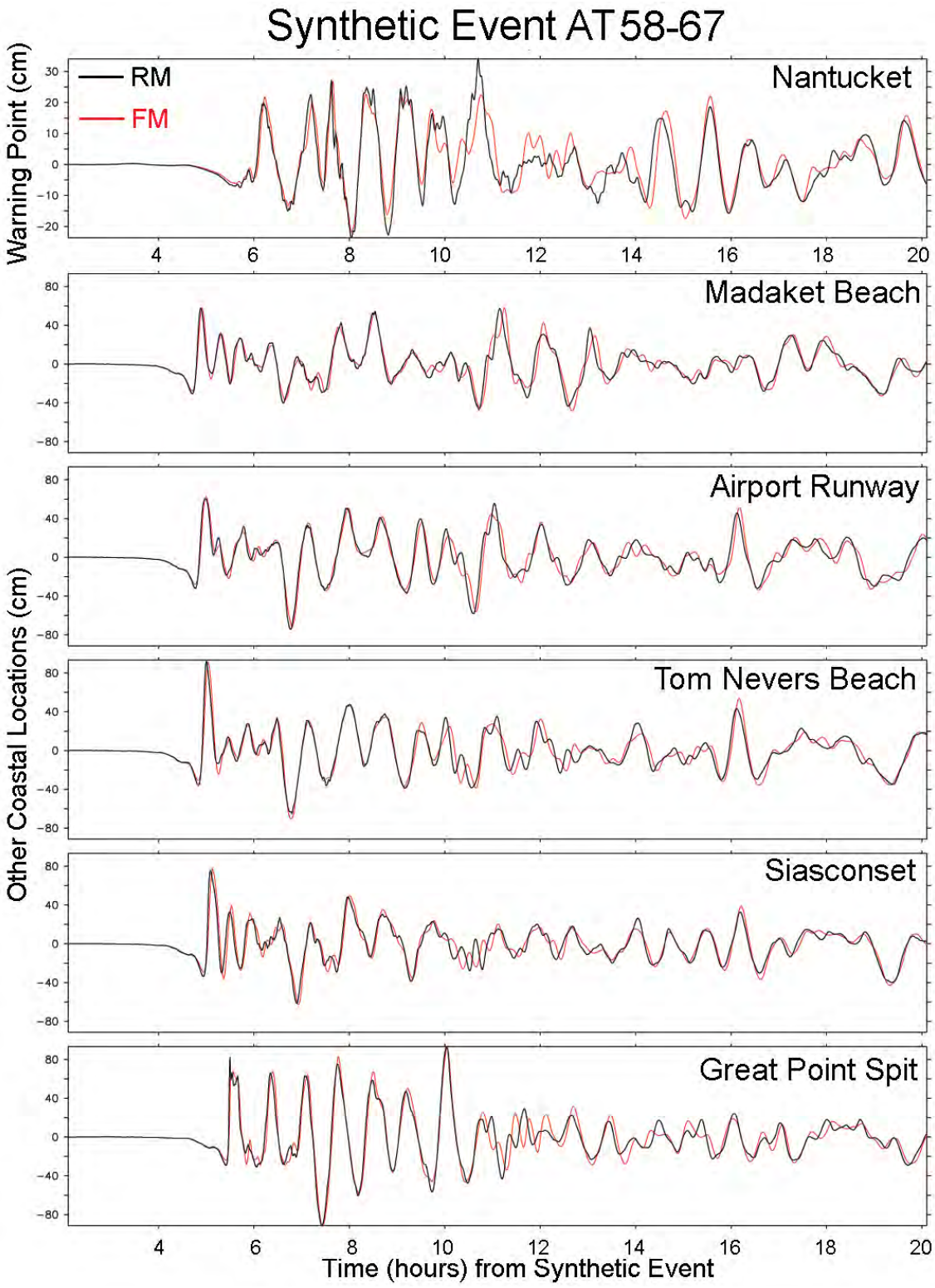

Figure 33: Comparison of the reference (RM, black) and forecast (FM, red) model wave height time series at the warning point (upper panel) and five other coastal sites during the ATSZ 58– 67 mega-tsunami scenario.

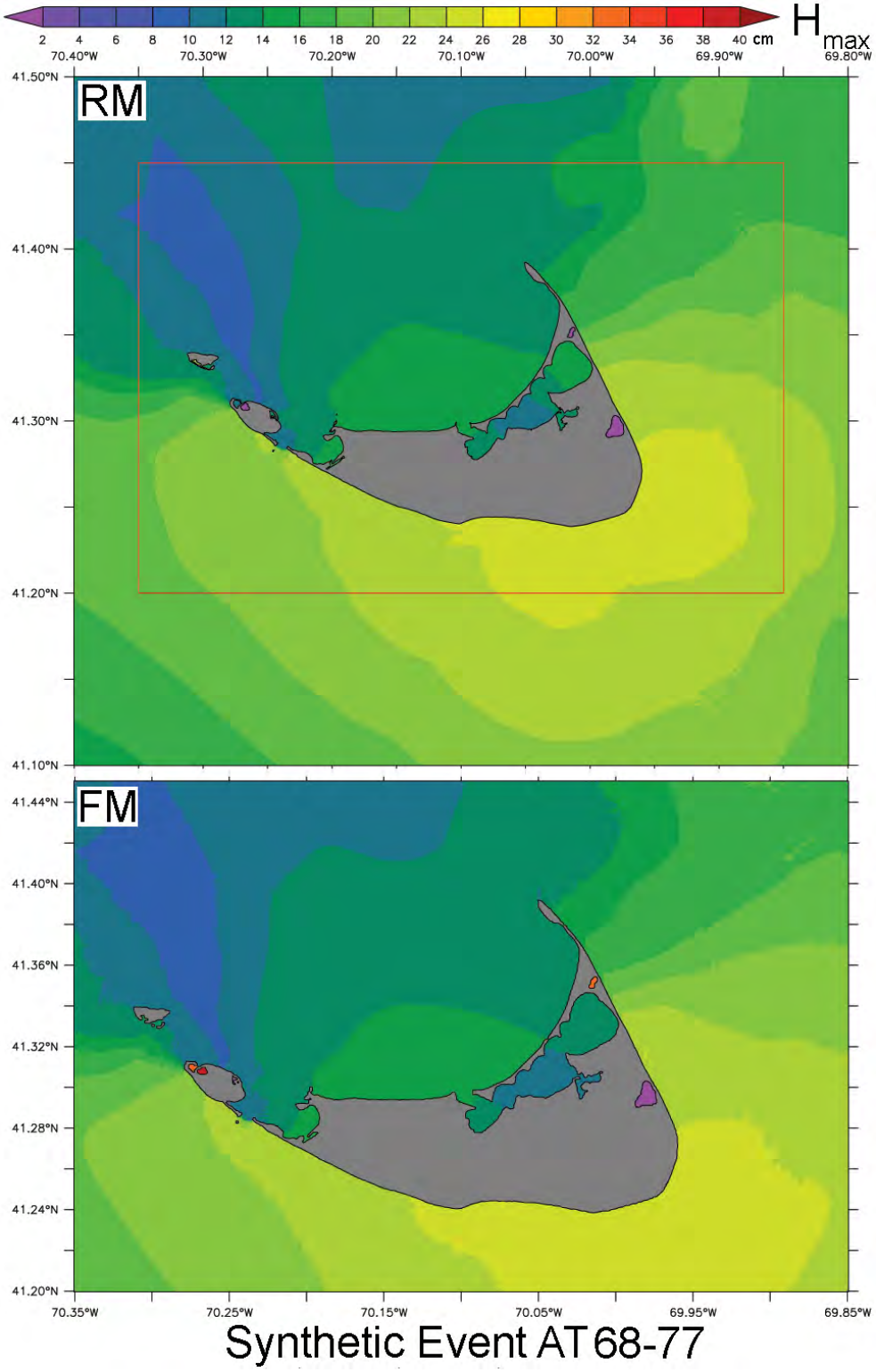

Figure 34: Comparison of the reference (RM, upper panel) and forecast (FM, lower panel) model maximum wave height (cm) of the innermost C grid for the ATSZ 68–77 mega-tsunami scenario.

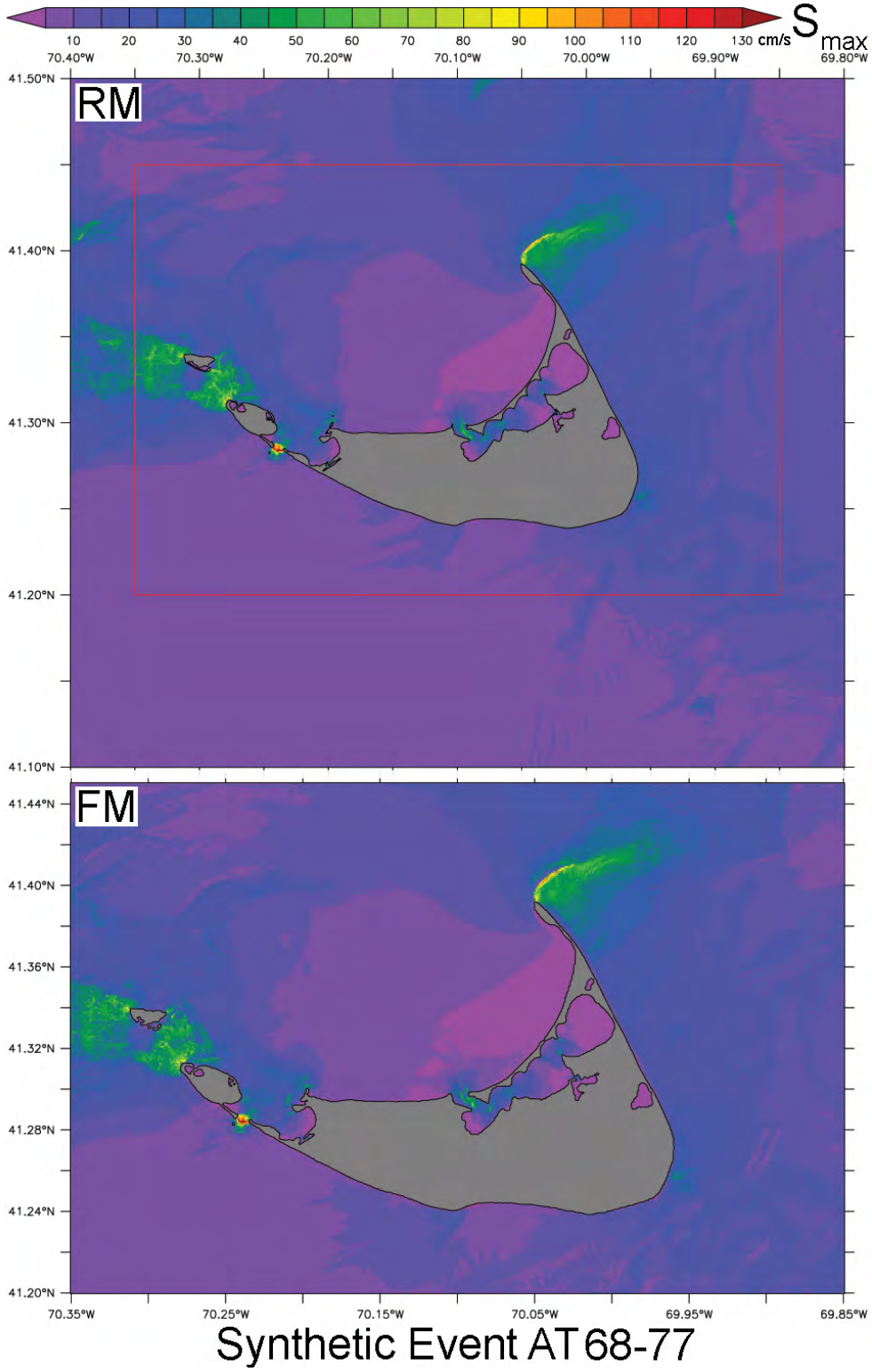

Figure 35: Comparison of the reference (RM, upper panel) and forecast (FM, lower panel) model maximum speed (cm/s) of the innermost C grid for the ATSZ 68–77 mega-tsunami scenario.

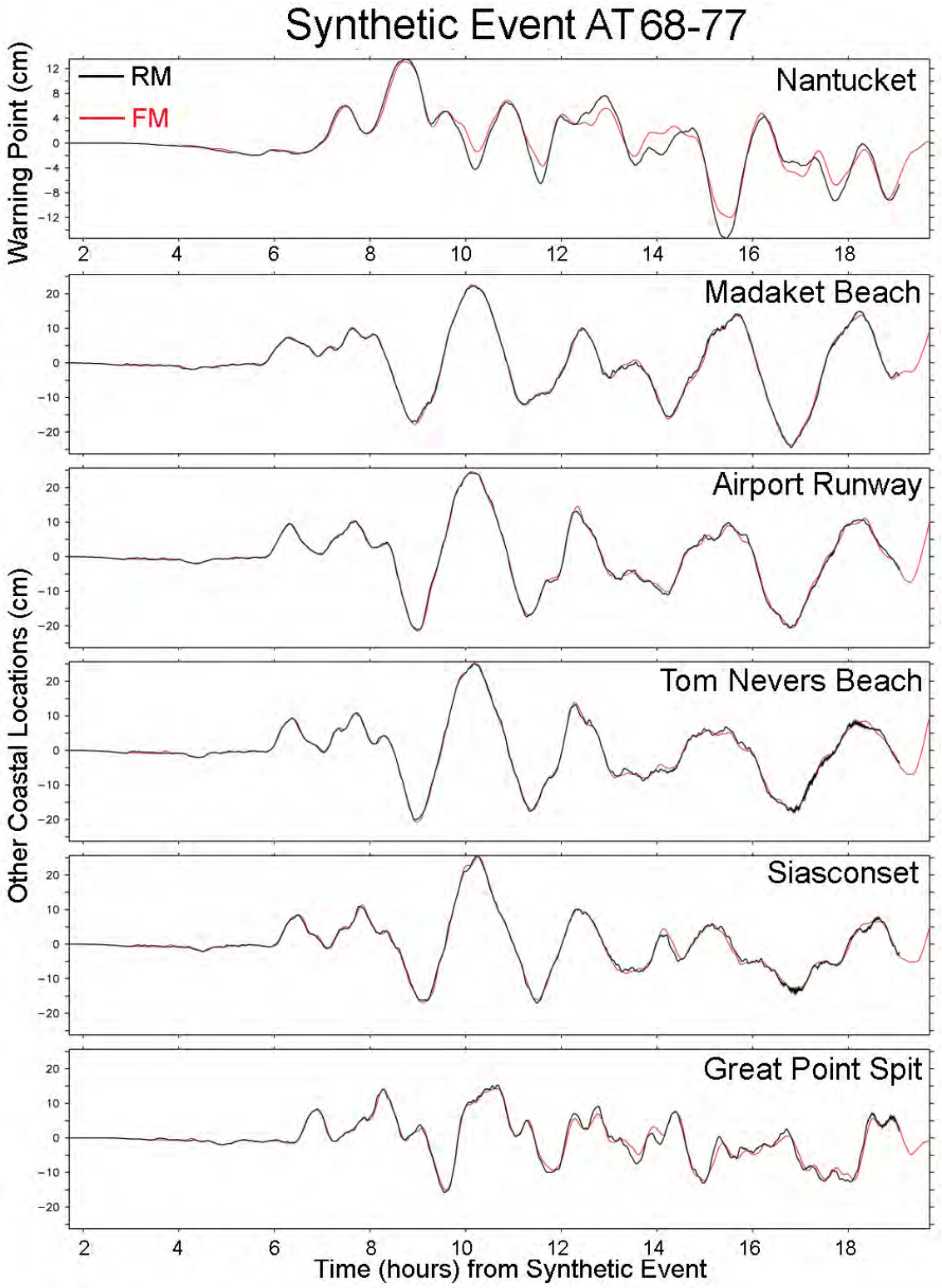

Figure 36: Comparison of the reference (RM, black) and forecast (FM, red) model wave height time series at the warning point (upper panel) and five other coastal sites during the ATSZ 68–77 mega-tsunami scenario.

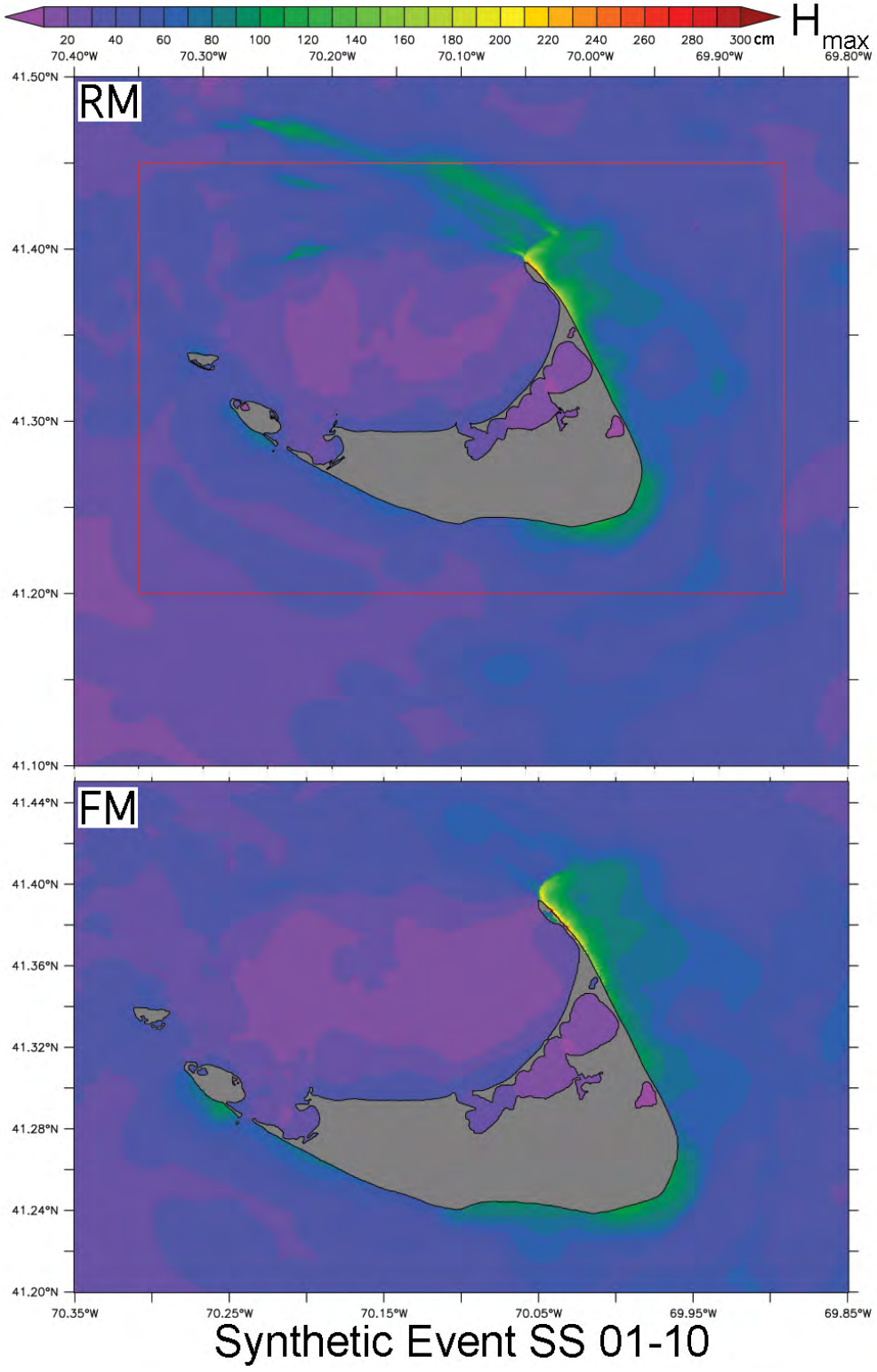

Figure 37: Comparison of the reference (RM, upper panel) and forecast (FM, lower panel) model maximum wave height (cm) of the innermost C grid for the SSSZ 01–10 mega-tsunami scenario.

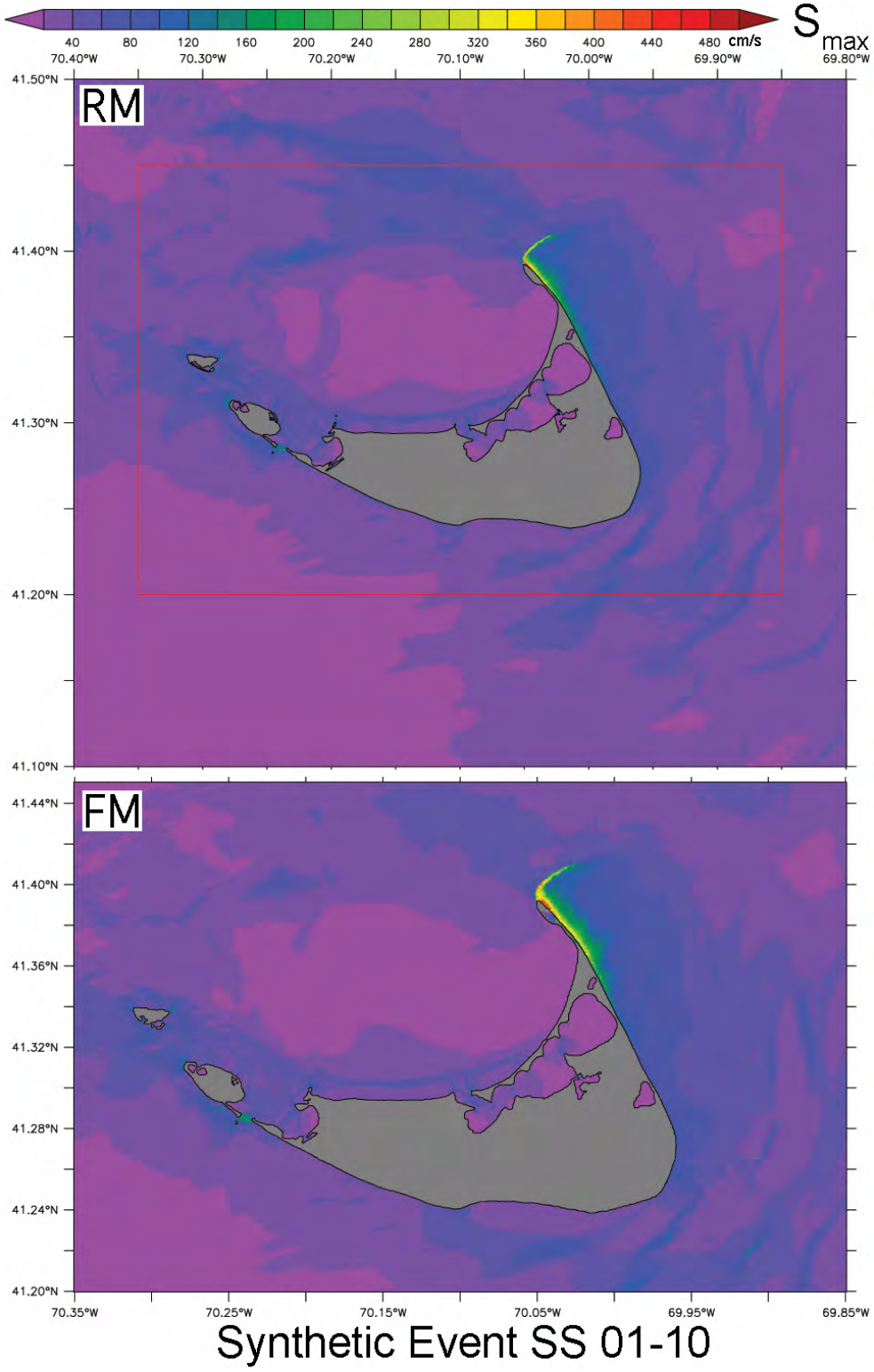

Figure 38: Comparison of the reference (RM, upper panel) and forecast (FM, lower panel) model maximum speed (cm/s) of the innermost C grid for the SSSZ 01–10 mega-tsunami scenario.

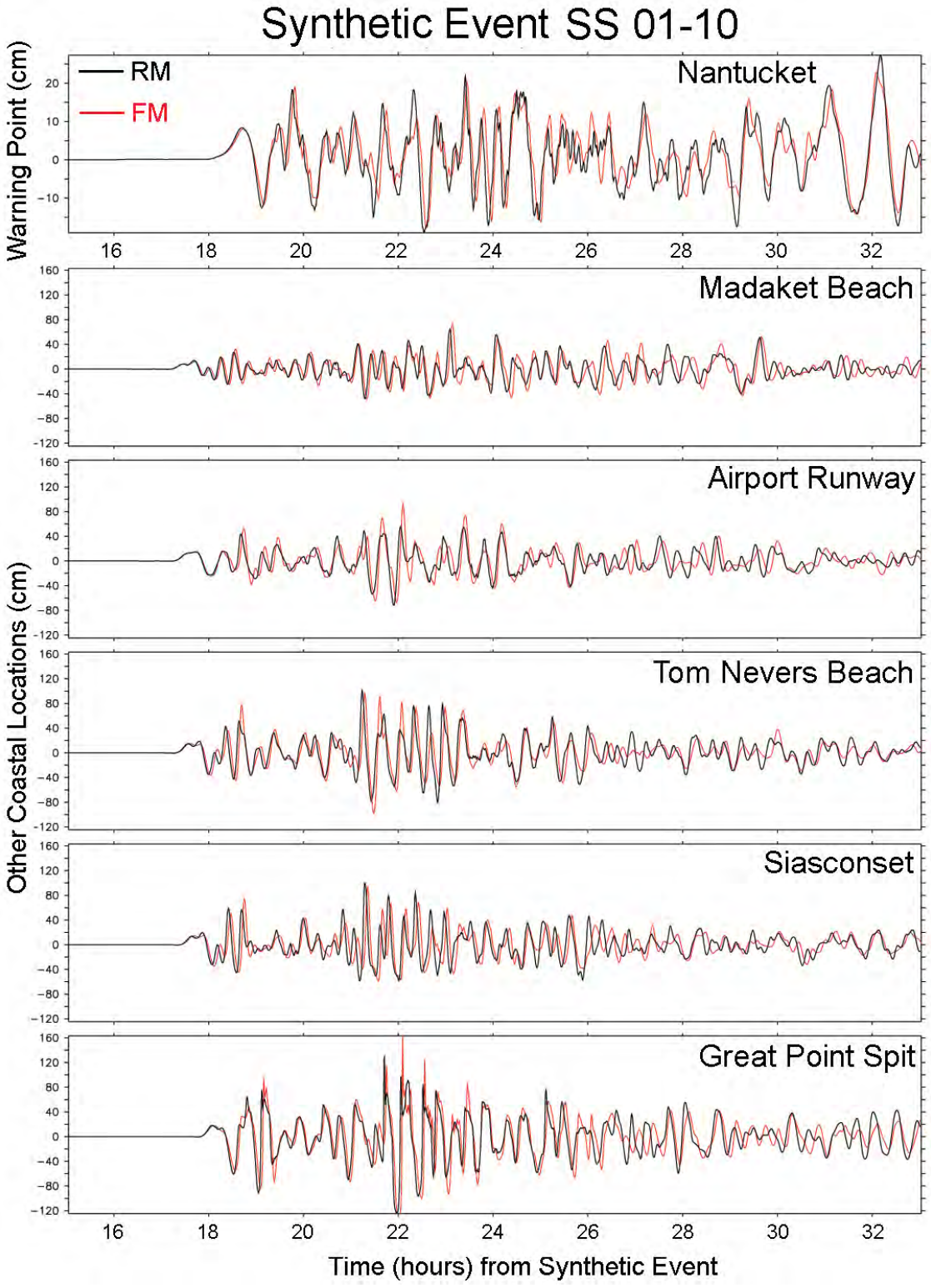

Figure 39: Comparison of the reference (RM, black) and forecast (FM, red) model wave height time series at the warning point (upper panel) and five other coastal sites during the SSSZ 01–10 mega-tsunami scenario.

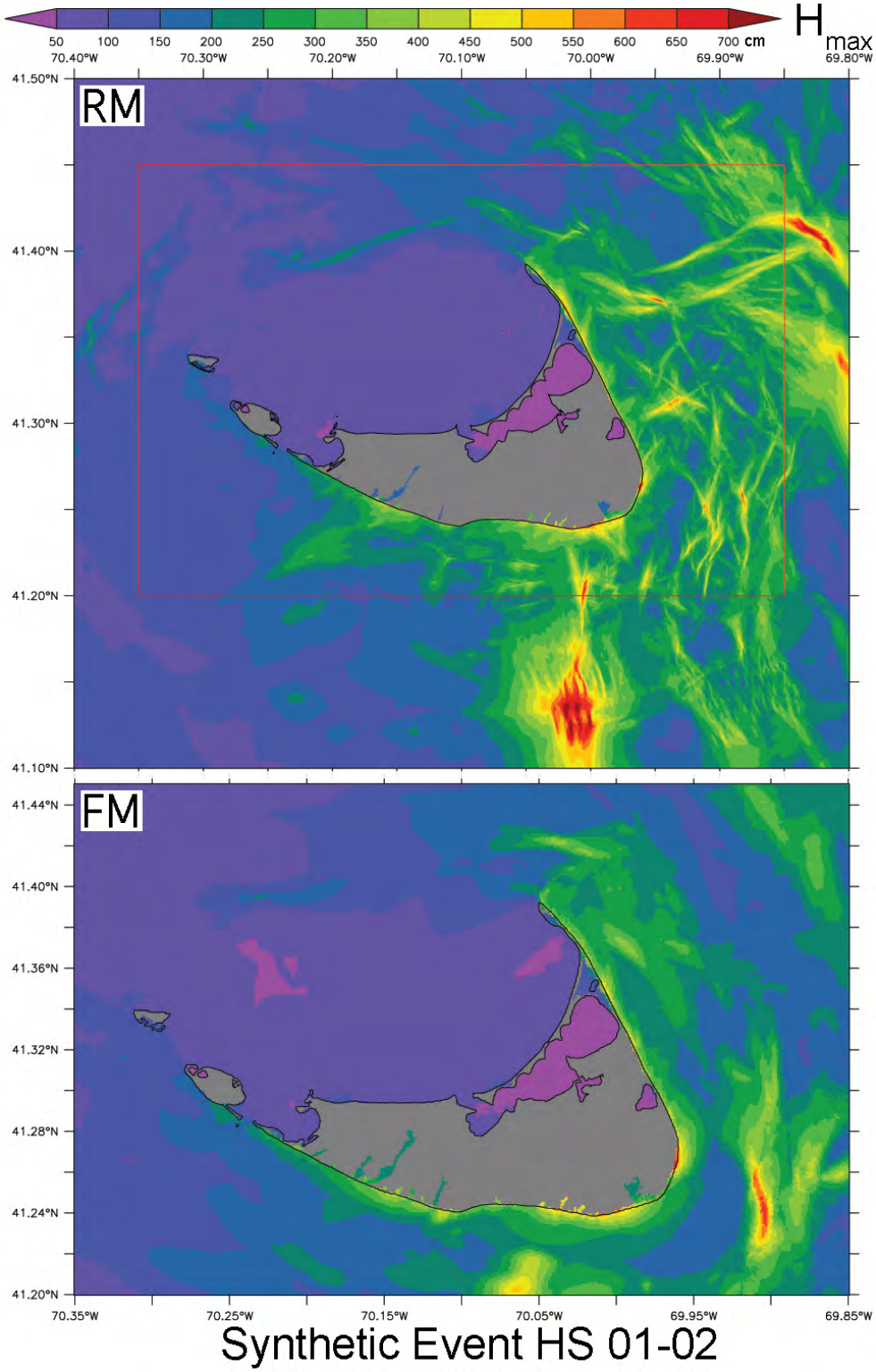

Figure 40: Comparison of the reference (RM, upper panel) and forecast (FM, lower panel) model maximum wave height (cm) of the innermost C grid for the HS 01–02 mega-tsunami scenario, located off Portugal as shown in **Figure 14**.

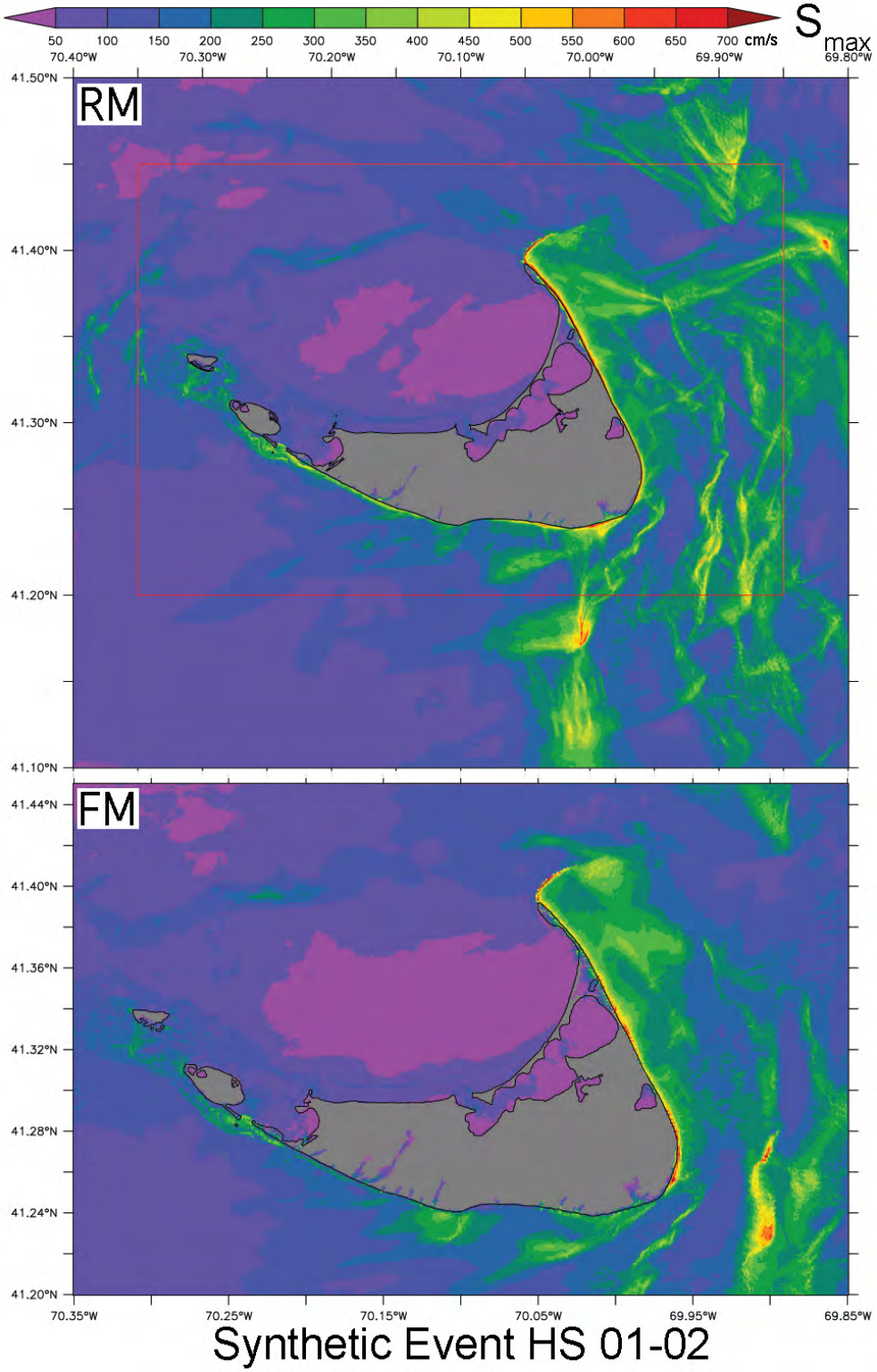

Figure 41: Comparison of the reference (RM, upper panel) and forecast (FM, lower panel) model maximum speed (cm/s) of the innermost C grid for the HS 01–02 mega-tsunami scenario.

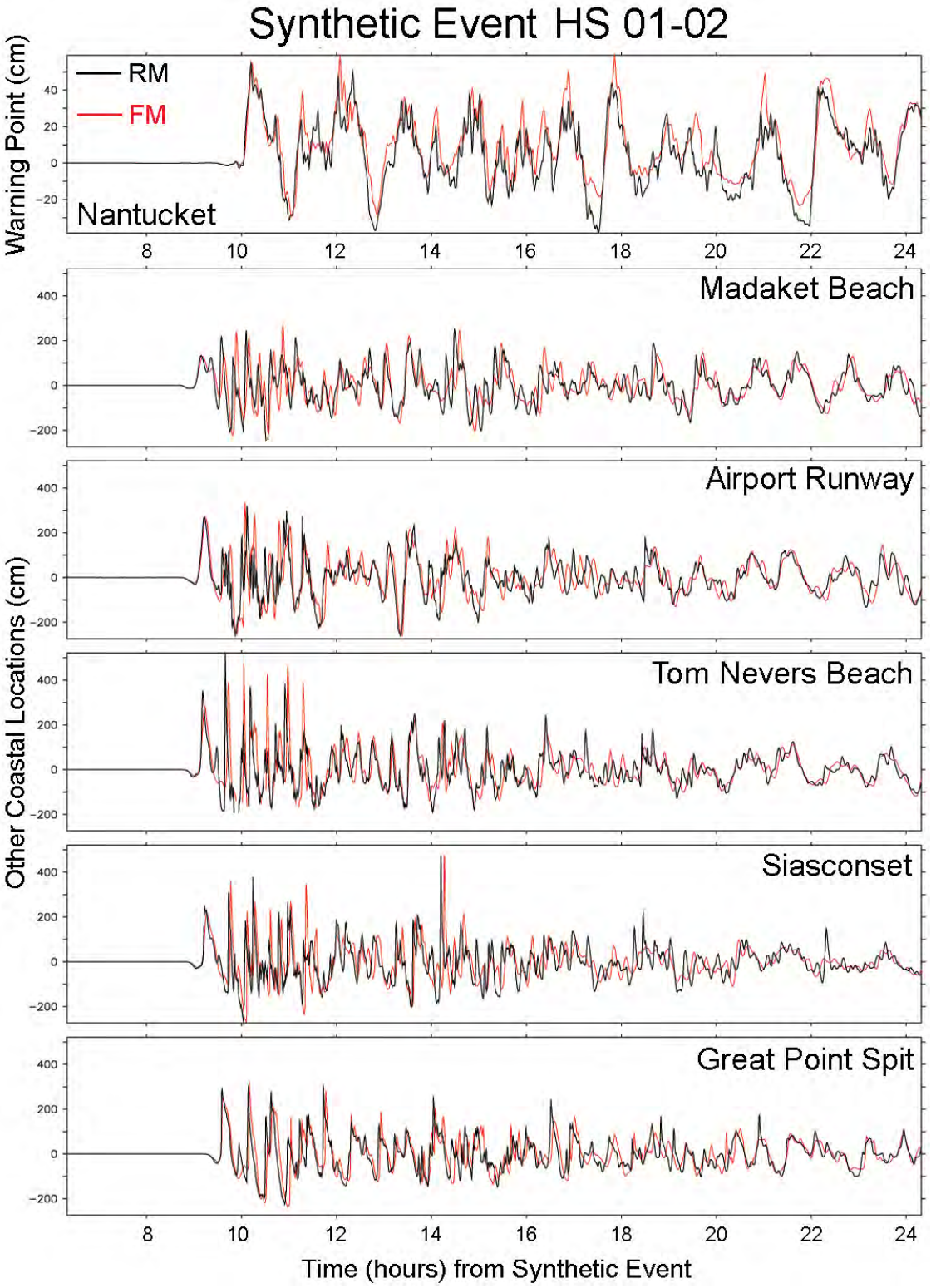

Figure 42: Comparison of the reference (RM, black) and forecast (FM, red) model wave height time series at the warning point (upper panel) and five other coastal sites during the HS 01–02 mega-tsunami scenario.

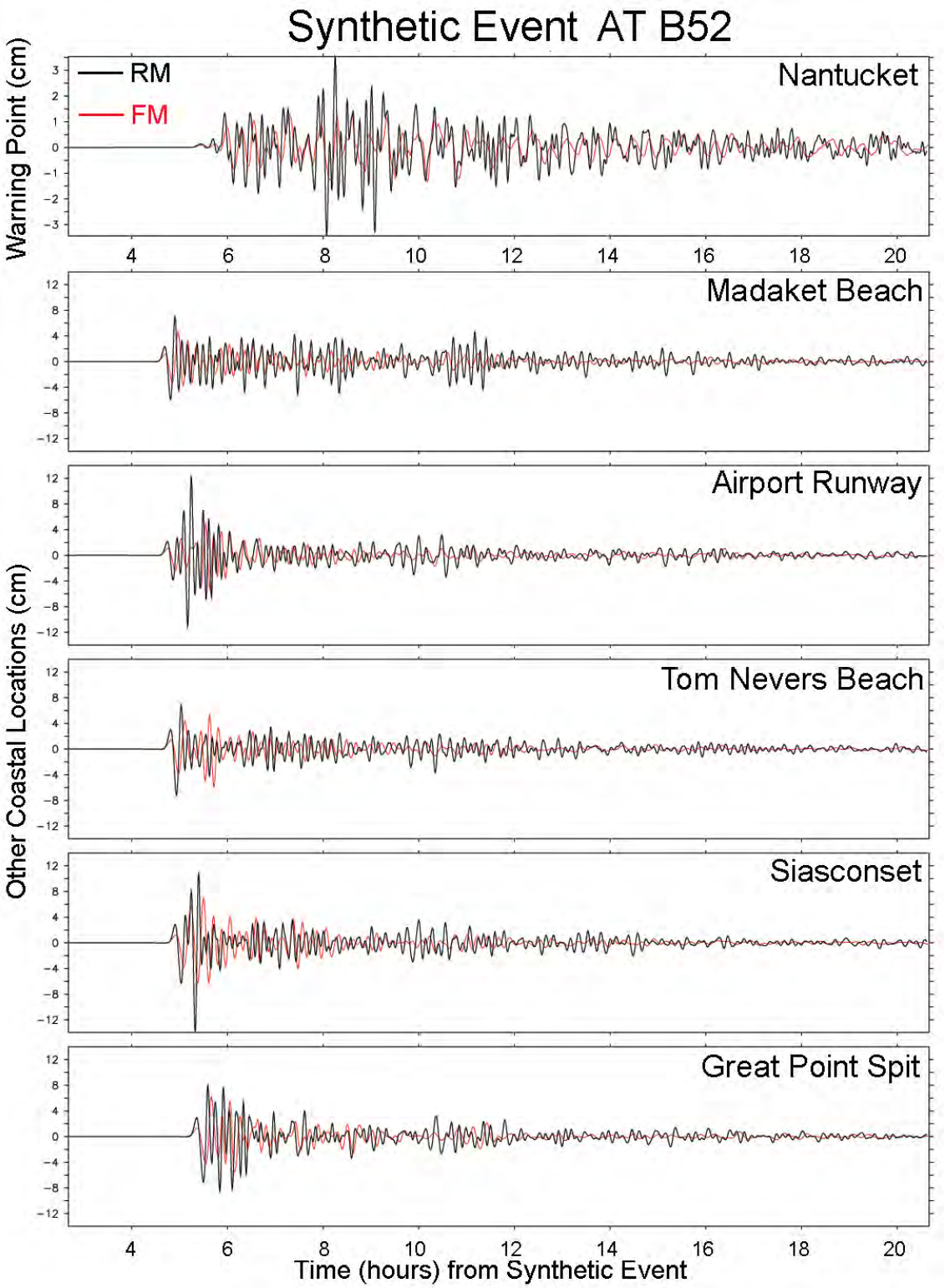

Figure 43: Comparison of the reference (RM, black) and forecast (FM, red) model wave height time series at the warning point (upper panel) and five other coastal sites during the ATSZ B52 scenario.

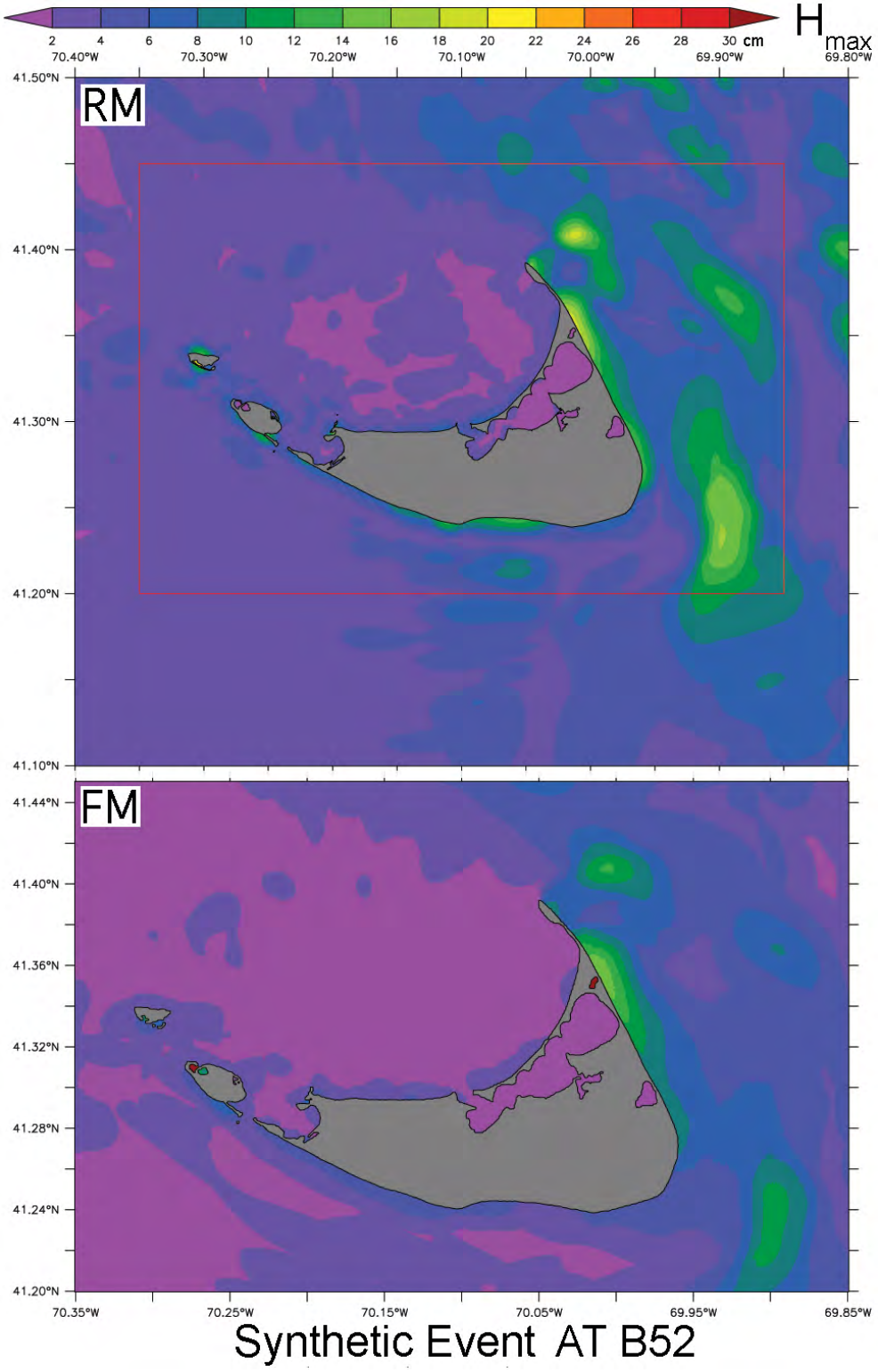

Figure 44: Comparison of the reference (RM, upper panel) and forecast (FM, lower panel) model maximum wave height (cm) of the innermost C grid for the ATSZ B52 scenario.

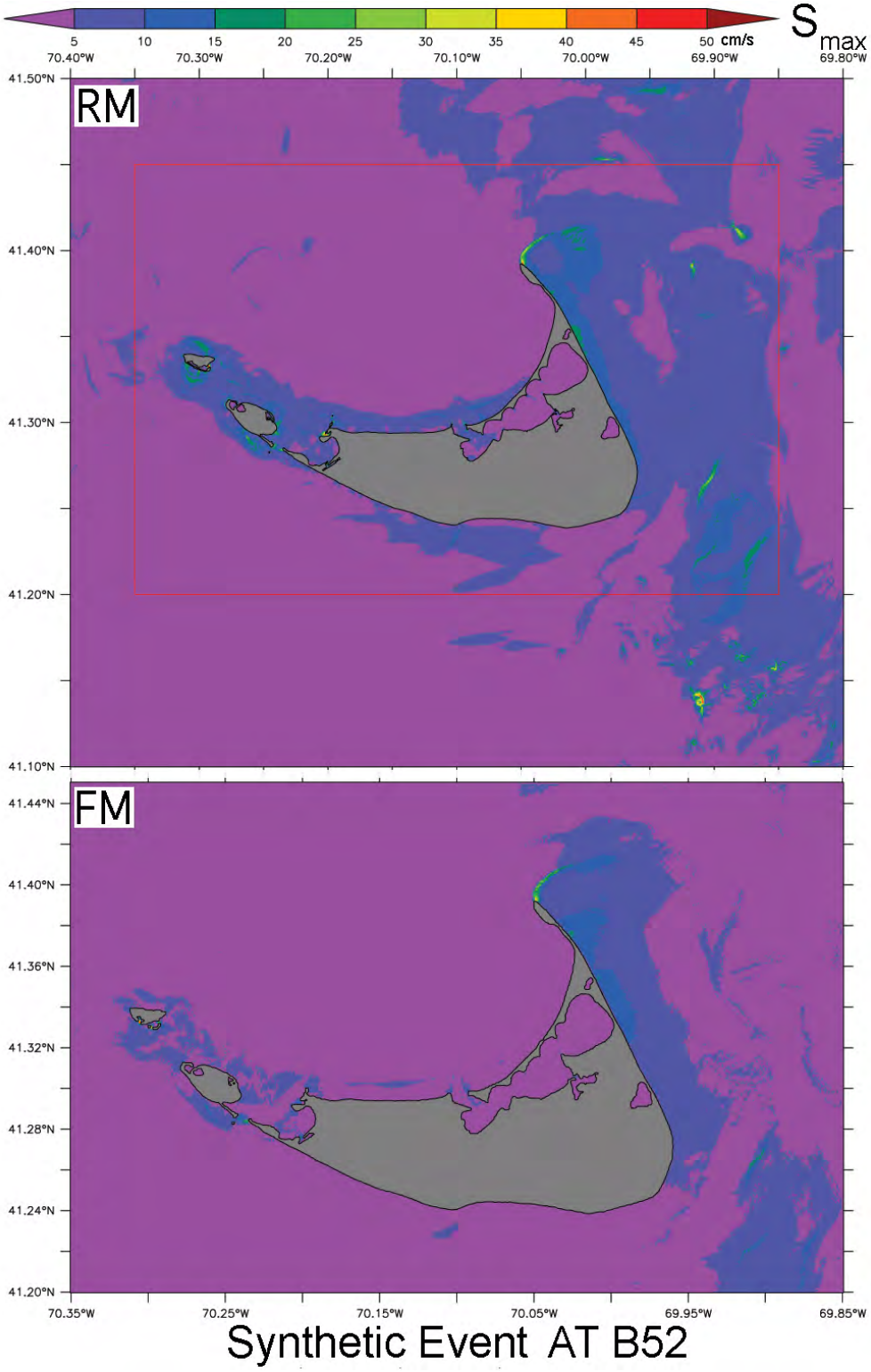

Figure 45: Comparison of the reference (RM, upper panel) and forecast (FM, lower panel) model maximum speed (cm/s) of the innermost C grid for the ATSZ B52 scenario.

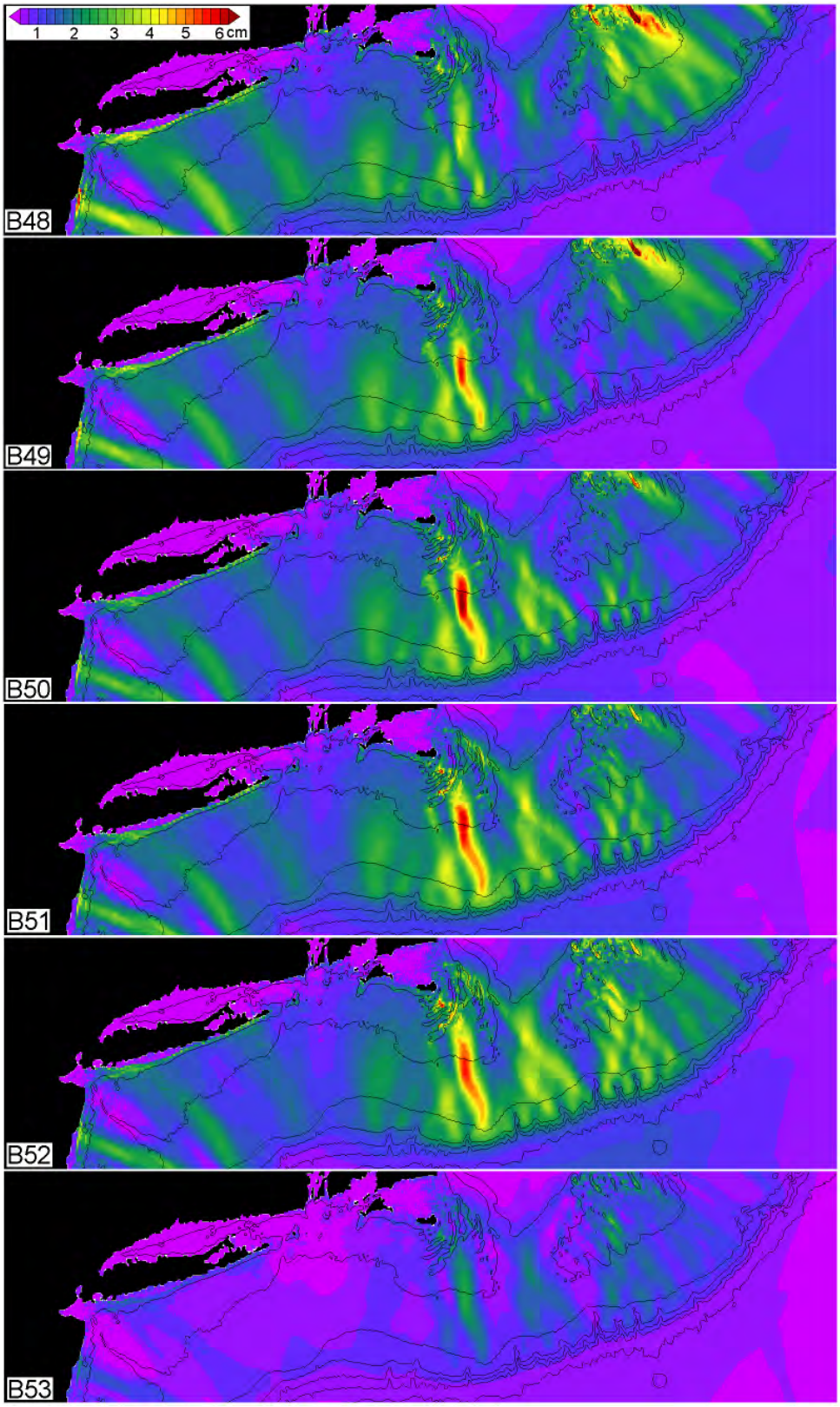

Figure 46: Bathymetry-related structures in the maximum wave response on the continental shelf seen in the forecast model A grid results.

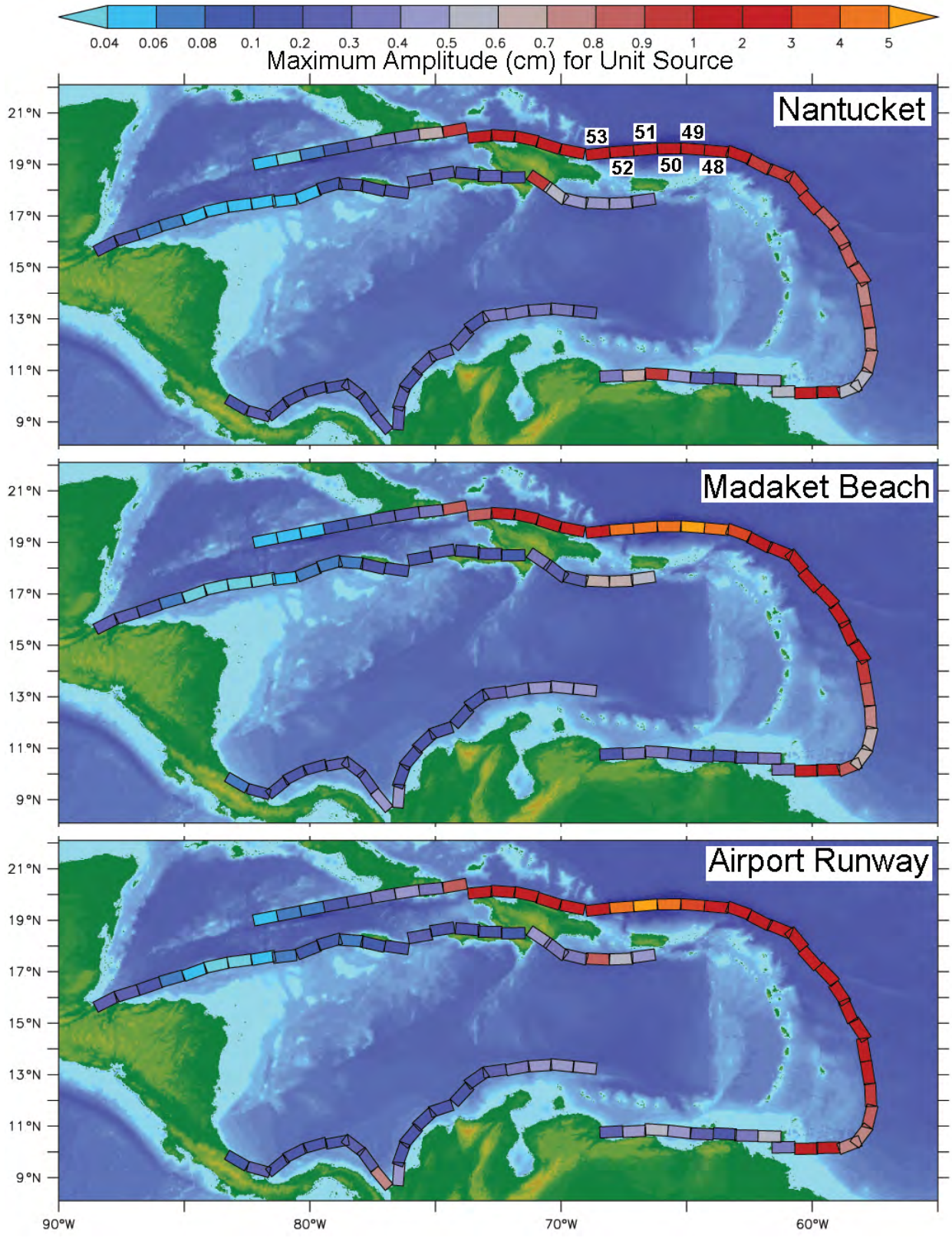

Figure 47: Maximum amplitude (cm) at the Nantucket warning point, Madaket Beach, and near the airport runway for wave trains from ATSZ unit sources.

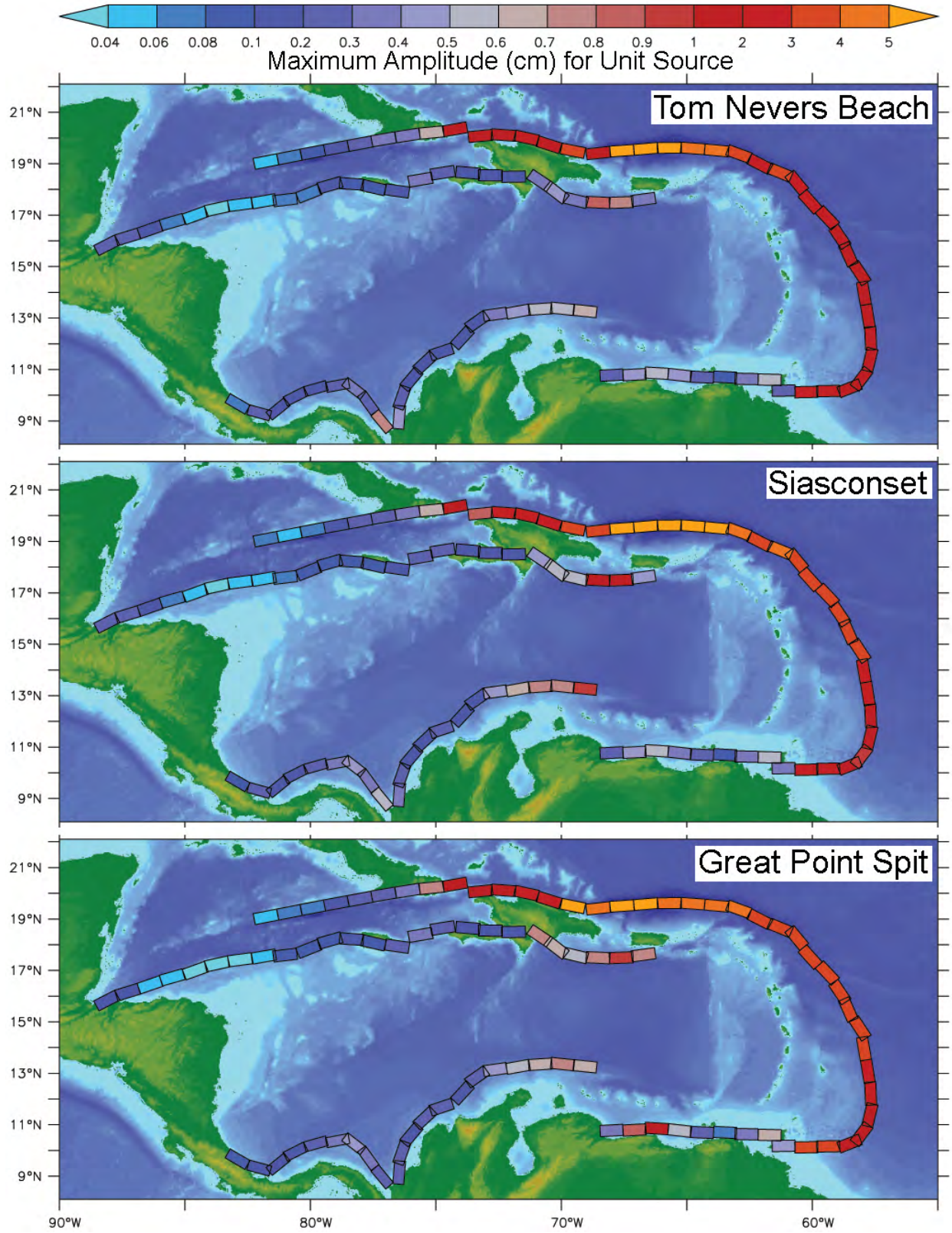

Figure 48: Maximum amplitude (cm) at Tom Nevers Beach, Siasconset, and near the Great Point spit for wave trains from ATSZ unit sources.

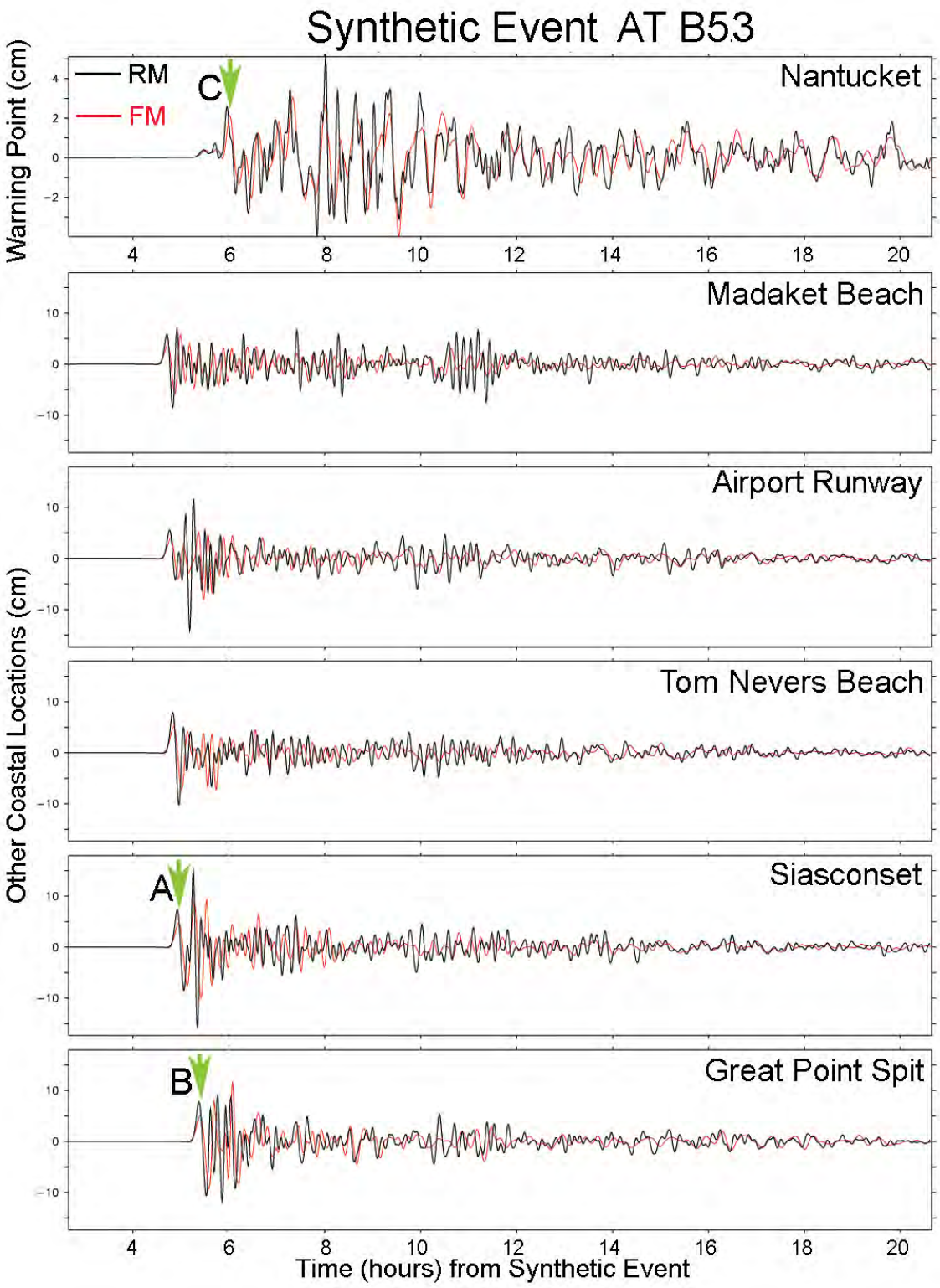

Figure 49: Comparison of the reference (RM, black) and forecast (FM, red) model wave height time series at the warning point (upper panel) and five other coastal sites during the ATSZ B53 scenario. Green arrows indicate discrete times (A, B, C) at which the reference and forecast model wave height and vector current fields are compared in **Figures 52–54**. Since no historical observations exist for Nantucket, this scenario is used as a proxy for the 1946 Dominican Republic event, which was observed elsewhere on the U.S. mainland.

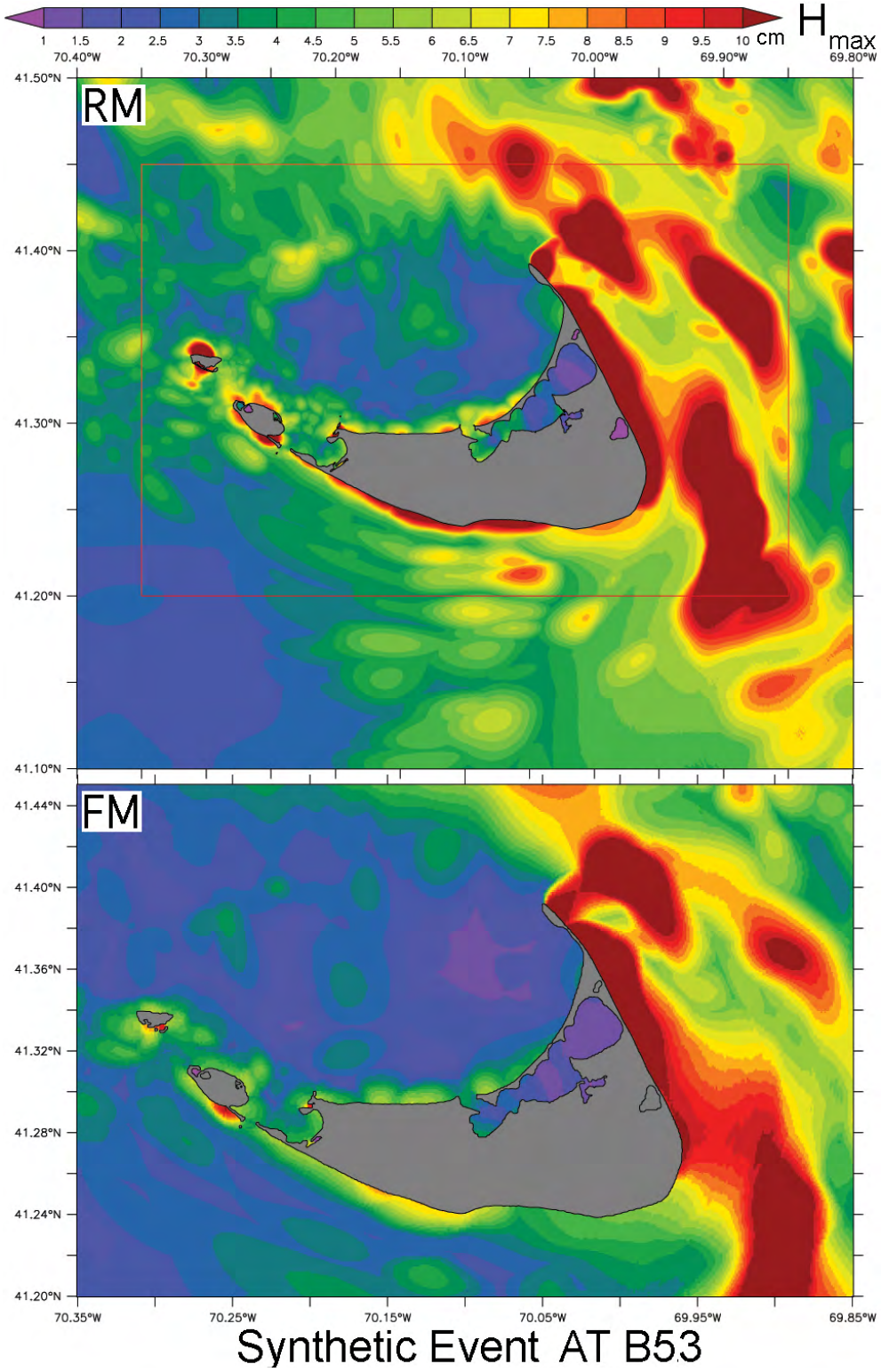

Figure 50: Comparison of the reference (RM, upper panel) and forecast (FM, lower panel) model maximum wave height (cm) of the innermost C grid for the ATSZ B53 scenario.

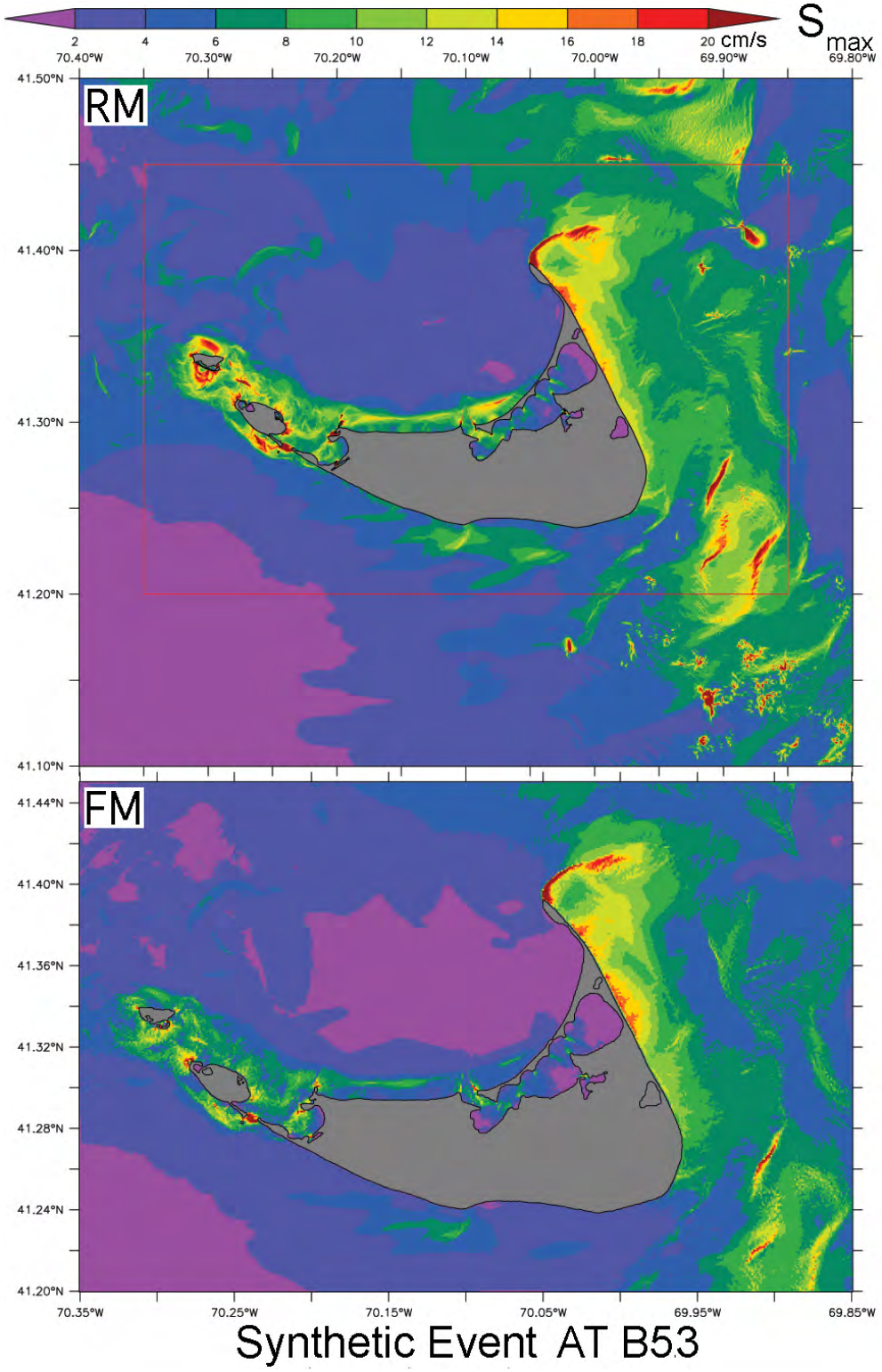

Figure 51: Comparison of the reference (RM, upper panel) and forecast (FM, lower panel) model maximum speed (cm/s) of the innermost C grid for the ATSZ B53 scenario. Both panels share a common color scale.

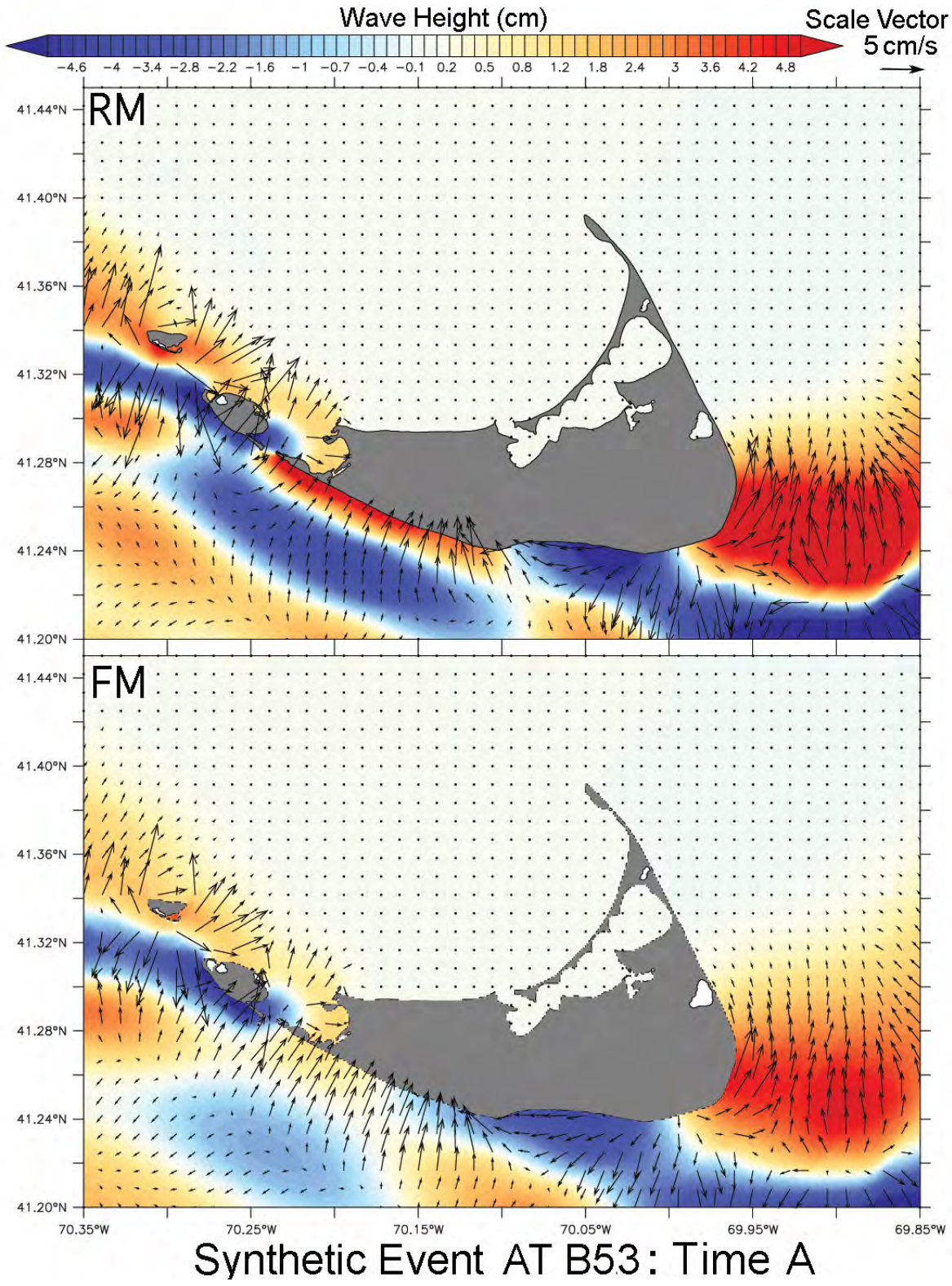

Figure 52: Comparison of the reference (RM, upper panel) and forecast (FM, lower panel) model wave height (cm) and vector current speed (cm/s) of the innermost C grid for the ATSZ B53 scenario. Time A: the leading wave crest reaches Siasconset.

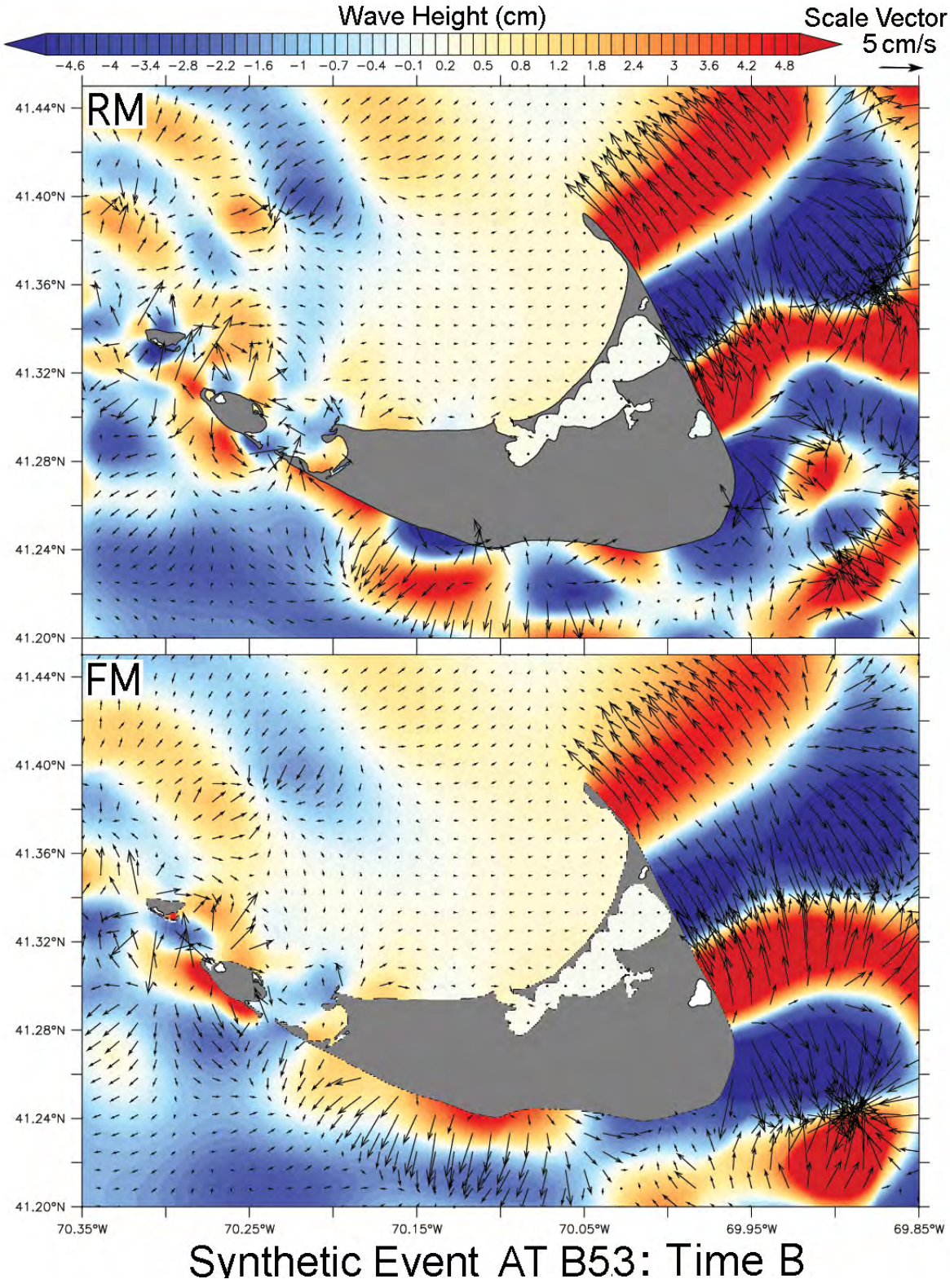

Figure 53: Comparison of the reference (RM, upper panel) and forecast (FM, lower panel) model wave height (cm) and vector current speed (cm/s) of the innermost C grid for the ATSZ B53 scenario. Time B: the leading wave crest reaches Great Point Spit.

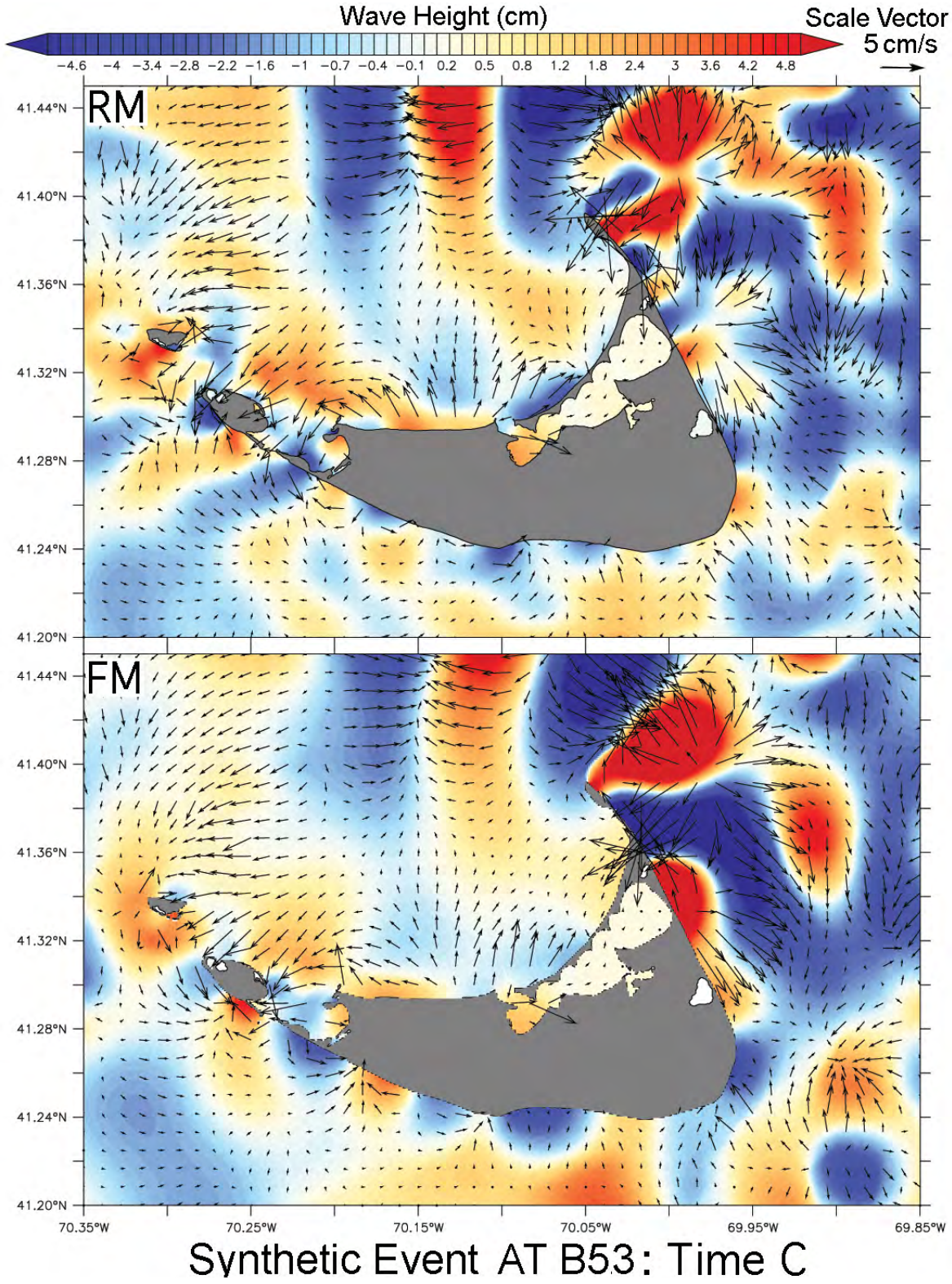

Figure 54: Comparison of the reference (RM, upper panel) and forecast (FM, lower panel) model wave height (cm) and vector current speed (cm/s) of the innermost C grid for the ATSZ B53 scenario. Time C: the leading wave crest reaches Nantucket Harbor.

Appendix A. Model input files for Nantucket, Massachusetts

As discussed in Section 3.5, input files providing model parameters, the file names of the nested grids, and the output specifications are necessary in order to run the model in either its reference or forecast mode. These files are provided below; each record contains the value(s) and an annotation of purpose.

A1. Reference model *.in file for Nantucket, Massachusetts

The following table contains the parameter and file choices used in the input file for the SIFT implementation (most3_facts_nc.in) of the reference model (RM) for Nantucket, Massachusetts. When run on an Intel® Xeon® E5670 2.93 GHz processor during development the model simulated 4 hr in 4.42 CPU hr.

```
0.001                          Minimum amplitude of input offshore wave (m)
1                              Minimum depth of offshore (m)
0.1                            Dry land depth of inundation (m)
0.0009                         Friction coefficient (n**2)
1                              Let A Grid and B Grid run up
300.0                          Max eta before blow-up (m)
1.25                           Time step (sec)
23040                          Total number of time steps in run
2                              Time steps between A-grid computations
2                              Time steps between B-grid computations
24                             Time steps between output steps
0                              Time steps before saving first output step
1                              Save output every n-th grid point, n=
bathy/NantucketMA_RM_A.
   most                        A-grid bathymetry file
bathy/NantucketMA_RM_B.
   most                        B-grid bathymetry file
bathy/NantucketMA_RM_C.
   most                        C-grid bathymetry file
./                             Directory of source files
./                             Directory for output files
1 1 1 1                        netCDF output for A, B, C, SIFT
1                              Number of time series locations
3 333 155                      Grid & cell indices for reference point
```

A2. Forecast model *.in file for Nantucket, Massachusetts

The following table contains the parameter and file choices used in the input file for the SIFT implementation (most3_facts_nc.in) of the optimized forecast model (FM) for Nantucket, Massachusetts. When run on an Intel® Xeon® E5670 2.93 GHz processor the model simulates 4 hr in under 8.2 min, satisfying the 10 min target for this metric.

```
0.005                          Minimum amplitude of input offshore wave (m)
1                              Minimum depth of offshore (m)
0.1                            Dry land depth of inundation (m)
0.0009                         Friction coefficient (n**2)
1                              Let A Grid and B Grid run up
300.0                          Max eta before blow-up (m)
3.75                           Time step (sec)
7680                           Total number of time steps in run
1                              Time steps between A-grid computations
2                              Time steps between B-grid computations
8                              Time steps between output steps
0                              Time steps before saving first output step
1                              Save output every n-th grid point, n=
bathy/NantucketMA_FM_A.
    most                       A-grid bathymetry file
bathy/NantucketMA_FM_B.
    most                       B-grid bathymetry file
bathy/NantucketMA_FM_C.
    most                       C-grid bathymetry file
./                             Directory of source files
./                             Directory for output files
1 1 1 1                        netCDF output for A, B, C, SIFT
1                              Number of time series locations
3 230 198                      Grid & cell indices for reference point
```

Appendix B. Propagation Database

Atlantic Ocean Unit Sources

The NOAA propagation database presented in this section is the representation of the database as of March 2013, and may not be the most current version of the database available upon publication.

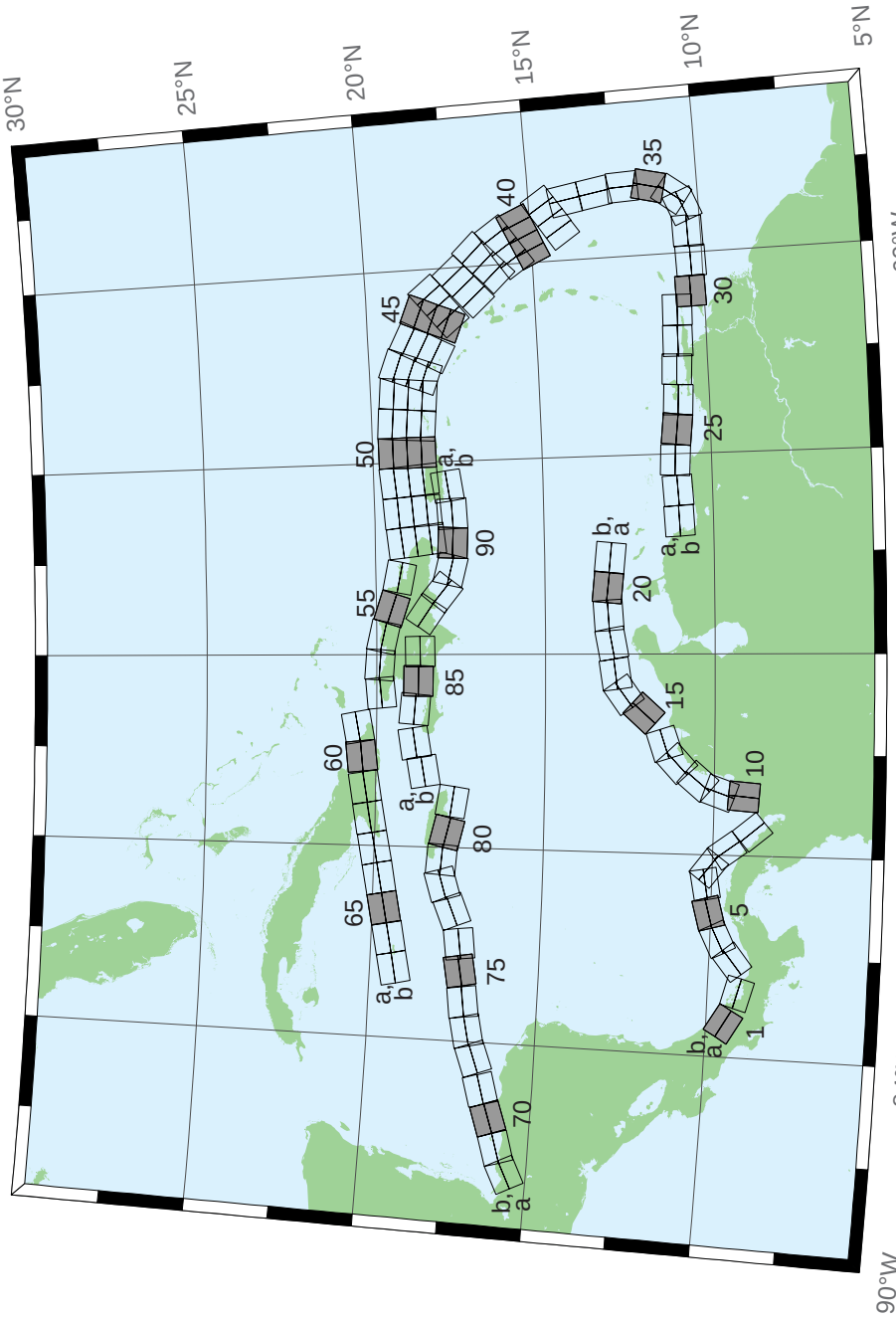

Figure B1: Atlantic Source Zone unit sources.

Table B1: Earthquake parameters for Atlantic Source Zone unit sources.

Segment	Description	Longitude (°E)	Latitude (°N)	Strike (°)	Dip (°)	Depth (km)
atsz-1a	Atlantic	-83.2020	9.1449	120	27.5	28.09
atsz-1b	Atlantic	-83.0000	9.4899	120	27.5	5
atsz-2a	Atlantic	-82.1932	8.7408	105.1	27.5	28.09
atsz-2b	Atlantic	-82.0880	9.1254	105.1	27.5	5
atsz-3a	Atlantic	-80.9172	9.0103	51.31	30	30
atsz-3b	Atlantic	-81.1636	9.3139	51.31	30	5
atsz-4a	Atlantic	-80.3265	9.4308	63.49	30	30
atsz-4b	Atlantic	-80.5027	9.7789	63.49	30	5
atsz-5a	Atlantic	-79.6247	9.6961	74.44	30	30
atsz-5b	Atlantic	-79.7307	10.0708	74.44	30	5
atsz-6a	Atlantic	-78.8069	9.8083	79.71	30	30
atsz-6b	Atlantic	-78.8775	10.1910	79.71	30	5
atsz-7a	Atlantic	-78.6237	9.7963	127.2	30	30
atsz-7b	Atlantic	-78.3845	10.1059	127.2	30	5
atsz-8a	Atlantic	-78.1693	9.3544	143.8	30	30
atsz-8b	Atlantic	-77.8511	9.5844	143.8	30	5
atsz-9a	Atlantic	-77.5913	8.5989	139.9	30	30
atsz-9b	Atlantic	-77.2900	8.8493	139.9	30	5
atsz-10a	Atlantic	-75.8109	9.0881	4.67	17	19.62
atsz-10b	Atlantic	-76.2445	9.1231	4.67	17	5
atsz-11a	Atlantic	-75.7406	9.6929	19.67	17	19.62
atsz-11b	Atlantic	-76.1511	9.8375	19.67	17	5
atsz-12a	Atlantic	-75.4763	10.2042	40.4	17	19.62
atsz-12b	Atlantic	-75.8089	10.4826	40.4	17	5
atsz-13a	Atlantic	-74.9914	10.7914	47.17	17	19.62
atsz-13b	Atlantic	-75.2890	11.1064	47.17	17	5
atsz-14a	Atlantic	-74.5666	11.0708	71.68	17	19.62
atsz-14b	Atlantic	-74.7043	11.4786	71.68	17	5
atsz-15a	Atlantic	-73.4576	11.8012	42.69	17	19.62
atsz-15b	Atlantic	-73.7805	12.0924	42.69	17	5
atsz-16a	Atlantic	-72.9788	12.3365	54.75	17	19.62
atsz-16b	Atlantic	-73.2329	12.6873	54.75	17	5
atsz-17a	Atlantic	-72.5454	12.5061	81.96	17	19.62
atsz-17b	Atlantic	-72.6071	12.9314	81.96	17	5
atsz-18a	Atlantic	-71.6045	12.6174	79.63	17	19.62
atsz-18b	Atlantic	-71.6839	13.0399	79.63	17	5
atsz-19a	Atlantic	-70.7970	12.7078	86.32	17	19.62
atsz-19b	Atlantic	-70.8253	13.1364	86.32	17	5
atsz-20a	Atlantic	-70.0246	12.7185	95.94	17	19.62
atsz-20b	Atlantic	-69.9789	13.1457	95.94	17	5
atsz-21a	Atlantic	-69.1244	12.6320	95.94	17	19.62
atsz-21b	Atlantic	-69.0788	13.0592	95.94	17	5
atsz-22a	Atlantic	-68.0338	11.4286	266.9	15	17.94

continued on next page

Table B1: (continued)

Segment	Description	Longitude (°E)	Latitude (°N)	Strike (°)	Dip (°)	Depth (km)
atsz-22b	Atlantic	-68.0102	10.9954	266.9	15	5
atsz-23a	Atlantic	-67.1246	11.4487	266.9	15	17.94
atsz-23b	Atlantic	-67.1010	11.0155	266.9	15	5
atsz-24a	Atlantic	-66.1656	11.5055	273.3	15	17.94
atsz-24b	Atlantic	-66.1911	11.0724	273.3	15	5
atsz-25a	Atlantic	-65.2126	11.4246	276.4	15	17.94
atsz-25b	Atlantic	-65.2616	10.9934	276.4	15	5
atsz-26a	Atlantic	-64.3641	11.3516	272.9	15	17.94
atsz-26b	Atlantic	-64.3862	10.9183	272.9	15	5
atsz-27a	Atlantic	-63.4472	11.3516	272.9	15	17.94
atsz-27b	Atlantic	-63.4698	10.9183	272.9	15	5
atsz-28a	Atlantic	-62.6104	11.2831	271.1	15	17.94
atsz-28b	Atlantic	-62.6189	10.8493	271.1	15	5
atsz-29a	Atlantic	-61.6826	11.2518	271.6	15	17.94
atsz-29b	Atlantic	-61.6947	10.8181	271.6	15	5
atsz-30a	Atlantic	-61.1569	10.8303	269	15	17.94
atsz-30b	Atlantic	-61.1493	10.3965	269	15	5
atsz-31a	Atlantic	-60.2529	10.7739	269	15	17.94
atsz-31b	Atlantic	-60.2453	10.3401	269	15	5
atsz-32a	Atlantic	-59.3510	10.8123	269	15	17.94
atsz-32b	Atlantic	-59.3734	10.3785	269	15	5
atsz-33a	Atlantic	-58.7592	10.8785	248.6	15	17.94
atsz-33b	Atlantic	-58.5984	10.4745	248.6	15	5
atsz-34a	Atlantic	-58.5699	11.0330	217.2	15	17.94
atsz-34b	Atlantic	-58.2179	10.7710	217.2	15	5
atsz-35a	Atlantic	-58.3549	11.5300	193.7	15	17.94
atsz-35b	Atlantic	-57.9248	11.4274	193.7	15	5
atsz-36a	Atlantic	-58.3432	12.1858	177.7	15	17.94
atsz-36b	Atlantic	-57.8997	12.2036	177.7	15	5
atsz-37a	Atlantic	-58.4490	12.9725	170.7	15	17.94
atsz-37b	Atlantic	-58.0095	13.0424	170.7	15	5
atsz-38a	Atlantic	-58.6079	13.8503	170.2	15	17.94
atsz-38b	Atlantic	-58.1674	13.9240	170.2	15	5
atsz-39a	Atlantic	-58.6667	14.3915	146.8	15	17.94
atsz-39b	Atlantic	-58.2913	14.6287	146.8	15	5
atsz-39y	Atlantic	-59.4168	13.9171	146.8	15	43.82
atsz-39z	Atlantic	-59.0415	14.1543	146.8	15	30.88
atsz-40a	Atlantic	-59.1899	15.2143	156.2	15	17.94
atsz-40b	Atlantic	-58.7781	15.3892	156.2	15	5
atsz-40y	Atlantic	-60.0131	14.8646	156.2	15	43.82
atsz-40z	Atlantic	-59.6012	15.0395	156.2	15	30.88
atsz-41a	Atlantic	-59.4723	15.7987	146.3	15	17.94
atsz-41b	Atlantic	-59.0966	16.0392	146.3	15	5

continued on next page

Table B1: (continued)

Segment	Description	Longitude (°E)	Latitude (°N)	Strike (°)	Dip (°)	Depth (km)
atsz-41y	Atlantic	-60.2229	15.3177	146.3	15	43.82
atsz-41z	Atlantic	-59.8473	15.5582	146.3	15	30.88
atsz-42a	Atlantic	-59.9029	16.4535	137	15	17.94
atsz-42b	Atlantic	-59.5716	16.7494	137	15	5
atsz-42y	Atlantic	-60.5645	15.8616	137	15	43.82
atsz-42z	Atlantic	-60.2334	16.1575	137	15	30.88
atsz-43a	Atlantic	-60.5996	17.0903	138.7	15	17.94
atsz-43b	Atlantic	-60.2580	17.3766	138.7	15	5
atsz-43y	Atlantic	-61.2818	16.5177	138.7	15	43.82
atsz-43z	Atlantic	-60.9404	16.8040	138.7	15	30.88
atsz-44a	Atlantic	-61.1559	17.8560	141.1	15	17.94
atsz-44b	Atlantic	-60.8008	18.1286	141.1	15	5
atsz-44y	Atlantic	-61.8651	17.3108	141.1	15	43.82
atsz-44z	Atlantic	-61.5102	17.5834	141.1	15	30.88
atsz-45a	Atlantic	-61.5491	18.0566	112.8	15	17.94
atsz-45b	Atlantic	-61.3716	18.4564	112.8	15	5
atsz-45y	Atlantic	-61.9037	17.2569	112.8	15	43.82
atsz-45z	Atlantic	-61.7260	17.6567	112.8	15	30.88
atsz-46a	Atlantic	-62.4217	18.4149	117.9	15	17.94
atsz-46b	Atlantic	-62.2075	18.7985	117.9	15	5
atsz-46y	Atlantic	-62.8493	17.6477	117.9	15	43.82
atsz-46z	Atlantic	-62.6352	18.0313	117.9	15	30.88
atsz-47a	Atlantic	-63.1649	18.7844	110.5	20	22.1
atsz-47b	Atlantic	-63.0087	19.1798	110.5	20	5
atsz-47y	Atlantic	-63.4770	17.9936	110.5	20	56.3
atsz-47z	Atlantic	-63.3205	18.3890	110.5	20	39.2
atsz-48a	Atlantic	-63.8800	18.8870	110.5	20	22.1
atsz-48b	Atlantic	-63.8382	19.3072	110.5	20	5
atsz-48y	Atlantic	-63.9643	18.0465	95.37	20	56.3
atsz-48z	Atlantic	-63.9216	18.4667	95.37	20	39.2
atsz-49a	Atlantic	-64.8153	18.9650	94.34	20	22.1
atsz-49b	Atlantic	-64.7814	19.3859	94.34	20	5
atsz-49y	Atlantic	-64.8840	18.1233	94.34	20	56.3
atsz-49z	Atlantic	-64.8492	18.5442	94.34	20	39.2
atsz-50a	Atlantic	-65.6921	18.9848	89.59	20	22.1
atsz-50b	Atlantic	-65.6953	19.4069	89.59	20	5
atsz-50y	Atlantic	-65.6874	18.1407	89.59	20	56.3
atsz-50z	Atlantic	-65.6887	18.5628	89.59	20	39.2
atsz-51a	Atlantic	-66.5742	18.9484	84.98	20	22.1
atsz-51b	Atlantic	-66.6133	19.3688	84.98	20	5
atsz-51y	Atlantic	-66.4977	18.1076	84.98	20	56.3
atsz-51z	Atlantic	-66.5353	18.5280	84.98	20	39.2
atsz-52a	Atlantic	-67.5412	18.8738	85.87	20	22.1
atsz-52b	Atlantic	-67.5734	19.2948	85.87	20	5

continued on next page

Table B1: (continued)

Segment	Description	Longitude (°E)	Latitude (°N)	Strike (°)	Dip (°)	Depth (km)
atsz-52y	Atlantic	-67.4781	18.0319	85.87	20	56.3
atsz-52z	Atlantic	-67.5090	18.4529	85.87	20	39.2
atsz-53a	Atlantic	-68.4547	18.7853	83.64	20	22.1
atsz-53b	Atlantic	-68.5042	19.2048	83.64	20	5
atsz-53y	Atlantic	-68.3575	17.9463	83.64	20	56.3
atsz-53z	Atlantic	-68.4055	18.3658	83.64	20	39.2
atsz-54a	Atlantic	-69.6740	18.8841	101.5	20	22.1
atsz-54b	Atlantic	-69.5846	19.2976	101.5	20	5
atsz-55a	Atlantic	-70.7045	19.1376	108.2	20	22.1
atsz-55b	Atlantic	-70.5647	19.5386	108.2	20	5
atsz-56a	Atlantic	-71.5368	19.3853	102.6	20	22.1
atsz-56b	Atlantic	-71.4386	19.7971	102.6	20	5
atsz-57a	Atlantic	-72.3535	19.4838	94.2	20	22.1
atsz-57b	Atlantic	-72.3206	19.9047	94.2	20	5
atsz-58a	Atlantic	-73.1580	19.4498	84.34	20	22.1
atsz-58b	Atlantic	-73.2022	19.8698	84.34	20	5
atsz-59a	Atlantic	-74.3567	20.9620	259.7	20	22.1
atsz-59b	Atlantic	-74.2764	20.5467	259.7	20	5
atsz-60a	Atlantic	-75.2386	20.8622	264.2	15	17.94
atsz-60b	Atlantic	-75.1917	20.4306	264.2	15	5
atsz-61a	Atlantic	-76.2383	20.7425	260.7	15	17.94
atsz-61b	Atlantic	-76.1635	20.3144	260.7	15	5
atsz-62a	Atlantic	-77.2021-	20.5910	259.9	15	17.94
atsz-62b	Atlantic	77.1214	20.1638	259.9	15	5
atsz-63a	Atlantic	-78.1540	20.4189	259	15	17.94
atsz-63b	Atlantic	-78.0661	19.9930	259	15	5
atsz-64a	Atlantic	-79.0959	20.2498	259.2	15	17.94
atsz-64b	Atlantic	-79.0098	19.8236	259.2	15	5
atsz-65a	Atlantic	-80.0393	20.0773	258.9	15	17.94
atsz-65b	Atlantic	-79.9502	19.6516	258.9	15	5
atsz-66a	Atlantic	-80.9675	19.8993	258.6	15	17.94
atsz-66b	Atlantic	-80.8766	19.4740	258.6	15	5
atsz-67a	Atlantic	-81.9065	19.7214	258.5	15	17.94
atsz-67b	Atlantic	-81.8149	19.2962	258.5	15	5
atsz-68a	Atlantic	-87.8003	15.2509	62.69	15	17.94
atsz-68b	Atlantic	-88.0070	15.6364	62.69	15	5
atsz-69a	Atlantic	-87.0824	15.5331	72.73	15	17.94
atsz-69b	Atlantic	-87.2163	15.9474	72.73	15	5
atsz-70a	Atlantic	-86.1622	15.8274	70.64	15	17.94
atsz-70b	Atlantic	-86.3120	16.2367	70.64	15	5
atsz-71a	Atlantic	-85.3117	16.1052	73.7	15	17.94
atsz-71b	Atlantic	-85.4387	16.5216	73.7	15	5
atsz-72a	Atlantic	-84.3470	16.3820	69.66	15	17.94
atsz-72b	Atlantic	-84.5045	16.7888	69.66	15	5

continued on next page

Table B1: (continued)

Segment	Description	Longitude (°E)	Latitude (°N)	Strike (°)	Dip (°)	Depth (km)
atsz-73a	Atlantic	-83.5657	16.6196	77.36	15	17.94
atsz-73b	Atlantic	-83.6650	17.0429	77.36	15	5
atsz-74a	Atlantic	-82.7104	16.7695	82.35	15	17.94
atsz-74b	Atlantic	-82.7709	17.1995	82.35	15	5
atsz-75a	Atlantic	-81.7297	16.9003	79.86	15	17.94
atsz-75b	Atlantic	-81.8097	17.3274	79.86	15	5
atsz-76a	Atlantic	-80.9196	16.9495	82.95	15	17.94
atsz-76b	Atlantic	-80.9754	17.3801	82.95	15	5
atsz-77a	Atlantic	-79.8086	17.2357	67.95	15	17.94
atsz-77b	Atlantic	-79.9795	17.6378	67.95	15	5
atsz-78a	Atlantic	-79.0245	17.5415	73.61	15	17.94
atsz-78b	Atlantic	-79.1532	17.9577	73.61	15	5
atsz-79a	Atlantic	-78.4122	17.5689	94.07	15	17.94
atsz-79b	Atlantic	-78.3798	18.0017	94.07	15	5
atsz-80a	Atlantic	-77.6403	17.4391	103.3	15	17.94
atsz-80b	Atlantic	-77.5352	17.8613	103.3	15	5
atsz-81a	Atlantic	-76.6376	17.2984	98.21	15	17.94
atsz-81b	Atlantic	-76.5726	17.7278	98.21	15	5
atsz-82a	Atlantic	-75.7299	19.0217	260.1	15	17.94
atsz-82b	Atlantic	-75.6516	18.5942	260.1	15	5
atsz-83a	Atlantic	-74.8351	19.2911	260.8	15	17.94
atsz-83b	Atlantic	-74.7621	18.8628	260.8	15	5
atsz-84a	Atlantic	-73.6639	19.2991	274.8	15	17.94
atsz-84b	Atlantic	-73.7026	18.8668	274.8	15	5
atsz-85a	Atlantic	-72.8198	19.2019	270.6	15	17.94
atsz-85b	Atlantic	-72.8246	18.7681	270.6	15	5
atsz-86a	Atlantic	-71.9143	19.1477	269.1	15	17.94
atsz-86b	Atlantic	-71.9068	18.7139	269.1	15	5
atsz-87a	Atlantic	-70.4738	18.8821	304.5	15	17.94
atsz-87b	Atlantic	-70.7329	18.5245	304.5	15	5
atsz-88a	Atlantic	-69.7710	18.3902	308.9	15	17.94
atsz-88b	Atlantic	-70.0547	18.0504	308.4	15	5
atsz-89a	Atlantic	-69.2635	18.2099	283.9	15	17.94
atsz-89b	Atlantic	-69.3728	17.7887	283.9	15	5
atsz-90a	Atlantic	-68.5059	18.1443	272.9	15	17.94
atsz-90b	Atlantic	-68.5284	17.7110	272.9	15	5
atsz-91a	Atlantic	-67.6428	18.1438	267.8	15	17.94
atsz-91b	Atlantic	-67.6256	17.7103	267.8	15	5
atsz-92a	Atlantic	-66.8261	18.2536	262	15	17.94
atsz-92b	Atlantic	-66.7627	17.8240	262	15	5

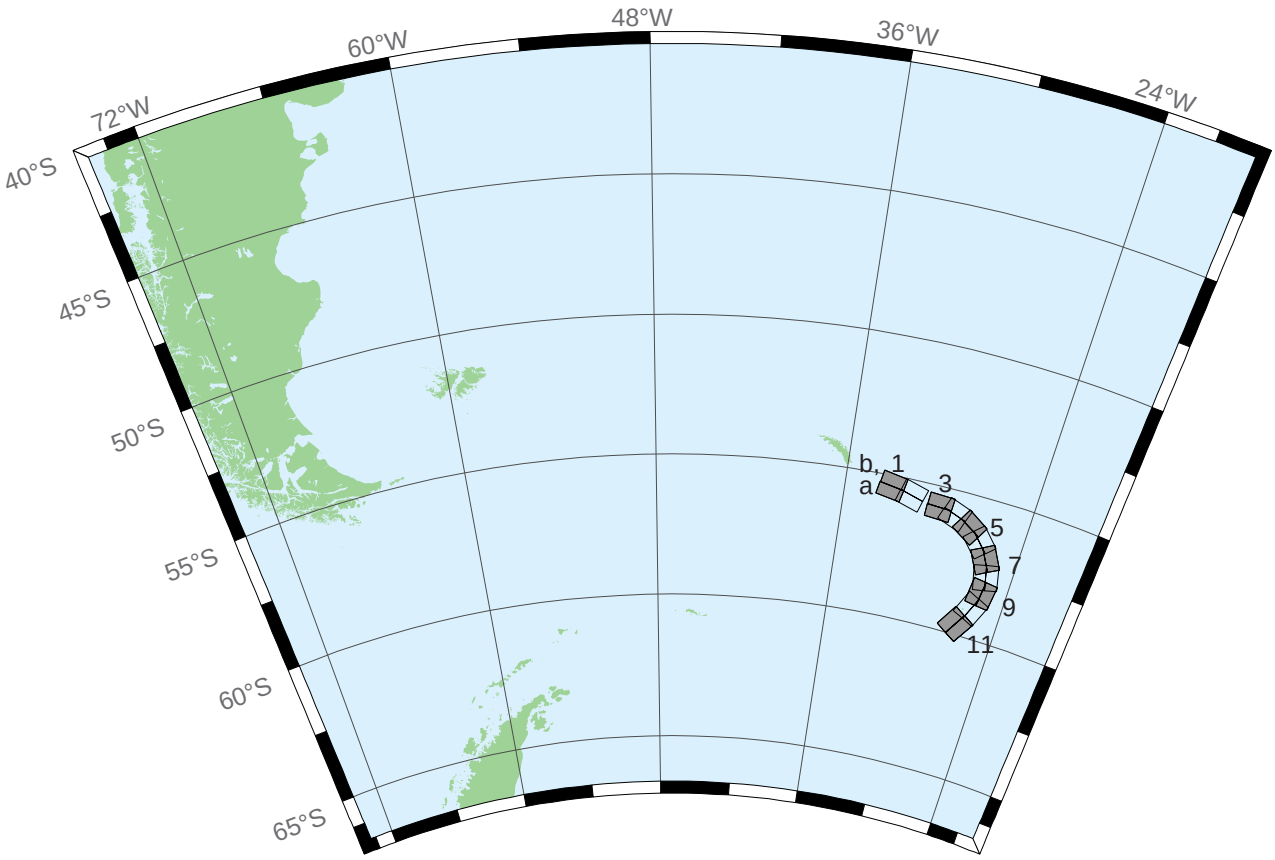

Figure B2: South Sandwich Islands Subduction Zone unit sources.

Table B2: Earthquake parameters for South Sandwich Islands Subduction Zone unit sources.

Segment	Description	Longitude (°E)	Latitude (°N)	Strike (°)	Dip (°)	Depth (km)
sssz-1a	South Sandwich Islands	-33.0670	-55.3780	280.2	15	17.94
sssz-1b	South Sandwich Islands	-32.9242	-54.9510	280.2	15	5
sssz-2a	South Sandwich Islands	-31.7197	-55.5621	286.3	15	17.94
sssz-2b	South Sandwich Islands	-31.4969	-55.1457	286.3	15	5
sssz-3a	South Sandwich Islands	-29.8355	-55.7456	273	15	17.94
sssz-3b	South Sandwich Islands	-29.7873	-55.3123	273	15	5
sssz-4a	South Sandwich Islands	-28.7648	-55.8715	290	15	17.94
sssz-4b	South Sandwich Islands	-28.4930	-55.4638	290	15	5
sssz-5a	South Sandwich Islands	-27.6356	-56.1844	301.5	15	17.94
sssz-5b	South Sandwich Islands	-27.2218	-55.8143	301.5	15	5
sssz-6a	South Sandwich Islands	-26.7655	-56.5959	317.5	15	17.94
sssz-6b	South Sandwich Islands	-26.1774	-56.3029	317.5	15	5
sssz-7a	South Sandwich Islands	-26.0921	-57.1441	332.1	15	17.94
sssz-7b	South Sandwich Islands	-25.3776	-56.9411	332.1	15	5
sssz-8a	South Sandwich Islands	-25.7129	-57.7563	347.9	15	17.94
sssz-8b	South Sandwich Islands	-24.9088	-57.6652	347.9	15	5
sssz-9a	South Sandwich Islands	-25.7003	-58.3505	7.182	15	17.94
sssz-9b	South Sandwich Islands	-24.8687	-58.4047	7.182	15	5
sssz-10a	South Sandwich Islands	-26.0673	-58.9577	24.25	15	17.94
sssz-10b	South Sandwich Islands	-25.2869	-59.1359	24.25	15	5
sssz-11a	South Sandwich Islands	-26.8279	-59.6329	32.7	15	17.94
sssz-11b	South Sandwich Islands	-26.0913	-59.8673	32.7	15	5

Appendix C.
Synthetic Testing: Nantucket, Massachusetts*

C1. Purpose

Forecast models are tested with synthetic tsunami events covering a range of tsunami source locations and magnitudes ranging from mega-tsunami events to micro-tsunami events. Testing is also done with selected historical tsunami events when available.

The purpose of forecast model testing is three-fold. The first objective is to assure that the results obtained with NOAA's tsunami forecast system, which has been released to the Tsunami Warning Centers for operational use, are consistent with those obtained by the researcher during the development of the forecast model. The second objective is to test the forecast model for consistency, accuracy, time efficiency, and quality of results over a range of possible tsunami locations and magnitudes. The third objective is to identify bugs and issues in need of resolution by the researcher who developed the forecast model or by the forecast software development team before the next version release to NOAA's two Tsunami Warning Centers.

Local hardware and software applications are used with tools familiar to the researcher(s) to run the Method of Splitting Tsunami (MOST) model during the forecast model development. The test results presented in this report lend confidence that the model performs as developed and produces the same results when initiated within the forecast application in an operational setting as those produced by the researcher during the forecast model development. The test results assure those who rely on the tsunami forecast model for Nantucket, Massachusetts, that consistent results are produced irrespective of system.

C2. Testing procedure

The general procedure for forecast model testing is to run a set of synthetic tsunami scenarios and a selected set of historical tsunami events through the forecast system application, and compare the results with those obtained by the researcher during the forecast model development (as presented in the Tsunami Forecast Model Report). Specific steps taken to test the model include:

1. Identification of testing scenarios, including the standard set of synthetic events, appropriate historical events, and customized synthetic scenarios that may have been used by the researcher(s) in the development of the forecast model.
2. Creation of new events to represent customized synthetic scenarios used by the researcher(s) in the development of the forecast model, if any.

---

* Authors: Mick Spillane, Lindsey Wright

3. Submission of test model runs with the forecast system, and export of the results from A, B, and C grids, along with time series.
4. Recording applicable metadata, including the specific version of the forecast system used for testing.
5. Examination of forecast system model results for instabilities in both time series and plot results.
6. Comparison of forecast model results obtained through the forecast system with those obtained during the forecast model development.
7. Summarization of results with specific mention of quality, consistency, and time efficiency.
8. Reporting of issues identified to modeler and forecast software development team.
9. Retesting the forecast models in the forecast system when reported issues have been addressed or explained.

Synthetic model runs were tested on a DELL PowerEdge R510 computer equipped with two Xeon E5670 processors at 2.93 GHz, each with 12 MBytes of cache and 32 GB memory. The processors are hex core and support hyperthreading, resulting in the computer performing as a 24 processor core machine. Additionally, the testing computer supports 10 Gigabit Ethernet for fast network connections. This computer configuration is similar or the same as the configurations of the computers installed at the Tsunami Warning Centers so the compute times should only vary slightly.

C3. Results

The Nantucket forecast model was tested with NOAA's tsunami forecast system SIFT. Test results from the forecast system and comparisons with the results obtained during the forecast model development are shown numerically in **Table C1** and graphically as described below. The results show that the forecast model is stable and robust, with consistent and high quality results across geographically distributed tsunami sources and mega-tsunami event magnitudes. The model run times for all three cases (wall-clock time) were under 24.4 min for 12 hr of simulation time, and under 8.2 min for 4 hr, thereby satisfying the "10 min run time per 4 hr of simulated time" criterion for operational efficiency.

A suite of three synthetic events was run on the Nantucket forecast model. The modeled scenarios were stable for all cases run with no inconsistencies or ringing. All scenarios tested produced wave heights less than 100 cm. The largest modeled height (see **Table C1**) was 76 cm from the Atlantic (ATSZ 48–57) source zone, and the smallest signal of 20 cm originated from the far-field South Sandwich (SSSZ 1–10) source zone. Comparisons between the development cases and the forecast system output were consistent in shape and amplitude for all cases run. The Nantucket reference point used for the forecast model development is the same as what is deployed in the forecast system, so the results can be considered valid for the three cases studied.

Table C1: Maximum and minimum amplitudes (cm) at the Nantucket, Massachusetts, warning point for synthetic and historical events tested using SIFT 3.2 and obtained during development. No historical cases were available.

				Maxima (cm)		Minima (cm)	
Scenarios	**Source Zone**	**Tsunami Source**	**α [m]**	**SIFT**	**Development**	**SIFT**	**Development**
Mega-tsunami Scenarios							
ATSZ 38–47	Atlantic	A38–47, B38–47	25	38.8	38.72	-25.4	-25.39
ATSZ 48–57	Atlantic	A48–57, B48–57	25	76.3	76.28	-19.4	-19.39
SSSZ 01–10	South Sandwich Islands	A01–10, B01–10	25	20.2	20.22	-17.7	-17.70

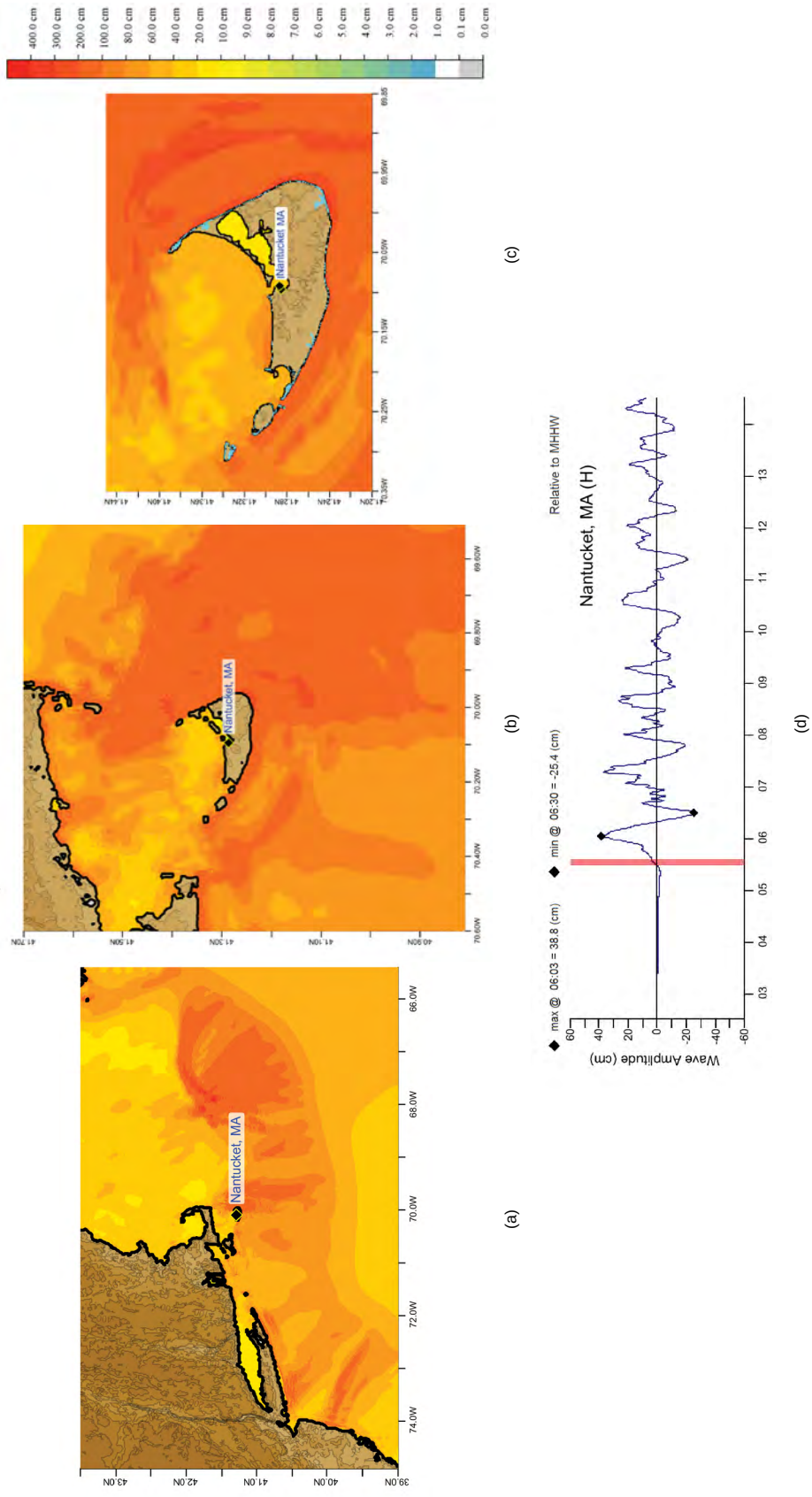

Figure C1: Response of the Nantucket forecast model to synthetic scenario ATSZ 38–47 (α=25). Maximum sea surface elevation for (a) A grid, (b) B grid, and (c) C grid. Sea surface elevation time series at the C-grid warning point (d). Panels (c) and (d) can be compared with the equivalent results, obtained during model development, displayed in **Figures 28** and **30**.

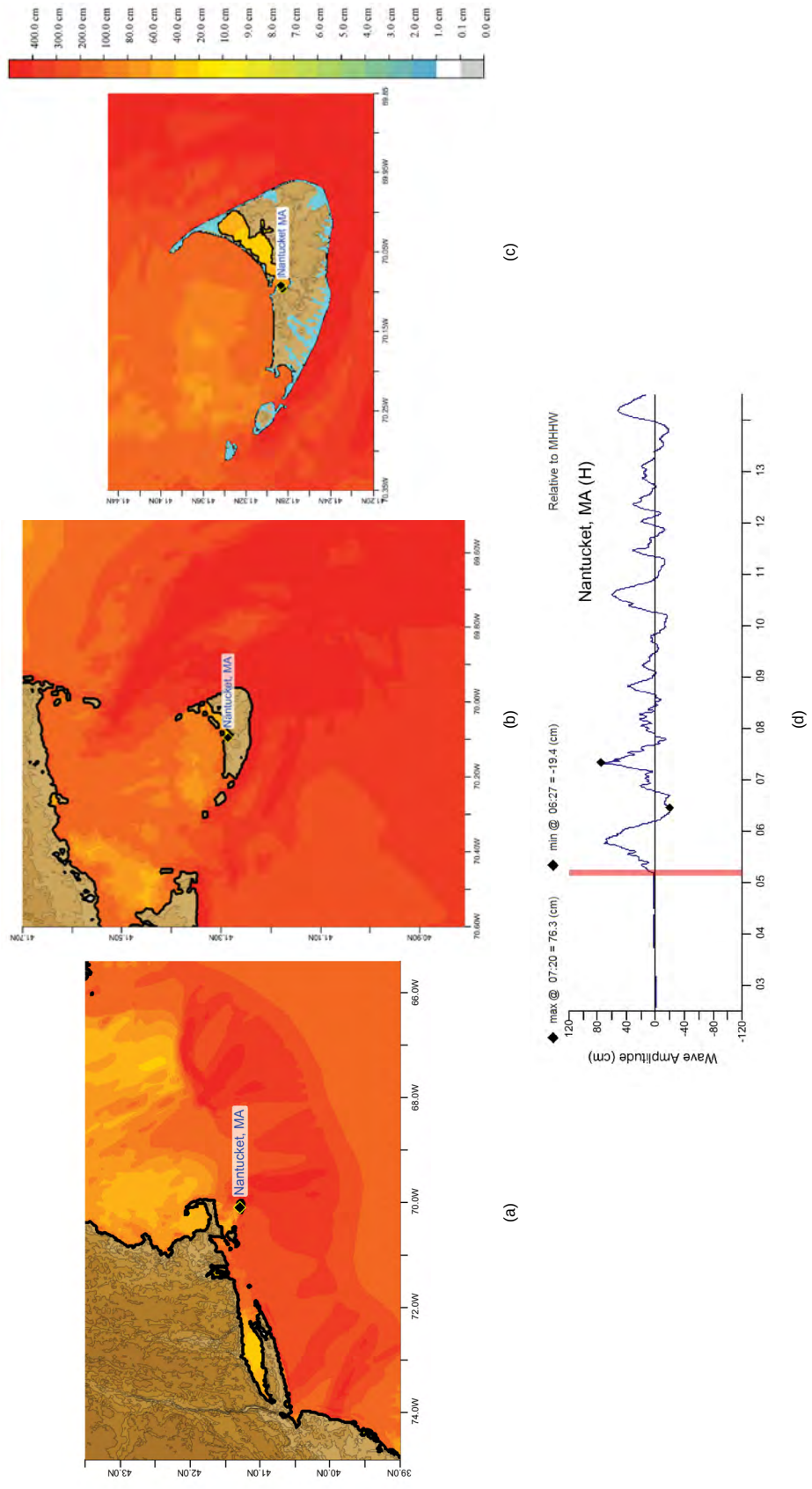

Figure C2: Response of the Nantucket forecast model to synthetic scenario ATSZ 48–57 (α=25). Maximum sea surface elevation for (a) A grid, (b) B grid, and (c) C grid. Sea surface elevation time series at the C-grid warning point (d). Panels (c) and (d) can be compared with the equivalent results, obtained during model development, displayed in **Figures 16** and **18**.

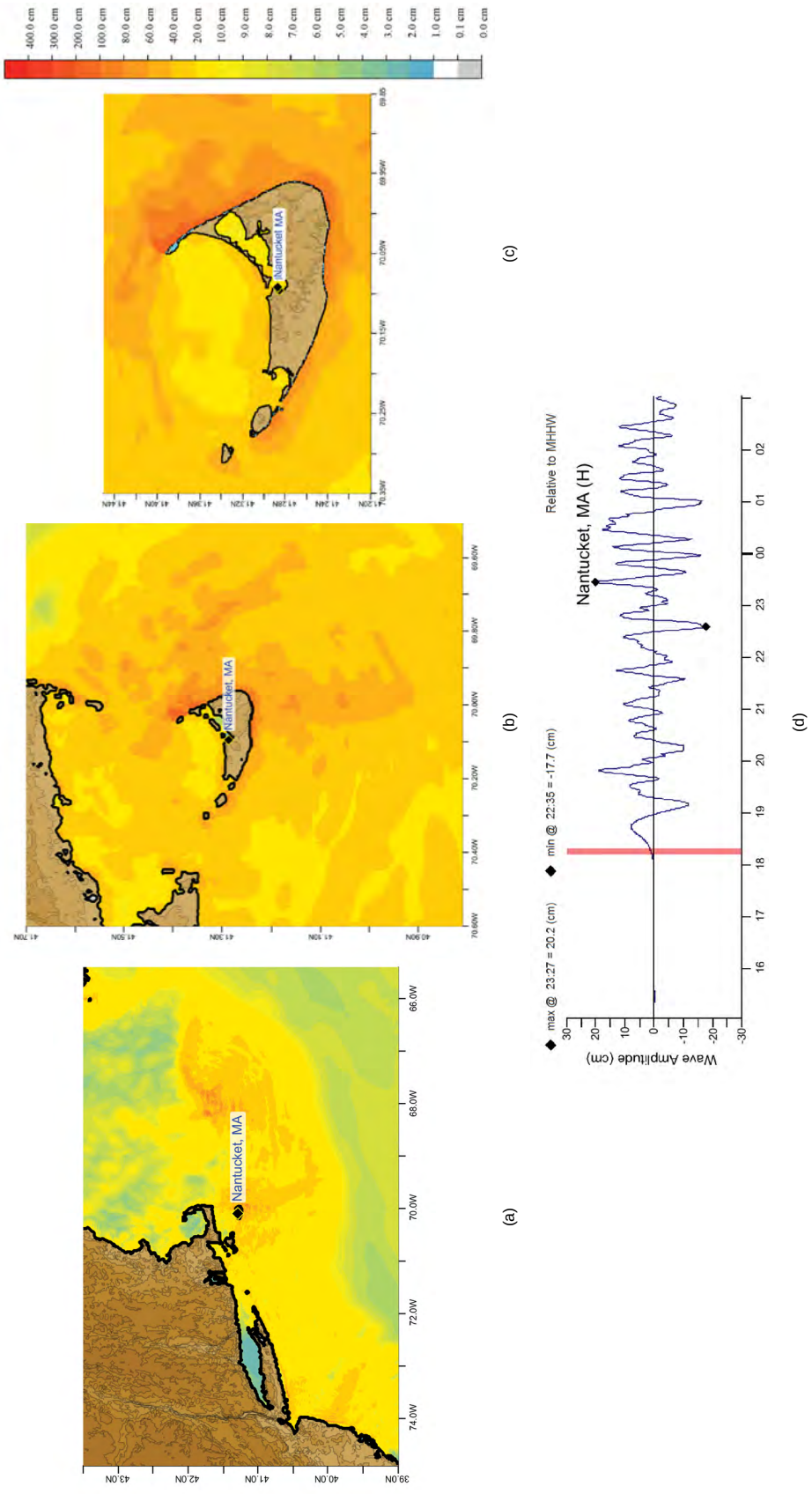

Figure C3: Response of the Nantucket forecast model to synthetic scenario SSSZ 1–10 (a=25). Maximum sea surface elevation for (a) A grid, (b) B grid, and (c) C grid. Sea surface elevation time series at the C-grid warning point (d). Panels (c) and (d) can be compared with the equivalent results, obtained during model development, displayed in **Figures 37** and **39**.

Glossary

Arrival time The time when the first tsunami wave is observed at a particular location, typically given in local and/or universal time, but also commonly noted in minutes or hours relative to the time of the earthquake.

Bathymetry The measurement of water depth of an undisturbed body of water.

Cascadia Subduction Zone Fault that extends from Cape Mendocino in Northern California northward to mid-Vancouver Island, Canada. The fault marks the convergence boundary where the Juan de Fuca tectonic plate is being subducted under the margin of the North America plate.

Current speed The scalar rate of water motion measured as distance/time.

Current velocity Movement of water expressed as a vector quantity. Velocity is the distance of movement per time coupled with direction of motion.

Deep-ocean Assessment and Reporting of Tsunamis (DART®) Tsunami detection and transmission system that measures the pressure of an overlying column of water and detects the passage of a tsunami.

Digital Elevation Model (DEM) A digital representation of bathymetry or topography based on regional survey data or satellite imagery. Data are arrays of regularly spaced elevations referenced to a map projection of the geographic coordinate system.

Epicenter The point on the surface of the earth that is directly above the focus of an earthquake.

Far-field Region outside of the source of a tsunami where no direct observations of the tsunami-generating event are evident, except for the tsunami waves themselves.

Focus The point beneath the surface of the earth where a rupture or energy release occurs due to a buildup of stress or the movement of Earth's tectonic plates relative to one another.

Inundation The horizontal inland extent of land that a tsunami penetrates, generally measured perpendicularly to a shoreline.

Marigram Tide gauge recording of wave level as a function of time at a particular location. The instrument used for recording is termed a marigraph.

Method of Splitting Tsunami (MOST) A suite of numerical simulation codes used to provide estimates of the three processes of tsunami evolution: tsunami generation, propagation, and inundation.

Moment magnitude (Mw) The magnitude of an earthquake on a logarithmic scale in terms of the energy released. Moment magnitude is based on the size and characteristics of a fault rupture as determined from long-period seismic waves.

Near–field Region of primary tsunami impact near the source of a tsunami. The near-field is defined as the region where non-tsunami effects of the tsunami-generating event have been observed, such as earth shaking from the earthquake, visible or measured ground deformation, or other direct (non-tsunami) evidences of the source of the tsunami wave.

Propagation database A basin-wide database of precomputed water elevations and flow velocities at uniformly spaced grid points throughout the world oceans. Values are computed from tsunamis generated by earthquakes with a fault rupture at any one of discrete 100 × 50 km unit sources along worldwide subduction zones.

Runup Vertical difference between the elevation of tsunami inundation and the sea level at the time of a tsunami. Runup is the elevation of the highest point of land inundated by a tsunami as measured relative to a stated datum, such as mean sea level.

Short-term Inundation Forecasting for Tsunamis (SIFT) A tsunami forecast system that integrates tsunami observations in deep ocean with numerical models to provide an estimate of tsunami wave arrival and amplitude at specific coastal locations while a tsunami propagates across an ocean basin.

Subduction zone A submarine region of the earth's crust at which two or more tectonic plates converge to cause one plate to sink under another, overriding plate. Subduction zones are regions of high seismic activity.

Synthetic event Hypothetical events based on computer simulations or theory of possible or even likely future scenarios.

Tele-tsunami or **distant tsunami** or **far-field tsunami** Most commonly, a tsunami originating from a source greater than 1000 km away from a particular location. In some contexts, a tele-tsunami is one that propagates through deep ocean before reaching a particular location without regard to distance separation.

Tidal wave Term frequently used incorrectly as a synonym for tsunami. A tsunami is unrelated to the predictable periodic rise and fall of sea level due to the gravitational attractions of the moon and sun; see **Tide**, below.

Tide The predictable rise and fall of a body of water (ocean, sea, bay, etc.) due to the gravitational attractions of the moon and sun.

Tide gauge An instrument for measuring the rise and fall of a column of water over time at a particular location.

Travel time The time it takes for a tsunami to travel from the generating source to a particular location.

Tsunameter An oceanographic instrument used to detect and measure tsunamis in the deep ocean. Tsunami measurements are typically transmitted acoustically to a surface buoy that in turn relays them in real time to ground stations via satellite.

Tsunami A Japanese term that literally translates to "harbor wave." Tsunamis are a series of long-period shallow water waves that are generated by the sudden displacement of water due to subsea disturbances such as earthquakes, submarine landslides, or volcanic eruptions. Less commonly, meteoric impact to the ocean or meteorological forcing can generate a tsunami.

Tsunami hazard assessment A systematic investigation of seismically active regions of the world oceans to determine their potential tsunami impact at a particular location. Numerical models are typically used to characterize tsunami generation, propagation, and inundation, and to quantify the risk posed to a particular community from tsunamis generated in each source region investigated.

Tsunami propagation The directional movement of a tsunami wave outward from the source of generation. The speed at which a tsunami propagates depends on the depth of the water column in which the wave is traveling. Tsunamis travel at a speed of 700 km/hr (450 mi/hr) over the average depth of 4000 m in the open deep Pacific Ocean.

Tsunami magnitude A number that characterizes the strength of a tsunami based on the tsunami wave amplitudes. Several different tsunami magnitude determination methods have been proposed.

Tsunami source Location of tsunami origin, most typically an underwater earthquake epicenter. Tsunamis are also generated by submarine landslides, underwater volcanic eruptions, or, less commonly, by meteoric impact of the ocean.

Wall-clock time The time that passes on a common clock or watch between the start and end of a model run, as distinguished from the time needed by a CPU or computer processor to complete the run, typically less than wall-clock time.

Wave amplitude The maximum vertical rise or drop of a column of water as measured from wave crest (peak) or trough to a defined mean water level state.

Wave crest or peak The highest part of a wave or maximum rise above a defined mean water level state, such as mean lower low water.

Wave height The vertical difference between the highest part of a specific wave (crest) and its corresponding lowest point (trough).

Wavelength The horizontal distance between two successive wave crests or troughs.

Wave period The length of time between the passage of two successive wave crests or troughs as measured at a fixed location.

Wave trough The lowest part of a wave or the maximum drop below a defined mean water level state, such as mean lower low water.

PMEL Tsunami Forecast Series Locations

Adak, AK
Apra Harbor, Guam
Arecibo, Puerto Rico
Arena Cove, CA
Atka, AK
Atlantic City, NJ
Bar Harbor, ME
Cape Hatteras, NC
Charlotte Amalie, U.S. Virgin Islands
Chignik, AK
Christiansted, U.S. Virgin Islands
Cordova, AK
Craig, AK
Crescent City, CA — **Vol. 2**
Daytona Beach, FL
Elfin Cove, AK
Eureka, CA
Fajardo, PR
Florence, OR
Garibaldi, OR
Haleiwa, HI
Hilo, HI — **Vol. 1**
Homer, AK
Honolulu, HI
Kahului, HI
Kailua-Kona, HI
Kawaihae, HI
Keauhou, HI
Key West, FL
Kihei, HI
King Cove, AK
Kodiak, AK — **Vol. 4**
Lahaina, HI
La Push, WA
Los Angeles, CA
Mayaguez, PR
Midway Atoll — **Vol. 7**
Montauk, NY
Monterey, CA
Morehead City, NC
Myrtle Beach, SC
Nantucket, MA — **Vol. 8**
Nawiliwili, HI
Neah Bay, WA
Newport, OR — **Vol. 5**
Nikolski, AK
Ocean City, MD
Pago Pago, American Samoa
Palm Beach, FL
Pearl Harbor, HI
Point Reyes, CA — **Vol. 6**
Ponce, PR
Port Alexander, AK
Port Angeles, WA
Port Orford, OR
Port San Luis, CA
Port Townsend, WA
Portland, ME
San Diego, CA
San Francisco, CA — **Vol. 3**
San Juan, Puerto Rico
Sand Point, AK
Santa Barbara, CA
Santa Monica, CA
Savannah, GA
Seaside, OR
Seward, AK
Shemya, AK
Sitka, AK
Toke Point, WA
Unalaska, AK
Virginia Beach, VA
Wake Island, U.S. Territory
Westport, WA
Yakutat, AK

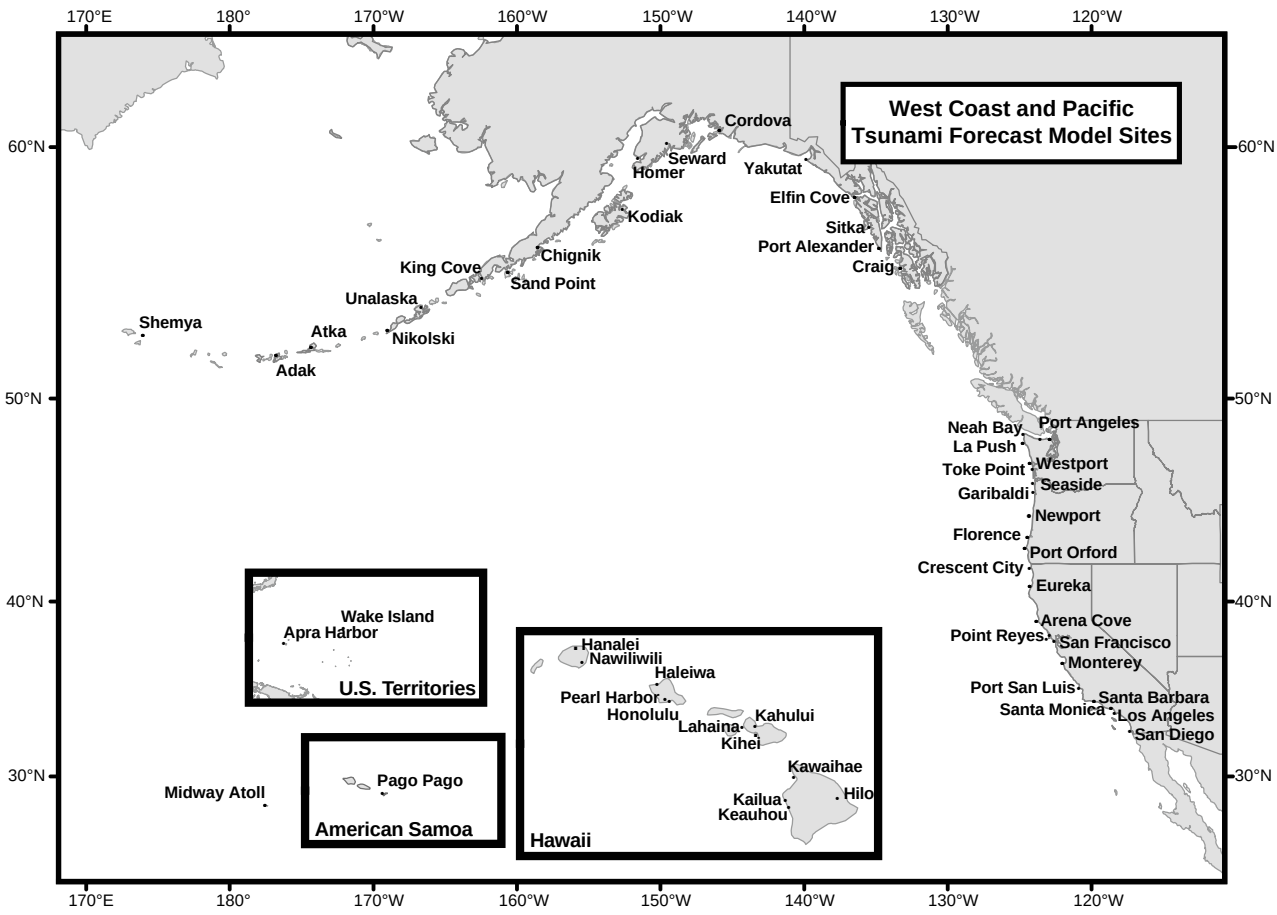
West Coast and Pacific
Tsunami Forecast Model Sites
170°E
180°
170°W
160°W
150°W
140°W
130°W
120°W
60°N
50°N
40°N
30°N
Cordova
Seward
Homer
Yakutat
Elfin Cove
Kodiak
Sitka
Port Alexander
Craig
Chignik
King Cove
Sand Point
Unalaska
Shemya
Atka
Nikolski
Adak
Neah Bay
Port Angeles
La Push
Toke Point
Westport
Seaside
Garibaldi
Newport
Florence
Port Orford
Crescent City
Eureka
Arena Cove
Point Reyes
San Francisco
Monterey
Port San Luis
Santa Barbara
Santa Monica
Los Angeles
San Diego
Wake Island
Apra Harbor
U.S. Territories
Hanalei
Nawiliwili
Haleiwa
Pearl Harbor
Honolulu
Lahaina
Kahului
Kihei
Kawaihae
Hilo
Kailua
Keauhou
Hawaii
Midway Atoll
Pago Pago
American Samoa

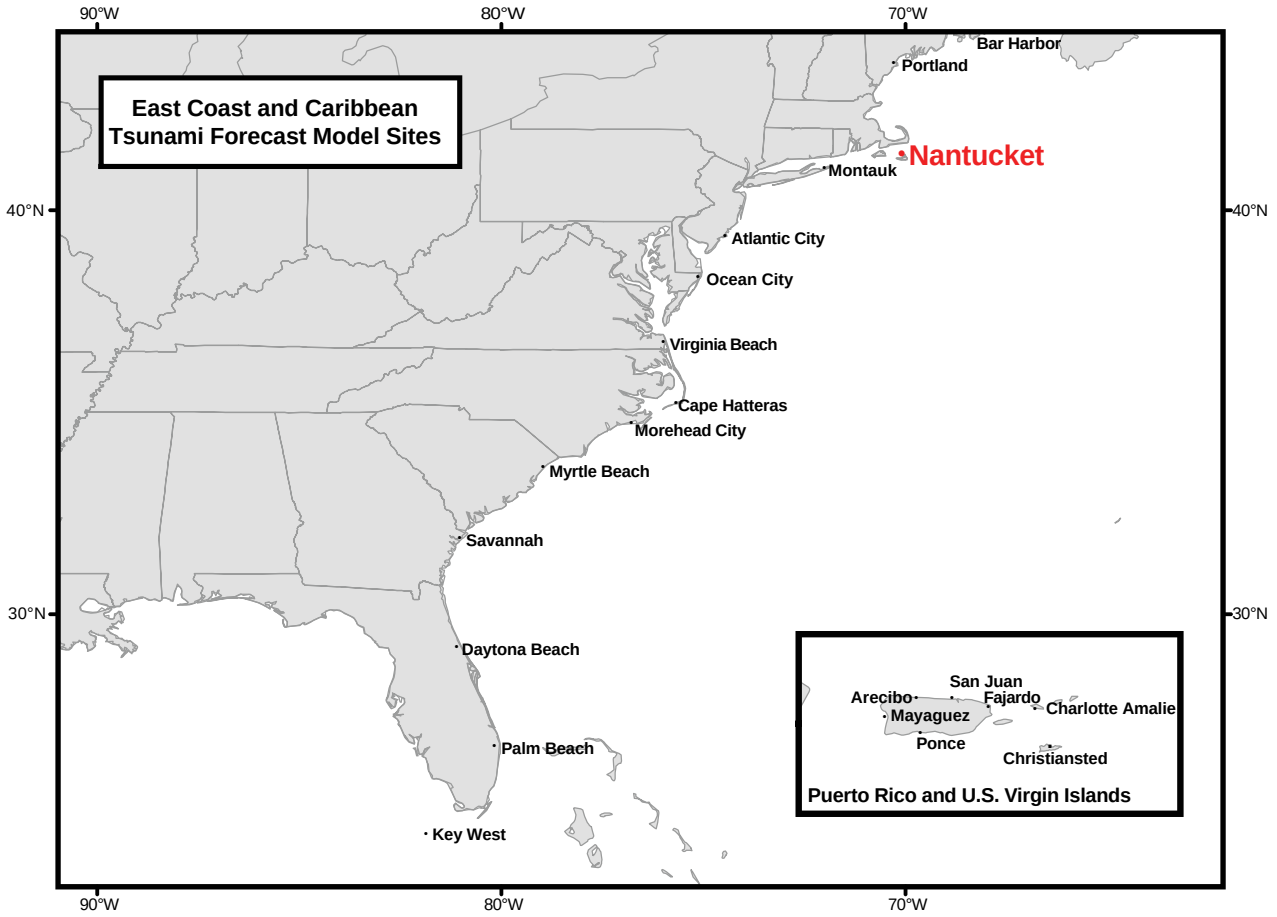
East Coast and Caribbean
Tsunami Forecast Model Sites
90°W
80°W
70°W
40°N
30°N
Bar Harbor
Portland
Nantucket
Montauk
Atlantic City
Ocean City
Virginia Beach
Cape Hatteras
Morehead City
Myrtle Beach
Savannah
Daytona Beach
Palm Beach
Key West
San Juan
Arecibo
Fajardo
Charlotte Amalie
Mayaguez
Ponce
Christiansted
Puerto Rico and U.S. Virgin Islands